ROLE OF LIGHT-FEEDING PHASE RELATIONS ON GLUCOSE METABOLISM

By

SEUL A. BAE

A dissertation submitted to the:

School of Graduate Studies

Rutgers, The State University of New Jersey

In partial fulfillment of the requirements

For the degree of

Doctor of Philosophy

Graduate Program in Chemical and Biochemical Engineering

Written under the direction of

Ioannis P. Androulakis, Ph. D.

And approved by:

_____

_____

_____

_____

New Brunswick, New Jersey

May, 2018

ABSTRACT OF THE DISSERTATION

Role of light-feeding phase relations on glucose metabolism

By SEUL A. BAE

Dissertation Director:

Ioannis P. Androulakis

Along with light/dark cycle, food intake is a strong *zeitgeber*, a cue given by the environment on host to reset the internal body clock. In mammals, metabolic activities are under the regulation of daily feeding rhythms as well as the peripheral clock machinery. In turn, the feeding rhythms influence the circadian rhythms of key clock components via enzymatic reactions and transcriptional regulations. Understanding the mechanism of interplay between the circadian clocks and metabolic activities are important as disruption of one seems to affect the other. Several studies showed evidence that disruption of circadian rhythms can facilitate metabolic syndrome. For example, shift-work and sleep deprivation result in dampened rhythms and obesity. Other studies suggested that obesity, diabetes, and cardiovascular diseases are linked with disruption of daily rhythms in food intake. At a molecular level, clock mutant mice show a decrease in metabolic rate, while liver-specific Bmal1 knockout mice and pancreas-specific Clock or Bmal1 knockout mice exhibit a disruption in glucose homeostasis. On the other hand, time-restricted feeding studies in mice show that metabolic cues influence circadian rhythmicityAlthough proper clock gene functions are linked to a wide variety of energy

metabolism functions including lipogenesis and appetite control, glucose homeostasis is of a particular interest since clock gene deficiencies directly lead to diabetes mellitus. Furthermore, possible molecular mechanisms that lead to a breach in glucose homeostasis have been suggested from a number of animal studies. I used semi-mechanistic mathematical models to evaluate the effect of circadian disruption on hepatic gluconeogenesis. The models allow examination of the entrainment dynamics of peripheral clock genes by two convoluted environmental signals, feeding rhythm transmitted through SIRT1 and the light/dark cycle transmitted through the hypothalamic pituitary adrenal axis (HPA) and cortisol. The mechanism behind metabolic implications under circadian disruption is achieved via linking the dynamics of clock genes and cortisol to transcription of gluconeogenic genes and insulin secretion. The model predicts that a few hours of restricted feeding in the early active phase of the host is beneficial for robust oscillation of clock genes, appropriate level of gluconeogenesis, and maximum secretion of insulin. Additionally, an asymmetry between the entrainment strengths of light/dark cycle and feeding/fasting cycle contributes to the convolusion of environmental signals in downstream metabolic activities.

Acknowledgements

I thank my advisor Ioannis P. Androulakis for his guidance, inspiration, understanding, and patience. I could not have completed this work without him. I also thank Alison, Rohit, and Kamau for being the kindest and the most supportive colleagues and friends. To Daniel and Jio, I love you very much. I would like to dedicate this work to all of them.

Table of Contents

List of Tables

List of Illustrations

CHAPTER 1: Background and motivation

1.1 Feeding rhythms and peripheral clock genes

The circadian rhythms orchestrate the mental and physical changes that follow a 24-hour cycle, primarily responding to light/dark schedule. In mammals, the central pace maker resides in the superchiasmatic nuclei (SCN) and takes in light as the entraining signal while synchronizing the clock genes in the periphery, influencing various rhythms in cells and tissues throughout the body. Aside from the light/dark cycle, food intake is also a strong *zeitgeber*, a cue given by the environment on host to reset the internal body clock. In mammals, metabolic activities are under the regulation of daily feeding rhythms as well as the peripheral clock machinery. In turn, the feeding rhythms influence the circadian rhythms of key clock components via enzymatic reactions and transcriptional regulations.[1-3] Understanding the mechanism of interplay between the circadian clocks and metabolic activities are important because disruption of one affects the other. Several studies show evidence that disruption of circadian rhythms can facilitate metabolic syndrome. For example, shift-work and sleep deprivation result in dampened rhythms and obesity.[4] Other studies suggested that obesity, diabetes, and cardiovascular diseases are linked with disruption of daily rhythms in food intake due to lifestyle choices and shift work.[5-7] On the other hand, time-restricted feeding studies in mice show that metabolic cues influence circadian rhythmicity. For example, restricted feeding schedule restored oscillations of some peripheral clock components in clock-deficient mouse livers.[8]

The evidence for the bi-directional influence between circadian clock and metabolism has been found in relation to the well-established core circadian clock machinery. Although some tissue-specific rhythms are observed throughout the body, the main driver for the core circadian clock in most tissues including liver and kidney is the positive and negative feedback loops between two protein complexes, CLOCK/BMAL1 heterodimer and PER/CRY complex [9-12]. The PER/CRY complex inhibits the CLOCK/BMAL1-mediated transcription of PER and CRY proteins, while stimulating the expression of BMAL1. Among the many ways that light/dark cycle and food availability impact each other, nutrient sensors such as AMP-activated protein kinase (AMPK), sirtuin 1 (SIRT1), and poly ADP-ribose polymerase 1 (PARP1) exhibit circadian behavior and interact with the key molecules of the core circadian clocks, while also playing key roles in metabolic activities.[13,14]

Recent literature suggest that SIRT1 is a key candidate for bridging the circadian clocks and metabolism. SIRT1 is a class III histone deacetylase (HDAC), a homolog of Sir2 (silence information regulator 2) in yeast.[2] Its activity takes place in the nucleus, modulating metabolism of lipids, proteins, and carbohydrates, while also enhancing mitochondrial activity,[15] in addition to modulating a variety of biological activities such as oncogenesis and aging.[16] SIRT1 acts as a nutrient sensor as its enzymatic activity requires binding of nicotinamide adenine dinucleotide (NAD^+) into its catalytic site along with the substrate. Modeling the activity of SIRT1 would require an accurate portrayal of the NAD^+ level in the cell, since it directly activates SIRT1. In addition to synthesizing NAD^+ from amino acids, cells can also recover NAD^+ from the NAD^+ salvage pathway,[17]

where nicotinamide (NAM) is released from NAD^+, NAM is converted to nicotinamide mononucleotide (NMN), and NMN is converted back to NAD^+, completing the cycle.

SIRT1 activity has complex relationships with the NAD^+ salvage pathway and the peripheral clocks. First, SIRT1 activity requires binding of NAD^+, thus NAD^+ has an activating effect on SIRT1. Second, SIRT1 activity is inhibited by NAM, the precursor of the rate-limiting step. Third, expression of nicotinamide mononucleotide adenylyltransferase (NAMPT), the rate-limiting enzyme of the NAD^+ salvage cycle, is under the control of SIRT1, which is a co-transcription factor for the Nampt gene along with peripheral clock genes (PCGs). In summary, SIRT1 functions as a nutrient sensor, being under the influence of the energy state of the cells, represented by NAD^+. It is also under the effect of the circadian rhythmicity presented by NAD^+, NAM, and NAMPT, which are under the control of PCGs.

The above observations motivate construction of a mathematical model that describes the interactions among SIRT1, NAD^+ salvage cycle, and peripheral clock genes in human hepatocyte, to study the effects of light and feeding schedules on circadian dynamics in the periphery. The model builds upon earlier works[18] of a semi-mechanical model for light entrainment on the peripheral clock genes through the HPA axis. The oscillations in the HPA axis are generated due to the negative feedback between glucocorticoid and corticotropin-releasing hormone (CRH)/adrenocorticotropic hormone (ACTH) using a modified Goodwin oscillator, entrained by light. The oscillating glucocorticoid is secreted into the periphery, scheduling the peripheral clock genes

(Per/Cry, Bmal1, and Clock). The two-way relationship between SIRT1 and PCGs will be incorporated to reflect the changes in the dynamics of PCGs due to food intake.

1.2 Circadian control of gluconeogenesis and insulin

Gluconeogenesis is the metabolic process that synthesizes glucose from non-carbohydrate sources such as pyruvate, lactate, glycerol, alanine, and glutamine. It is a ubiquitous process that has been preserved through evolution from microorganisms to mammals.[19] In mammals, gluconeogenesis mostly occurs in the liver during the fasting phase to keep the blood glucose level at a biologically safe level.[20] Glucose homeostasis is linked to the circadian genes through core clock gene knock-out experiments. In mice with liver-specific Bmal1 knock-out, altered rhythms for gluconeogenic genes were observed.[21] As a result, glucose levels during the late fasting phase were decreased for the knock-out animals compared to the control animals. In contrast, increased expression level of CRY1 and CRY2 proteins in the liver had a decreasing effect on the glucose level.[22] Per, Rev-erbα, and Clock gene knock-outs also affect the glucose metabolism.[23] Per knock-out results in decreased glucose levels while Rev-erbα knock-out leads to increased glucose levels. Clock knock-out animals exhibit conflicting results, showing increased glucose levels in some studies, while the opposite trend was seen in other studies, possibly because the Clock gene effect on carbohydrate metabolism is subject to genetic make-up of the animals and experimental/environmental factors.

Cortisol, the hormone that entrains the PCGs to the light/dark cycle, also plays an important role in maintaining glucose homeostasis in mammals. It is well established that

serum cortisol level increases gluconeogenesis in humans.[24] Under 12h of fasting conditions, gluconeogenesis is accounted for about 35% of the glucose production. When a high dose of cortisol is administered and the serum cortisol level is increased, gluconeogenesis is accounted for 65% of glucose production. In conscious, overnight-fasted dogs, acute physiological increases in plasma cortisol levels resulted in increased gluconeogenic conversion of alanine to glucose, by increasing both net hepatic alanine uptake (NHAU) and hepatic fractional extraction of alanine.[25] Cortisol stimulation of hepatic gluconeogenesis is probably due to activation of participating liver enzymes such as pyruvate carboxylase.[26] By contrast, *in vitro* experiments using mice fibroblasts showed that Cry1 and Cry2 inhibit the activating effect of glucocorticoid receptor by binding to the glucocorticoid response element (GRE) on the promoter of gluconeogenic genes.[27]

SIRT1, the enzyme that entrains the PCGs to the feeding state, has a direct influence on hepatic metabolism involved in glucose homeostasis. During long-term fasting (>6 hours), SIRT1 activity results in increased transcription of gluconeogenic genes, such as Pck1 and G6pc. During this phase, SIRT1-mediated deacetylation activates PPARγ-coactivator α (PGC-1α) and Forkhead box O1 (FOXO1).[28] In a feeding state where blood glucose level is increased, FOXO1 is phosphorylated via insulin mediated mechanism and is expelled to the cytoplasm, where it is ubiquitinated and degraded.[29] The translocation of FOXO1 from nucleus to cytoplasm involves multiple phosphorylation steps starting with insulin, released from the pancreas. Insulin first phosphorylates Phosphatidylinositol-4,5-bisphosphate 3-kinase (PI3K), then PI3K

phosphorylates protein kinase B (Akt). Finally, Akt phosphorylates FOXO1 and FOXO 1 is moved out of the nucleus.[29] Experimental evidence indicates that SIRT1-mediated deacetylation of FOXO1, in a fasting state, causes translocation of FOXO1 back to the nucleus, where it binds to the promoter for glucose-6-phosphatase (G6Pase), activating transcription of G6pc and thus increasing hepatic gluconeogenesis.[30] PGC-1α induces transcription of Pck1 and G6pc, along with its co-activators glucocorticoid receptor and hepatic nuclear factor-4α (HNF-4α).[31] In summary, SIRT1 deacetylates and activates PGC-1α and FOXO1, leading to gluconeogenesis; both are required for robust activation of gluconeogenic gene expression in hepatic cells.

The above observations motivate a need for a mechanistic model that incorporates the effect of SIRT1, cortisol, and insulin on hepatic gluconeogenesis, to establish the link between proper clock gene function and glucose metabolism. This model would also integrate the light-feeding phase relations to gluconeogenesis, possibly revealing how circadian disruption leads to metabolic syndrome.

1.3 Outline of the dissertation

The investigation on the effect of circadian disruption on metabolism involves a step-wise development and analysis of semi-mechanistic models. In Chapter 2 discusses the baseline model that incorporates the feeding/fasting cycle as an entraining factor for the peripheral clock genes. In Chapter 3, the model was further developed to link hepatic gluconeogenesis to phase relations between the light/dark cycle and feeding rhythms. A framework for sensitivity analysis was developed and implemented to analyze this model

in detail. In Chapter 4, a model describing the circadian secretion of insulin from the pancreatic β-cells were developed based on insulin granule dynamics. In Chapter 5 summarizes and addresses future directions and the major findings from the project.

CHAPTER 2: The synergistic role of light-feeding phase relations on entraining robust circadian rhythms in the periphery

2.1 Background

Time-restricted feeding studies in mammals show that circadian rhythmicity is dependent on metabolic cues along with the light/dark cycle. As an example, restricted feeding restored rhythms of some peripheral clock components in clock-deficient mouse livers.[8] Recent studies suggest that SIRT1 may play an important role in feeding entrainment of peripheral clocks through deacetylating core clock components. One such activity of SIRT1 is to facilitate the degradation of PER/CRY proteins in the nucleus. The CLOCK/BMAL1 complex also interacts with SIRT1 by binding to it and activating the transcription of NAMPT (the rate-limiting enzyme for the NAD^+ salvage cycle). NAD^+, in turn, acts as a direct activator of SIRT1. The above observations motivates construction of a mathematical model that describes the interactions among SIRT1, NAD+ salvage cycle, and peripheral clock genes in human hepatocyte, to study the effects of light and feeding cycles on circadian dynamics in the periphery. It is anticipated that phase relationship between the light and feeding cues may play an important role in the entrainment dynamics of the PCGs.

2.2 Methods

We developed a mathematical model to study the dynamics of circadian and metabolic components under the entrainment of two environmental cues, light/dark cycle and feeding rhythm. The model was built upon our previous work[18,32] by introducing

significant modifications to capture the changes to cellular energy state and metabolic activity due to the feeding state. The model is essentially composed of two compartments: 1) a central compartment that encompasses the feeding and light/dark cycle, entraining the cellular energy state and cortisol dynamics, and 2) a peripheral compartment representing a human hepatocyte that captures the convoluted downstream effects of released cortisol and cellular energy state on peripheral clock genes (PCGs) and metabolic components. The overall schematic of the model is shown in Figure 1.

2.2.1 Central Compartment

In the central compartment, the light/dark cycle, food availability during the day, and their signal transductions to the periphery are modeled. The environmental cues are represented as step functions in Equation (1) and Equations (4). In the baseline case when feeding pattern is synchronized to the light/dark cycle, a constant food supply is available between the hours of 6 am and 6 pm, and a constant supply of light source is present also between the hours of 6 am and 6 pm. Since the model aims to describe the dynamics of PCGs in human hepatocyte, the timespan where constant light signal is present is considered the active period when food intake normally occurs. Equation (1) was later modified for testing various feeding duration and delay relative to the light schedule. The feeding signal goes through two transit compartments each with a delay of 3 hours (τ_f), in Equations (2)-(3). Afterwards, feeding eventually entrains the dynamics of cellular energy state, NAD^+, by reducing it to NADH. The transit compartments for feeding signal were added to the model based on the experimental observations that NAD^+ level peaks 5-6 hours after the beginning of the active period in rat liver,[33]

suggesting a delay in feeding signal modifying the redox reactions between NAD^+ and NADH.

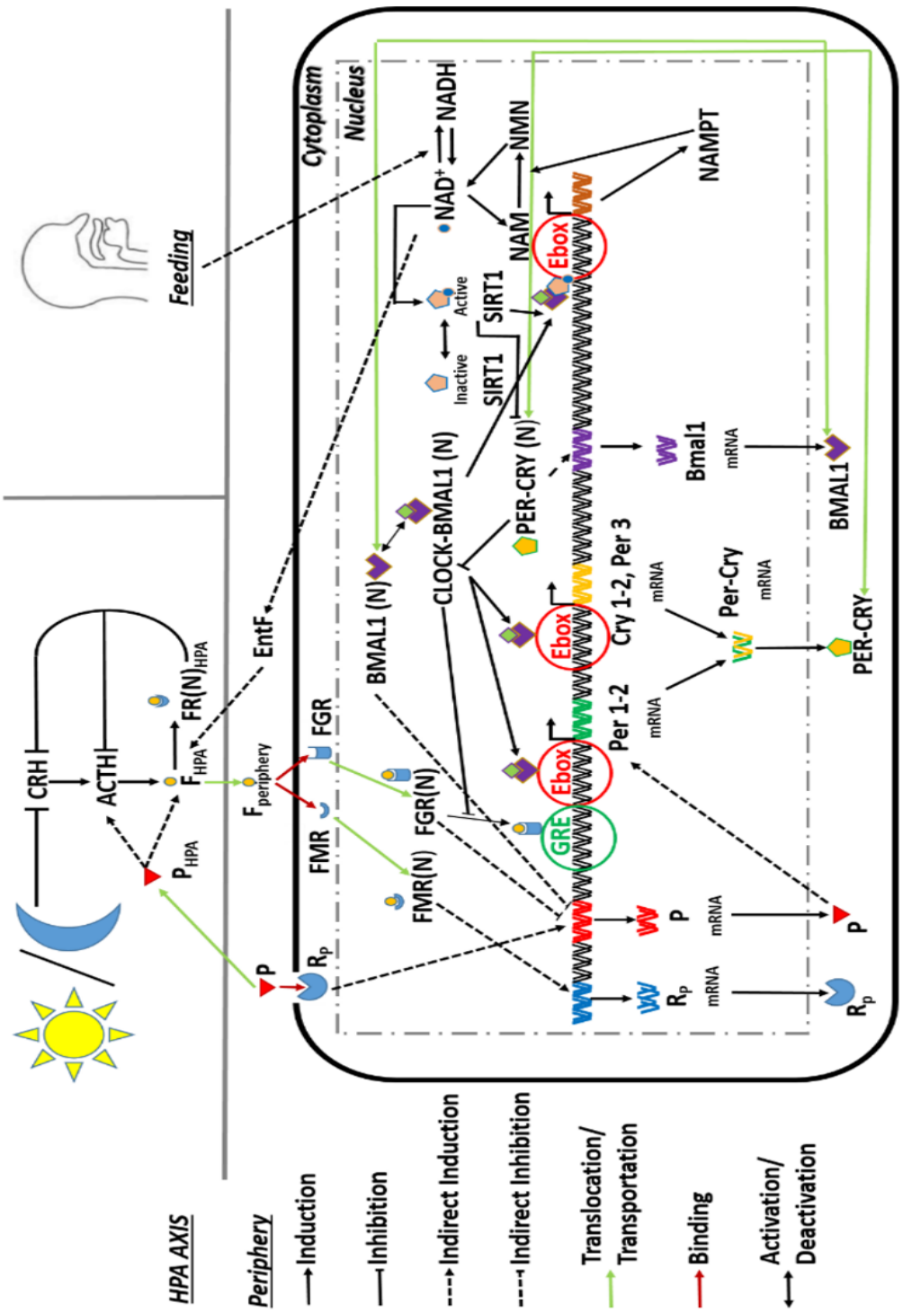
HPA AXIS
Periphery
Induction
Inhibition
Indirect Induction
Indirect Inhibition
Translocation/ Transportation
Binding
Activation/ Deactivation
CRH
ACTH
P_{HPA}
F_{HPA}
$FR(N)_{HPA}$
$F_{periphery}$
EntF
Feeding
Cytoplasm
Nucleus
FGR
FMR
FGR(N)
FMR(N)
R_P
P
mRNA
BMAL1 (N)
CLOCK-BMAL1 (N)
PER-CRY (N)
Active
Inactive
SIRT1
NAD^+
NADH
NAM
NMN
NAMPT
Ebox
GRE
Per 1-2
Cry 1-2, Per 3
Per-Cry
Bmal1
BMAL1
PER-CRY

Figure 1: Schematic representation of the light and feeding entrained model. The HPA is entrained to the light/dark cycle, and NAD^+ availability is entrained to food availability. Cortisol and SIRT1 in the periphery entrains the peripheral clock genes (PCGs).

The light signal is transmitted to the periphery through cortisol dynamics, driven by the self-sustained oscillations of CRH and ACTH in the HPA axis. The entrainment of these components by the light/dark cycle are described by Equations (4)-(7). These equations represent a Goodwin oscillator, modified to include Michaelis-Menten kinetics in the terms that represent synthesis and degradation of each component to avoid the use of unrealistically high Hill coefficients.[34] The production of CRH in the hypothalamus in Equation (5) leads to the secretion of ACTH in the anterior lobe of the pituitary gland in Equation (6). Equation (7) describes ACTH acting on the adrenal cortex, which produces the glucocorticoid hormones (mainly cortisol in humans). Then, cortisol negatively regulates CRH and ACTH via receptor mediated activities, creating a negative feedback loop and maintaining sustained oscillations in the absence of environmental cues. Equations (8)-(11) describe the signal transduction pathway that forms the cortisol-receptor complex. These equations were derived from a corticosteroid pharmacodynamic model.[35] Receptor mRNA dynamics is described by a zero order production and first order degradation terms in Equation (8). The indirect response model accounts for the experimentally observed downregulation of receptor mRNA upon methylprednisolone (MPL) treatment. The receptor protein dynamics is modeled in Equation (9), mediated by the receptor mRNA, degradation, binding rate to the ligand cortisol, and transfer in and out of the nucleus. Equations (10) and (11) describe the receptor binding to cortisol, and the resulting cortisol-receptor complex translocating to the nucleus to inhibit CRH and ACTH secretion. Finally, Equation (12) describes the

translocation of pro-inflammatory cytokines to the central compartment, which has an HPA-activating effect represented as stimulation of ACTH and cortisol using indirect response.[36]

The external light/dark cycle is transmitted to the hypothalamus as a photic signal via communication with retinal ganglion cells (RGCs) in the eye.[37] The hypothalamic suprachiasmatic nucleus (SCN) integrates the photic input and regulate the physiological circadian rhythms of the cortisol and the periphery.[38,39] The SCN mediates secretion of light-induced arginine vasopressin (AVP).[40] Given that decreased secretion of AVP leads to increased cortisol levels[41] and stimulating both CRH and ACTH release,[42] we ultimately regulate the production of cortisol by light-induced degradation of CRH (Equation (5)). We introduced a significant modification to the HPA axis to reflect the signals received by the SCN from feeding. Ventromedial arcuate nucleus (vmARC) is often associated with satiety because metabolically active hormones such as ghrelin, leptin, glucocorticoid, insulin, and their receptors are expressed at high levels in it.[43-46] These hormones, along with glucose, modulate the electrical activity of vmARC.[47-49] Studies confirmed that vmARC forms a complex with the subepidermal layer of the median eminence (seME), and have reciprocal connections with the SCN.[50] Therefore, we hypothesized that cellular energy state change caused by feeding in the periphery is transmitted to the SCN via electric signaling through the vmARC. Furthermore, studies showed that corticosterone rhythms change to show a food-anticipatory peak upon a change of feeding schedule.[51] From the above observations, we created a transit compartment, EntF, that represents the signaling activity from the periphery to the SCN

via vmARC, and added a response to this signal to cortisol production in the HPA axis using Michaelis-Menten kinetics. Parameter k_n in Equation (7) represents the coupling strength of the feeding signal to the SCN. The coupling strength was estimated to capture the qualitative behaviour of cortisol under conditions where feeding is synchronized to the active (light) period and feeding is anti-synchronized to the active period. When food is available during the active period, there is ample evidence that cortisol level peaks in the morning time.[52] However, when food availability is not synchronized to the light period, the cortisol level peaks slightly before food availability in the anticipation of incoming nutrients,[51] and the oscillation amplitude is expected to decrease.[53] The finalized value of the estimated parameter as well as all other parameters and their descriptions are shown in Table A1 in the appendix.

$$\text{feed} = \begin{cases} 1, & 6AM \le t < 6PM \\ 0, & 6PM \le t < 6AM \end{cases} \quad (1)$$

$$\frac{\text{dfeed2}}{\text{dt}} = \frac{1}{\tau_f}(feed - feed2) \quad (2)$$

$$\frac{\text{dfeed3}}{\text{dt}} = \frac{1}{\tau_f}(feed2 - feed3) \quad (3)$$

$$\text{light} = \begin{cases} 1, & 6AM \le t < 6PM \\ 0, & 6PM \le t < 6AM \end{cases} \quad (4)$$

$$\frac{dCRH}{dt} = \frac{k_{p1}}{K_{p1} + FR(N)_{HPA}} - V_{d1} \cdot \frac{CRH \cdot \left(1 + \frac{light}{1 + light}\right)}{K_{d1} + CRH} \quad (5)$$

$$\frac{dACTH}{dt} = \frac{k_{p2} \cdot CRH}{K_{p2} + FR(N)_{HPA}}(1 + k_{fp} \cdot P_{HPA}) - V_{d2} \cdot \frac{ACTH}{K_{d2} + ACTH} \quad (6)$$

$$\frac{dF_{HPA}}{dt} = k_{p3} \cdot ACTH \cdot \left(1 + k_{fp} \cdot P_{HPA}\right) \cdot k_n \cdot (1 + \frac{EntF}{1 + EntF}) - V_{d3} \cdot \frac{F_{HPA}}{K_{d3} + F_{HPA}} \quad (7)$$

$$\frac{dmRNA_{R,HPA}}{dt} = k_{syn\_Rm} \cdot \left(1 - \frac{FR(N)_{HPA}}{IC_{50_{Rm}} + FR(N)_{HPA}}\right) - k_{dgr_{Rm}} \cdot mRNA_{R\_HPA} \quad (8)$$

$$\frac{dR_{HPA}}{dt} = k_{syn\_R} \cdot mRNA_{R_{HPA}} + r_f \cdot k_{re} \cdot FR(N)_{HPA} - k_{on} \cdot (F_{HPA} - 1) \cdot R_{HPA} - k_{dgr_R} \cdot R_{HPA} \quad (9)$$

$$\frac{dFR_{HPA}}{dt} = k_{on}.F_{HPA}.R_{HPA} - k_t \cdot FR_{HPA} \quad (10)$$

$$\frac{dFR(N)_{HPA}}{dt} = k_t \cdot FR_{HPA} - k_{re} \cdot FR(N)_{HPA} \quad (11)$$

$$\frac{dP_{HPA}}{dt} = \frac{1}{\tau}(P - P_{HPA}) \quad (12)$$

2.2.2 Peripheral Compartment

The peripheral compartment represents a human hepatocyte and captures the downstream effects of released cortisol, entrained by the light/dark cycle, and cellular energy state, entrained by the feeding schedule, on peripheral clock genes (PCGs) and metabolic components.

The cortisol dynamics from the central compartment dominates the dynamics of cortisol in the peripheral compartment. The diffusion of cortisol to the cytoplasm in the periphery is modeled as a transit compartment in Equation (13). Once in the cytoplasm, cortisol can bind the mineralocorticoid (MR) and the glucocorticoid (GR) receptors and activate them. The dynamics of the cortisol-receptor interactions have been previously modeled by our group,[32] and parameters used were estimated based on human cortisol and cytokine experimental data.[54] In Equations (14) and (17), we assume that cortisol activates either the MR or GR by phosphorylation. The phosphorylation and dephosphorylation of the receptors are described with Michaelis-Menten kinetics. In

these equations, MRT and GRT represent the total receptor concentrations, where MR and GR represent the activated form of the receptors that are already phosphorylated. Subsequent terms represent the binding of the receptor with cortisol and the recycled receptors. The dynamics of the receptor-ligand complex are described by Equations (15) and (18), controlled by the binding rate and importation rate into the nucleus. Once the cortisol-receptor complex is translocated into the nucleus, the dynamics follow Equations (16) and (19), controlled by the importation rate and recycle rate back to the cytoplasm.

Once the cortisol-MR complex and cortisol-GR complex translocate to the nucleus, they exert influence on the dynamics of pro-inflammatory cytokines and the PCGs. Equations describing the circadian rhythmicity of pro-inflammatory cytokine and its receptor were adapted from previous works by our group.[32,36] Although the role of pro-inflammatory cytokines was modeled for an immune subsystem previously, the influence of cytokines on cortisol dynamics was still implemented for modeling the periphery representing a hepatocyte, as shown in Equation (7). The cytokines were adapted based on the justification that liver serves as an immunological organ.[55] In particular, human hepatocytes express pro-inflammatory cytokines such as interleukin-8 (IL-8), tumor necrosis factor- α (TNF-α), and growth related (GRO)- α, GRO-β, and GRO-γ[56] upon bacterial infection, showing that hepatocytes both initiate and amplify inflammatory responses. Furthermore, lipopolysaccharide (LPS) induced endotoxic shock has been shown to exaggerate the abolition or alteration of circadian rhythms in the liver

of animals subjected to chronic jet lag,[57] suggesting that mediation of PCGs and cortisol by pro-inflammatory cytokines should be included in the model for a liver subsystem.

It has been well established that cortisol functions as a critical driver for secretion of circadian cytokines, such as interferon γ (IFN-γ), interleukin 1 (IL-1), and TNF-α.[58] Furthermore, studies suggest a GR mediated cytokine inhibition, since experimental evidence shows that treatment with GR antagonist reduces expression of cytokines.[59-62] The inhibitory activity of the GR and cortisol complex is expressed in Equation (20). In the same equation, the indirect inhibition of BMAL1 is modeled to reflect the diurnal rhythms of PCG-mediated pro-inflammatory cytokines. Participation of BMAL1 in the cytokine rhythms is supported by Bmal1 mRNA experiments which found that BMAL1 deficient mice myeloid cells showed exacerbated immune responses and increased secretion of cytokines under challenges with endotoxin or bacteria.[63-65] After translation, cytokines bind to cytokine receptor and form a complex PR, which feeds back to the cytokine mRNA due to autocrine effects.[66] We simulated the effect of cytokine/cytokine receptor complex with an indirect response in Equation (20). The translation of cytokine mRNA is described by Equation (21). The translated cytokine protein stimulates the HPA-axis as previously mentioned, and also indirectly induces the translation of PER-CRY mRNA, which will be described later. The cortisol-mediated upregulation of cytokine receptors was modeled in Equation (22) as indirect stimulation of the receptor mRNA. Equation (23) describes the translation of cytokine receptor, and Equation (24) represents the dynamics of the cytokine/cytokine receptor complex.

While light/dark cycle entrains the PCGs via the cortisol-receptor complex, the feeding cycle entrains the PCGs via the NAD^+ and SIRT1. The mathematical representation of feeding entrainment on the PCGs involves the rhythmic response of NAD^+ and SIRT1 to feeding and fasting states, which react with multiple components in the circadian machinery. The dynamics of NAD^+ in the periphery is mainly driven by two reactions: 1) reduction to NADH; and 2) the NAD^+ salvage pathway. It is suggested that while feeding, continuous glycolytic throughput would result in the accumulation of NADH, and therefore limit the NAD^+ concentration. In contrast, fasting would decrease the glycolytic NAD^+ demand, resulting in higher NADH oxidation and higher NAD^+ concentration.[67] Therefore, in Equation (25) which describes the changing concentration of NAD^+ in the periphery due to food availability and the NAD^+ salvage cycle, feeding signal (through the transit compartments in Equations (2)-(3)) drives the inhibition term. The transit compartments for feeding were added to the model based on the experimental observations that NAD^+ level peaks 5-6 hours after the beginning of the active period in rat liver,[33] suggesting a delay in feeding signal modifying the redox reactions between NAD^+ and NADH. The regeneration of NAD^+ from NADH by oxidation reaction is modeled using Michaelis-Menten kinetics. In Equation (25), nad represents the combined concentration of NAD^+ and NADH together; therefore the quantity (nad-NAD) represents the concentration of NADH available to be oxidized, and the rate of NAD^+ regeneration is dependent on it. Aside from NADH oxidation, the NAD^+ salvage pathway is another way cells generate NAD^+, and the reactions are modeled using Michaelis-Menten kinetics in Equations (25)-(27). In the salvage

pathway, nicotinamide (NAM) is released from NAD^+ in ADP-ribose transfer reactions, represented as a degradation term in Equation (25) describing the change in NAD^+ concentration, and represented as a synthesis term in Equation (26) describing the change in NAM concentration. NAM is converted to nicotinamide mononucleotide (NMN) by rate-limiting enzyme nicotinamide phosphoribosyltransferase (NAMPT) catalyzation. Since the conversion of NAM to NMN is dependent on the availability of NAMPT, the synthesis term for NMN is multiplied by the NAMPT concentration in Equation (27). Finally, NMN is converted back to NAD^+ by an enzyme called nicotinamide mononucleotide adenylyltransferase (NMNAT), completing the cycle of the NAD^+ salvage pathway. Parameters describing reactions involving NAD^+ reduction and salvage cycle are estimated to capture the qualitative behaviour of NAD^+ and NAMPT based on food availability. One of the key features is that NAD^+ levels are high during fasting and become lower during feeding, but there is a delay of 5-6 hours between feeding start time and NAD^+ level decline.[68] NAMPT tends to peak shortly before the time when NAD^+ level peaks.[69] The estimated parameters ensures that these qualities are captured regardless of the presence of conflict between the light/dark cycle and feeding cycle.

NAD^+ acts the representative agent that communicates the energy state of the periphery to the SCN in our model. As mentioned previously, the electric signaling activity of vmARC is regulated by metabolically active hormones such as ghrelin, leptin, glucocorticoid, insulin, and their receptors, along with glucose.[43-49] Furthermore, tracer experiments using fluorophore-conjugated cholera toxin B (CTB) shows that the SCN is

one of the sites that are involved in reciprocal communication with the vmARC.[50] Therefore, we hypothesize that information about food availability in the periphery is transmitted to the SCN via electric signaling through the vmARC, and lump the hormonal and electric signaling activity into one transit compartment in Equation (28). This transit compartment, termed EntF, stimulates cortisol secretion in the HPA axis in the central compartment, in Equation (7). The parameters in Equation (7) were estimated to produce the food-anticipatory rise of cortisol upon food availability dis-synchronized to light. [51]

NAD^+ is also the activating agent of SIRT1. It is well established that NAD^+ activates SIRT1 by directly binding and altering the conformation of the catalytic site to allow binding of substrates, as the crystal structure of SIRT1 are in the active conformation.[70,71] Furthermore, SIRT1 is an attractive candidate to study in the context of metabolic diseases, both experimentally and *in silico* because multiple inhibitors and activators, such as indoles/indole derivatives[72] and resveratrol[73] were studied as possible therapeutics for cancer, obesity, and aging-related heart diseases.[74] The stimulating effect of NAD^+ on SIRT1 is modeled in Equation (29), using Mechaelis-Menten kinetics. The constant sirtT represents the total concentration of SIRT1 protein, both in the inactive conformation and the NAD^+ bound active conformation, and SIRT1 represents the activated SIRT1 enzyme. The production rate of active SIRT1 is dependent on the concentration of inactive SIRT1 protein availability as well as the activator (NAD^+) concentration. We model the dynamics of active SIRT1 in this manner because experimental evidence suggests that the total SIRT1 protein concentration stays relatively

constant while the enzymatic activity level oscillates with a circadian rhythm.[2] Estimation of parameters for Equation (29) captures that SIRT1 level peaks ~3 hours post the first food availability based on mouse liver data.[2]

So far, the environmental cues entrain the periphery through two different channels. The light/dark cycle entrains the cortisol rhythms in the central compartment through the HPA axis, which drives the dynamic of cortisol-receptor complex in the periphery. The feeding cycle entrains the dynamics of NAD^+ which communicates the cellular energy state to the SCN, and also the SIRT1 protein. The cortisol-receptor complex and SIRT1 are the two main entrainers of PCGs that will produce convoluted downstream effects, and their entrainment dynamics will be described.

The entrainment dynamics of the PCGs by cortisol are based on our previous work.[18] A network of transcriptional and translational feedback loops are incorporated into Equations (30)-(36) with important modifications to model the circadian rhythmicity of the PCGs, ultimately resulting in autonomous oscillations of the PCGs. Although these equations were originally developed for an immune subsystem such as macrophages or neutrophils, the rhythmic patterns and mechanism behind the core clock machinery involving the PER/CRY complex and CLOCK/BMAL1 complexes are similar across different tissues in the body,[9-12] and these equations are successful in describing the PCG behavior in the liver. The negative and positive feedback loops consisting of the two protein complexes have been implemented in mathematical modeling of a hepatocyte in another work,[75] further confirming that utilization of this mechanism in modeling hepatocyte is justified. In Equation (30), the entrainment of Per and Cry mRNAs by

cortisol is taken into account based on the consideration that cortisol and GR complex binds to the promotor region of the Per1 and Per2 genes.[76] The transcription of the Per and Cry genes is stimulated when CLOCK/BMAL1 complex binds to an Ebox enhancer. Additionally, translated PER/CRY protein translocates to the nucleus and inhibits its own translatioinal activity, forming a negative feedback loop. The exponent p to the PER/CRY protein in the nucleus in Equation (30) is a Hill-function coefficient, and is utilized to describe the switch-like behavior of the translational activities. The role of pro-inflammatory cytokines is also incorporated into this equation via indirect response, based on studies that show that Per1, Cry1, and Cry2 expressions are induced upon treatment with pro-inflammatory cytokines such as IL-6 or TNF-α.[77-79] The dynamics of PER/CRY protein is represented by Equation (31) and composes of the complex formation rate, degradation rate, and nuclear import and export rates. The PER/CRY protein dynamics inside the nucleus is governed by Equation (32), which is also described by the nuclear import/export rate as well as the degradation rate. When inside the nucleus, PER/CRY protein can also indirectly induce Bmal1 transcription,[80] and this relationship was modeled as a Hill equation with a coefficient r in Equation (33). The dynamics of the BMAL1 protein is dependent on translation, degradation, and nuclear import/export rates, as shown in Equation (34). Inside the nucleus, BMAL1(N) binds to the CLOCK protein, which is assumed to be in an access of BMAL1(N) in this model. The dynamics of BMAL1(N) and the CLOCK/BMAL1 complex are shown in Equations (35)-(36).

The feeding rhythms entrain the PCGs via NAD^+ and SIRT1 but the interaction between PCGs and NAD^+-activated SIRT1 is bidirectional. SIRT1 both exerts influence on the rhythms of some clock components while also being under the regulation of them at the same time. The activated SIRT1 protein binds to the CLOCK/BMAL1 complex, one of the key components that drive the core circadian machinery in the periphery. Once it forms the CLOCK/BMAL1/SIRT1 complex, it promotes the expression of NAMPT.[81] As previously mentioned, NAMPT controls the rate of regeneration of NAD^+ from the NAD^+ salvage cycle, the activator of SIRT1. Therefore, SIRT1 self-regulates its activation through interacting with core peripheral clock components. The dynamics of CLOCK/BMAL1/SIRT1 complex is modeled in Equation (37). In this equation k_{m8a} represents the association rate of CLOCK/BMAL1 complex and SIRT1, k_{m8d} represents the dissociation rate of CLOCK/BMAL1/SIRT1 complex back to CLOCK/BMAL1 and SIRT1, and k_{m9d} represents the degradation rate of this complex. The regeneration of CLOCK/BMAL1 from CLOCK/BMAL1/SIRT1 complex is presents in Equation (36). The dynamics of NAMPT are modeled in Equation (38), using first order production (k_{m10a}), and degradation (k_{m10d}) terms. Another influence of SIRT1 on the dynamics of the PCGs is taking away the availability of CLOCK/BMAL1 complex that promotes the expression of PER/CRY. Therefore, accumulation of activated SIRT1 enzyme will inhibit the translation of Per/Cry mRNA. SIRT1 affects the rhythm of PER/CRY with its deacetylating activity as well. In Equation (32), SIRT1 indirectly stimulates the nucPER/CRY degradation. This modification is introduced because SIRT1 is known to facilitate degradation of PER2 protein by deacetylation of PER2.[2,82] Supporting

experimental evidence also shows abnormally high PER2 accumulation in SIRT1-deficient mouse embryonic fibroblasts (MEFs).[83] Two steps were taken to estimate parameters describing interaction between core clock genes and metabolic components. First, parameters were optimized for correct phase relations of components relative to light under synchronized schedule. For example, it is well established that PER and CRY proteins peak in the morning time, or early active phase.[52,84,85] Once these conditions were met, the parameters were estimated once again at a state in which feeding was anti-synchronized to light. The new estimation would yield complete inversion of the metabolic components and PCGs,[51] and decrease in amplitude for PCGs.[53] For all estimation, PER/CRY protein complex was used as the representative sample for PCGs since PER/CRY rhythms are under close influence of both SIRT1 and nuclear cortisol-receptor complex.

In summary, our model utilizes SIRT1 as the key molecule that connects the cellular energy state resulting from feeding availability to the PCGs, whose rhythms are now entrained by signals from both light/dark and feeding/fasting cycles. The dynamics of NAD^+ (a SIRT1 activator) are modeled to reflect the change in redox reaction from feeding as well as the NAD^+ salvage cycle that takes input from the circadian dynamics from CLOCK/BMAL1 heterodimer. The interaction between SIRT1 and cortisol are also captured to reflect adjustments to the cortisol dynamics upon change in feeding schedule, introducing a modification to the HPA-axis.

$$\frac{dF_{periphery}}{dt} = \frac{1}{\tau} \cdot (F_{HPA} - F_{periphery}) \qquad (13)$$

$$\frac{dMR}{dt} = k_{MR}\left(\frac{\left(1+\frac{k_{F,MR}.F_{periphery}}{K_{F,MR}+F_{periphery}}\right)(MR_T - MR)}{K_{MR}+MR_T-MR}\right) - \frac{k_{MR,deg}.MR}{K_{MR,deg}+MR} - k_{b,MR}.F_{periphery}.MR + k_{re,MR}.FMR(N) \quad (14)$$

$$\frac{dFMR}{dt} = k_{on,MR}F_{periphery}.MR - k_{t,MR}FMR \quad (15)$$

$$\frac{dFMR(N)}{dt} = k_{t,MR}FMR - k_{re,MR}FMR(N) \quad (16)$$

$$\frac{dGR}{dt} = k_{GR}\left(\frac{\left(1+\frac{k_{F,GR}.F_{periphery}}{K_{F,GR}+F_{periphery}}\right)(GR_T - GR)}{K_{GR}+GR_T-GR}\right) - \frac{k_{GR,deg}.GR}{K_{GR,deg}+GR} - k_{b,GR}.F_{periphery}.GR + k_{re,GR}.FGR(N) \quad (17)$$

$$\frac{dFGR}{dt} = k_{on,GR}F_{periphery}.GR - k_{T,GR}FGR \quad (18)$$

$$\frac{dFGR(N)}{dt} = k_{T,GR}FGR - k_{re,GR}FGR(N) \quad (19)$$

$$\frac{dmRNA_P}{dt} = k_{mRNA_{P_{in}}}\left(1-\frac{k_{fr}.FGR(N)}{K_{fr}+FGR(N)}\right).\left(1-\frac{k_{pc}.BMAL1(N)}{K_{pc}+BMAL1(N)}\right).(1+PR) - k_{mRNA_{P_{out}}}.(mRNA_P) \quad (20)$$

$$\frac{dP}{dt} = k_{in_P}.mRNA_P - k_{out_P}.P \quad (21)$$

$$\frac{dmRNA_{R_P}}{dt} = k_{mRNA_{R_{P_{in}}}}\left(1+\frac{k_{fr2}.FMR(N)}{K_{fr2}+FMR(N)}\right) - k_{mRNA_{R_{P_{out}}}}.(mRNA_{R_p}) \quad (22)$$

$$\frac{dR_p}{dt} = k_{in_{R_p}}.mRNA_{R_p} - k_{out_{R_P}}.R_P - k_d.PR_p \quad (23)$$

$$\frac{dPR}{dt} = k_d.PR_p - k_{out_{PR_P}}.PR_p \quad (24)$$

$$\frac{dNAD}{dt} = \frac{k_{m1}(nad-NAD)}{K_{m1}+nad-NAD} + \frac{k_{m2}\cdot NMN}{K_{m2}\cdot +NMN} - \frac{k_{m3}\cdot feed3\cdot NAD}{K_{m3}+NAD} - \frac{k_{m4}\cdot NAD}{K_{m4}+NAD} \quad (25)$$

$$\frac{dNAM}{dt} = \frac{k_{m4} \cdot NAD}{K_{m4} + NAD} - \frac{k_{m5} \cdot NAMPT \cdot NAM}{K_{m5} + NAM}$$

(26)

$$\frac{dNMN}{dt} = \frac{k_{m5} \cdot NAMPT \cdot NAM}{K_{m5} + NAM} - \frac{k_{m2} \cdot NMN}{K_{m2} \cdot + NMN}$$

(27)

$$\frac{\mathrm{dEntF}}{\mathrm{dt}} = \frac{k_{m11} \cdot NAD}{K_{m11} + NAD} - k_{m12} \cdot EntF$$

(28)

$$\frac{dSIRT1}{dt} = \frac{k_{m6} \cdot NAD \cdot (sirtT - SIRT1)}{K_{m6} + sirtT - SIRT1} - \frac{k_{m7} \cdot SIRT1}{K_{m7} + SIRT1} - k_{m8a} \cdot CLOCK/BMAL1 \cdot SIRT1 + k_{m8d} \cdot CLOCK/BMAL1/SIRT1$$

(29)

$$\frac{dPer/Cry_{mRNA}}{dt} = \frac{v_{1b}(CLOCK/BMAL1 + c)}{k_{1b}\left(1 + \left(\frac{nucPER/CRY}{k_{1i}}\right)^{p}\right)}\left(1 + k_f.P\right) - k_{1d}.Per/Cry_{mRNA} + k_c \frac{FGR(N)}{CLOCK - BMAL1}$$

(30)

$$\frac{dPER/CRY}{dt} = k_{2b} \cdot Per/Cry^{q}_{mRNA} - k_{2d} \cdot PER/CRY - k_{2t} \cdot PER/CRY + k_{3t} \cdot nucPER/CRY$$

(31)

$$\frac{dnucPER/CRY}{dt} = k_{2t} \cdot PER/CRY \ - k_{3t} \cdot nucPER/CRY - k_{3d} \cdot nucPER/CRY \cdot (1 + SIRT1)$$

(32)

$$\frac{dBmal1_{mRNA}}{dt} = \frac{v_{4b} \cdot nucPER/CRY^{r}}{k^{r}_{4b} + nucPER/CRY^{r}} - k_{4d} \cdot Bmal1_{mRNA}$$

(33)

$$\frac{dBMAL1}{dt} = k_{5b} \cdot Bmal1_{mRNA} - k_{5d} \cdot BMAL1 - k_{5t} \cdot BMAL1 + k_{6t} \cdot nucBMAL1$$

(34)

$$\frac{dnucBMAL1}{dt} = k_{5t} \cdot BMAL1 - k_{6t} \cdot nucBMAL1 - k_{6d} \cdot nucBMAL1 + k_{7a} \cdot CLOCK/BMAL1 - k_{6a} \cdot nucBMAL1$$

(35)

$$\frac{dCLOCK/BMAL1}{dt} = k_{6a} \cdot nucBMAL1 - k_{7a} \cdot CLOCK/BMAL1 - k_{7d} \cdot CLOCK/BMAL1 - k_{m8a} \cdot CLOCK/BMAL1 \cdot SIRT1 + k_{m8d} \cdot CLOCK/BMAL1/SIRT1$$

(36)

$$\frac{dCLOCK/BMAL1/SIRT1}{dt} = k_{m8a}CLOCK/BMAL1 \cdot SIRT1 - k_{m8d} \cdot CLOCK/BMAL1/SIRT1 - k_{m9d} \cdot CLOCK/BMAL1/SIRT1 \quad (37)$$

$$\frac{dNAMPT}{dt} = k_{m10a}CLOCK/BMAL1/SIRT1 - k_{m10d}NAMPT \quad (38)$$

2.2.3 Sensitivity analysis

A sensitivity analysis was performed on the model to gain insight into the PCG dynamics predicted by our model. The analysis was performed under two different entrainer conditions, first with light and feeding signals aligned, and next with light and feeding signals anti-synchronized. We computed a relative sensitivity coefficient for every parameter, using Equation (39) below.

$$\frac{1}{NM}\sum_{j=1}^{NM}\frac{p_k}{y_{ij}}\left(\frac{\partial y}{\partial p_k}\right)_{y=y(t_{ij},p)} \quad (39)$$

In the above equation,

NM = number of measures

y = state variable whose response is being measured

p_k= parameter to be tested

Since we are most interested in studying the dynamics of PCGs where both light and feeding zeitgebers exert their influence, we used the profile of PER/CRY to calculate the sensitivity coefficients. Each parameter was varied by 1% and relative sensitivity

coefficients for each parameter based on the response variable's amplitude and phase angles were computed.

2.3 Results

Our in silico experiments aim to explore the change in dynamics of the peripheral clock machinery due to interactions of two independent entrainers, light and feeding. The schematics of the model including the HPA axis entrained by light, and the periphery representing a hepatocyte entrained by cortisol and feeding are shown in Figure 1. The redox reaction between NAD^+ and NADH receives the signal from feeding/fasting cycle, and the resulting NAD^+ dynamics stimulate the activation of SIRT1, which serves as a bridge between light and feeding entrainment. SIRT1 then interacts with the PCGs in a bidirectional manner, directly and indirectly regulating the rhythms of PER/CRY via binding and deacetylation reactions, while being under the influence of CLOCK/BMAL1 heterocomplex.

In Figure 2, the time profiles of cortisol (2B), PER/CRY protein (2C), and SIRT1 (2D) are shown over a period of 24 hours, under synchronized and anti-synchronized light and feeding schedules. Figure 2A shows the light and feeding signals under both conditions. Light signal was on from 6am to 6pm for both conditions. The feeding signal was also on from 6am to 6pm for the synchronized schedule, while the signal was on from 6pm to 6am, opposite from the light signal, for the anti-synchronized schedule. When feeding is synchronized to light, cortisol, PER/CRY protein, and SIRT1 all peak in the morning time, or during the early active period. In contrast, when feeding is anti-

synchronized to light, PER/CRY and SIRT1 phases are completely inverted, while cortisol peak shifts to the beginning of the inactive phase. Additionally, the amplitudes for cortisol and PER/CRY oscillations are smaller for the anti-synchronized schedule, compared to the synchronized schedule. These features are in qualitative agreement with restricted feeding studies performed on mice.[86,87] However, the amplitude of active SIRT1 does not undergo a change between the synchronized and anti-synchronized schedules, responding only in peak time.

We then explored how constant light signals at varying intensities will affect the PCGs under identical feeding signal. Feeding signal was on from 6am to 6pm whereas light signal was on for the entire time (Figure 3A). The resulting time profiles for cortisol, PER/CRY, and SIRT1 were compared against the light and feeding synchronized schedule in Figure 3. The results show that under constant light, cortisol (3B) and PER/CRY (3C) oscillate with reduced amplitudes compared to light/dark cycle synchronized to feeding. Applying constant light at brighter intensities caused a greater reduction of amplitude for cortisol and PER/CRY. This observation is in qualitative agreement with experimental observations in mice.[88] The phase angles for cortisol and PER/CRY were not affected by changing intensities of light. However, SIRT1 oscillations remained identical when applying different light schedules and intensities and exhibited no difference in amplitude or phase.

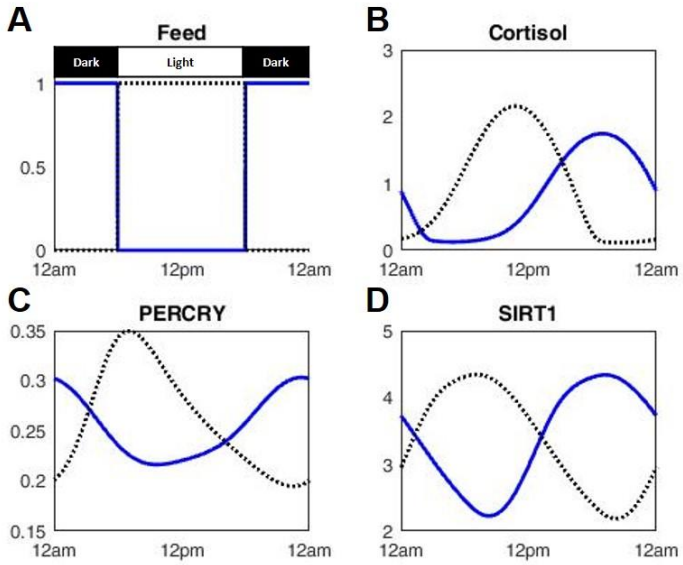

Figure 2: The time profiles of key components throughout the day upon synchronized (black dotted line) and anti-synchronized (blue line) light and feeding schedules. Light signal was at 1 from 6am to 6pm, and at 0 for the rest of the day. Feeding signals synchronized and anti-synchronized to light are shown in (A). The corresponding cortisol (B), PER/CRY protein (C), and SIRT1 (D) profiles are also shown.

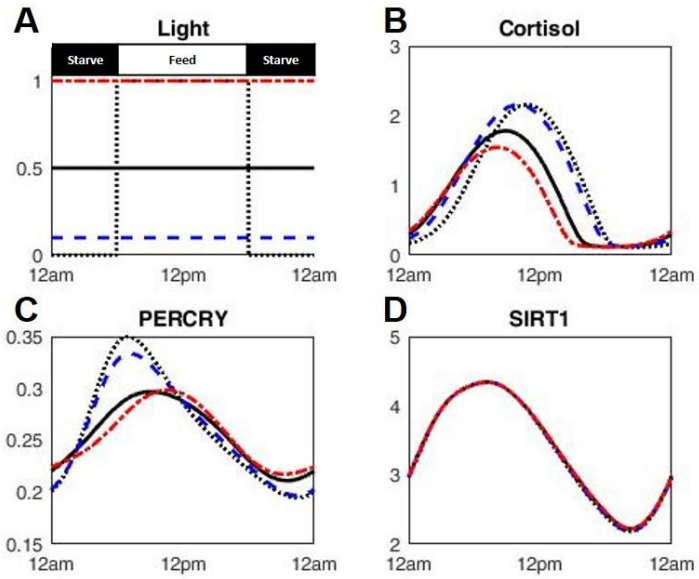

Figure 3: Time profiles of key components under constant light schedule at different intensities are compared. Feeding signal was at 1 from 6am-6pm, and at 0 for the rest of the day (A). Constant light signals at different intensities are also shown in (A), along with a control, in which feeding and light are synchronized. The cortisol (B), PER/CRY protein (C), and SIRT1 (D) profiles under the different light intensities are shown.

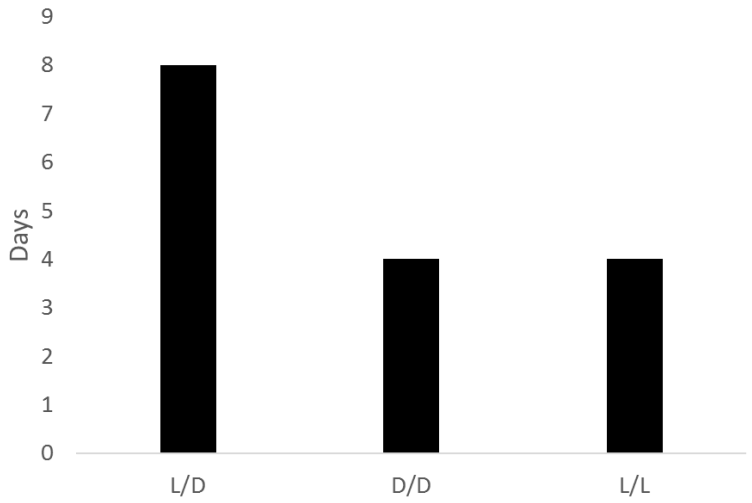

Figure 4: Number of days taken to first reach the steady state phase angle upon feeding inversion at different light schedules. L/D is 12-hour light, 12-hour dark cycle. D/D is a 24-hour dim light schedule with an intensity of 0.1. L/L is a 24-hour light schedule with an intensity of 1.

Imposing a constant light signal to the system not only results in a diverged PCG dynamics from the synchronized light/dark cycle, but also changes the system response when feeding signals are inverted. The transition time for feeding inversion under constant light conditions were calculated and are shown in Figure 4 along with the transition time under light/dark cycle. The transition time is defined as the number of days to first reach the steady-state phase relations after feeding inversion. Initially, the feeding signal was on from 6am to 6pm, and then switched to be on from 6pm to 6am at midnight. The phase angle, or the ew steady-state was first computed, and then each day's phase angle following feeding inversion was compared to the computed steady-state phase angle to determine when the PER/CRY rhythm first reached the steady-state phase angle. As Figure 4 shows, the phase inversion was achieved more quickly with constant light conditions at both bright (L/L) and dark (D/D) light intensities, compared to the light/dark cycle (L/D).

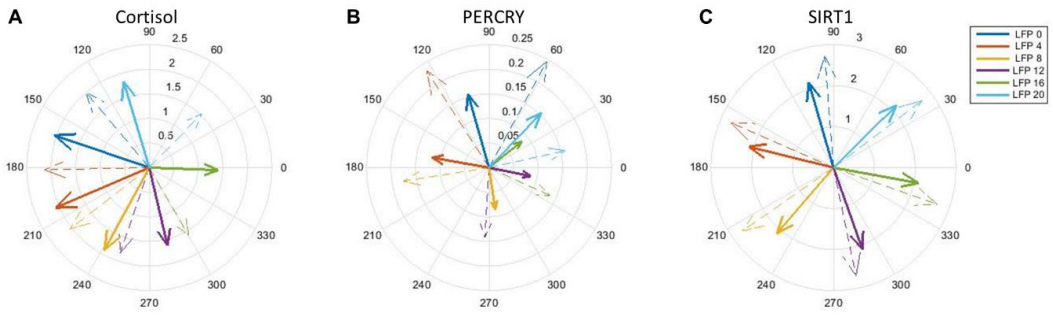

Figure 5: Amplitude and phase of cortisol (A), PERCRY protein (B), and SIRT1 (C) at various light-feeding phase relations (LFPs). Thick lines represent data with 12-hour feeding duration with an amplitude of 1, and thin dashed lines represent data with 6-hour feeding duration with an amplitude of 2.

In Figure 5, we tested the effects of phase relations between light and feeding signals under two different feeding durations. Either a 12h-duration feeding signal at an amplitude of 1 (represented by thick lines), or a 6h-duration feeding signal at an amplitude of 2 (represented by thin dashed lines) were applied with varying start time delays relative to light. The amplitudes for feeding signals with different durations were set such that the AUC of feeding for a given 24 hour period is identical between the two feeding durations tested. From the resulting dynamics, the amplitudes and phase angles for cortisol (5A), PER/CRY (5B), and SIRT1 (5C) profiles were shown in compass plots. The amplitudes are represented as the lengths of the arrowheads, and phase angles are represented as the directions of the arrowheads in the plot. The amplitude change for cortisol was observed with changes in phase relations between light and feeding, characterized by smaller amplitudes in the first and fourth quadrants compared to second and third quadrants. However, feeding duration did not affect the amplitude of cortisol as much as the effects caused by feeding delays. The largest percent difference between amplitudes caused by feeding duration was 14%, observed at the light-feeding phase difference of 20 hours. Compared to this case, the largest percent difference in amplitude

due to light-feeding phase difference was 62%, observed between 4 hours and 16 hours for the 12h-duration feeding. However, PER/CRY amplitudes were influenced both by feeding duration and feeding delays, characterized by the difference in lengths between thick solid and thin dashed arrowheads as well as the changing amplitude around the plot. For both feeding durations, amplitudes were higher when light-feeding phase difference was small (0-4 hours). Amplitudes decreased as phase difference increased, with a minimum at 16 hours of phase difference. For all light-feeding phase differences, amplitudes were greater for the 6h-duration feeding compared to 12h-duration feeding. Furthermore, feeding delays in 6h-duration schedule resulted in phase-jump behavior, characterized by irregular angles between each thick arrows. For example, in the 12h-duration feeding case, the difference in phase angle between 8h and 12h light-feeding phase difference is about 100 degrees, whereas that between 16h and 20h difference is less than 10 degrees. In contrast, SIRT1 phase angles strictly followed the feeding schedules, while amplitudes were identical for each feeding duration. SIRT1 amplitude for 6-hour duration was greater than that of the 12h-duration, due to difference in feeding signal strength.

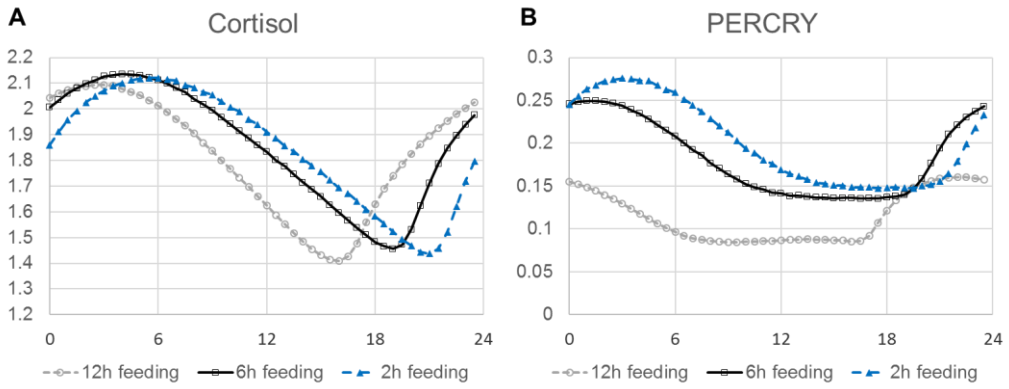

Figure 6: Amplitudes of cortisol (A) and PER/CRY (B) proteins are shown at different feeding delay times relative to light are shown.

To explore the effects of feeding duration and phase relative to light in more detail, the amplitudes of cortisol and PER/CRY were plotted along an axis of light-feeding phase difference at 30 minute intervals in Figure 6. A positive value of the light-feeding phase difference means that feeding signal was started after the start of light signal. Therefore, feeding was started at ZT0, ZT0.5, ZT1, ZT1.5, etc. Feeding duration of 12 hours at an amplitude of 1, 6 hours at an amplitude of 2, and 2 hours at an amplitude of 6 were tested, keeping the AUC of feeding identical over a 24h period. In Figure 6A, we observe that the cortisol amplitude is high when feeding starts shortly after light phase, and drops as feeding delay increases. The amplitude is at the maximum value when feeding is started at ZT3 for 12h-duration feeding, ZT4 for 6h-duration feeding, and ZT6 for 2h-duration feeding. The amplitudes reach the minimum values at feeding start time of ZT16 for the 12h-duration feeding, ZT19 for the 6h-duration feeding, and ZT23 for the 2h-duration feeding. The feeding delay time at the minimum amplitude is offset from the time of complete anti-synchrony between light and feeding, which is at ZT12. In Figure 6B, the amplitudes for PER/CRY protein are plotted in the identical

manner. The influence of feeding duration is apparent from this plot, as the amplitudes for shorter feeding duration is higher than those for longer feeding duration for most of the delay times, from ZT1 to ZT19. The PER/CRY protein oscillates with larger amplitude when feeding starts early morning, or a few hours before the light period starts. The PER/CRY amplitude is at maximum when feeding starts 2 hours before light under 12h-duration feeding schedule. For 6h-duration feeding, starting feeding at ZT1 gives the maximum amplitude, and starting feeding at ZT3 will give maximum amplitude for 2h-duration feeding. From then, amplitudes decline as feeding delay is increased. Unlike the cortisol, there is a range of delay times in which the PER/CRY oscillates at minimum amplitude. For example, a feeding start time between ZT7 and ZT17 will cause PER/CRY to oscillate at the minimum amplitude. Similar ranges exist for 6h- and 2h-duration feedings, and the ranges are centered around the delays exhibiting minimum correlation coefficients between light and feeding. The slopes leading to and exiting from the minimum ranges are asymmetric and can be characterized by a slow decline of amplitude and quick recovery of amplitude with increasing feeding delays.

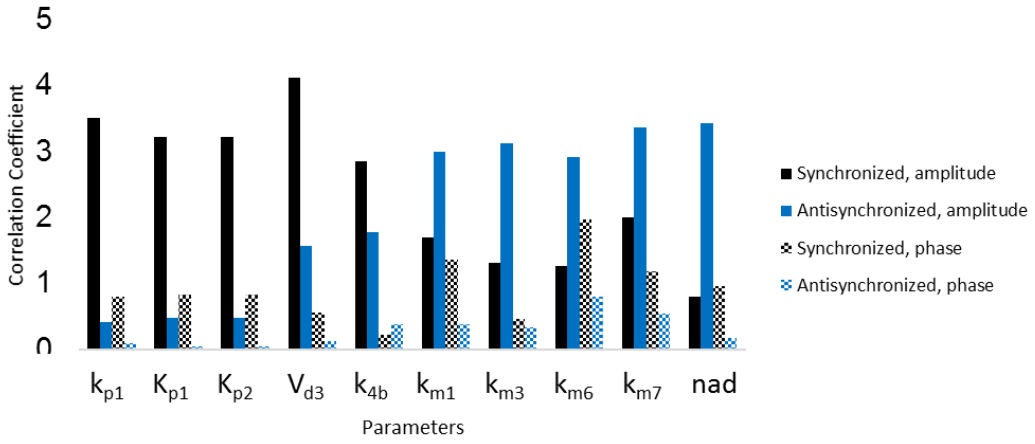

Figure 7: Sensitivity coefficients for PER/CRY protein under synchronized and anti-synchronized light and feeding signals. Sensitivity coefficients were calculated based on PER/CRY amplitude and phase angles.

Sensitivity coefficients for PER/CRY protein amplitude and phase were computed using Equation (39), once with synchronized light and feeding signals and another time with anti-synchronized light and feeding signals. In Figure 7, the parameters with 5 largest sensitivity coefficient for each condition based on PER/CRY amplitude were selected, and their sensitivity coefficients under both conditions are shown. When light and feeding signals were synchronized, the most sensitive parameters were k_{p1}, K_{p1}, K_{p2}, V_{d3}, and k_{4b}. Among these parameters, the first four are associated with the Goodwin oscillator in the HPA axis. Last parameter k_{4b} is the Michaelis constant for Bmal1 transcription. When light and feeding signals are anti-synchronized, k_{m1}, k_{m3}, k_{m6}, k_{m7}, and nad appear to be most sensitive to perturbations. Among these parameters, k_{m1}, k_{m3}, and nad are associated with the dynamics of NAD^+ concentration in the periphery. The other two parameters, k_{m6} and k_{m7}, describe the dynamics of activated SIRT1. Finally, the amplitude of PER/CRY protein was more sensitive than phase angle when the parameters

were perturbed, under both synchronized and anti-synchronized light and feeding conditions.

2.4 Discussion

The role of circadian rhythms on metabolic activity has been well established in mammals. Maintaining homeostasis of plasma glucose level throughout the day is extremely important for mammals since insufficient or excessive glucose levels can have detrimental effects on key biological functions such as neuronal activity and balancing of body fluid and electrolytes.[89] Important metabolic pathways that contribute to steady glucose level, such as gluconeogenesis and glycogen metabolism, are linked to proper functioning of the peripheral clock machinery.[21,22] Lipid metabolism has also shown to exhibit circadian activities[90] while also being regulated by BMAL1,[91] a core component of the feedback loop that creates circadian rhythms. Therefore, it is not surprising that circadian disruption can result in metabolic syndrome[6] or that animals with metabolic syndromes exhibit attenuated circadian rhythms in the periphery.[92] Although the metabolic implications from circadian disruption may manifest through multiple unknown mechanisms, there are some distinguishing effects on the clock genes upon changes in meal timing. One of the common and well-established observations is that restricting food access to the animals' rest period can re-entrain the circadian rhythms in the periphery to be synchronized to the feeding schedule, uncoupling the rhythms of the periphery from the central clock in the SCN. More specifically, when mice with pancreatic adenocarcinoma had 4 hours of access to food during the light period, PER2 and BMAL1 peaks were advanced by 8 hours.[93] In another study, diurnal fed mice

showed completely inverted expression of D-site binding mRNA and protein responsible for some clock output genes.[94] Furthermore, the phase inversion in the periphery is achieved whether the animals are subject to a 12-hour light, 12-hour dark (LD) cycle, or a constant dark (DD) schedule. When feeding time was advanced by 7 hours in mice, the peaks for Per1 and Per2 mRNA, D-site-binding protein, and Cyp7A mRNA in the liver were advanced by 6-12 hours.[53]

As Figure 2 shows, our model predicts that cortisol peak will be pushed to the beginning of the feeding time. At the same time, PER/CRY protein rhythms will completely invert upon feeding inversion, re-entraining to the new feeding schedule. The peak was shifted from early active phase to early rest phase, consistent with the literature data. A loss of amplitude is also observed for the PER/CRY rhythms, also consistent with findings that feeding exclusively during rest phase results in reduced oscillations for PER2.[53] The complete re-entrainment of PER/CRY rhythms to feeding is achieved through two major channels in our model. First, feeding-entrained NAD^+ affects the synthesis of cortisol through a transit compartment, EntF. As a result, cortisol exhibits an altered rhythmic pattern (Figure 2B), peaking near the feeding start time. The peak-delay behavior is reflective of the food-anticipatory rise in glucocorticoid levels in mice subjected to altered feeding schedules.[95] Unlike PER/CRY, cortisol rhythm is not completely shifted by 12 hours because it is strongly entrained by the light signal in the HPA axis. Light negatively regulates the CRH, which promotes ACTH, which in turn stimulates the release of cortisol. The cortisol-receptor complex promotes the expression of PER/CRY with the delayed rhythm, pushing the peak location of PER/CRY back.

However, altered cortisol profile alone cannot explain the complete 12h phase shift of PER/CRY, since the cortisol peak was not shifted by 12 hours. The complete phase inversion is achieved by the re-entrainment of CLOCK/BMAL1 heterocomplex by SIRT1. In our model, SIRT1 binds to CLOCK/BMAL1 to form CLOCK/BMAL1/SIRT1 complex, which serves as a transcription factor for NAMPT. Therefore, SIRT1 depletes the pool of CLOCK/BMAL1 complex and delays the peak time. Since CLOCK/BMAL1 promotes the transcription of Per/Cry genes, the peak time of PER/CRY protein is further delayed and achieves a complete 12h inversion.

We hypothesized that imposing a constant light condition will result in attenuated amplitudes for cortisol and PER/CRY rhythms, while improving the transition time between feeding rhythm changes. As Figure 3 shows, we confirmed that constant light signals result in reduced amplitudes for cortisol and PER/CRY rhythms. However, SIRT1 amplitude or phase was unaffected by the light intensity, because it is tightly controlled by the feeding-entrained NAD^+. While all constant light at all intensities result in lower amplitude oscillations for cortisol and PCGs, the intensity of the constant light signal affects their dynamics. Higher light intensity, or bright light, attenuates the oscillation amplitude more than dim light. This prediction agrees with experimental findings in mice.[88] Light signal entrains the cortisol by facilitating the degradation of CRH in Equation (5). Brighter light will result in greater degradation of CRH, which yields lower production of ACTH and therefore less cortisol (Figure 3B). Since the PCGs are entrained by cortisol in the periphery, the PER/CRY amplitude is reduced more under bright light in return. Imposing constant light signal also alters the transition time of the

PCGs upon feeding inversion. As Figure 4 shows, the PCGs adjust to the new feeding pattern more quickly under constant light condition than a 12h light, 12h dark cycle. This model behavior is consistent with the experiment that in mice carrying glucocorticoid receptor null alleles exclusively in the hepatocytes, the PCGs in the liver entrain much faster to the feeding regimen compared to the wild-type mice.[95] Since cortisol and cortisol receptor interaction is essential in entraining the PCGs by light, we rationalize that removing the light schedule creates a similar environment *in silico*, and observe that faster entrainment to feeding is achieved under constant light conditions. In our model, transition time is faster under constant light because the light/dark cycle acts as a conflicting entrainer and inhibits the transition to the feeding regimen.

In Figure 5, our model predicts that restricting feeding to a few hours during the active period results in higher amplitude oscillations for the peripheral clock machinery. In this figure, two different feeding durations (12h and 6h) with identical AUC over a given 24h period were tested at varying start times relative to light. The PER/CRY amplitudes are the highest when a 6h-duration feeding is started at ZT0 and ZT4 (Figure 5B). The prediction is in qualitative agreement with animal studies. When a mouse model of diet-induced obesity was subjected to 8h restricted feeding during the active phase, Per2 and Bmal1 mRNA oscillations were enhanced with increased amplitudes, for both high-fat-content and normal diets.[96] The increase in amplitude with shorter feeding duration is most likely due to the increased amplitude in the oscillation of SIRT1. If the feeding duration is shortened, the intensity of feeding signal has to be higher to compensate for the short duration and provide identical AUC of feeding to the system.

Since SIRT1 is directly activated by NAD^+ which is closely tied to feeding signals, SIRT1 amplitude also increases under shorter feeding duration, as shown in Figure 5C. Then, the SIRT1 dynamics will affect PER/CRY rhythms by facilitating the degradation rate inside the nucleus, eventually decreasing the protein's self-inhibitory effect on its own transcription rate (Equation (30)). In addition to the feeding duration, feeding start time relative to light also affects the amplitude of PER/CRY oscillation. For 12h feeding duration, starting feeding between ZT8 and ZT16 resulted in low amplitude oscillations, while feeding start time of ZT12 to ZT20 resulted in low amplitude oscillations for 6h-duration feeding. The light-feeding phase differences that yields low amplitude PER/CRY oscillations also result in lower amplitude oscillations for cortisol (Figure 5A). This phenomenon is due to that light and feeding both exert influence on cortisol, much like PER/CRY, although the light entrainment is much stronger in cortisol secreted from the HPA axis. We also observe from Figure 5 that phase angles progress through the feeding start time in different ways for cortisol, PER/CRY, and SIRT1. The irregularities in phase angles is expected since amplitude death in coupled limit-cycle oscillators are associated with phase-flip behavior,[97] where the phase angle between the two oscillators, or the difference in acrophases, suddenly increases at a threshold difference between the external entrainers. SIRT1's phase angles over the varying feeding start times are evenly spaced, because it is mainly entrained by the feeding signal alone. However, PER/CRY and cortisol phase angles progress through the feeding start times at varying angles, since they are coupled to both light and phase signals entering externally.

In Figure 6, the amplitudes for cortisol and PER/CRY through the varying feeding start times are shown in more detail, to identify which light-phase phase relations would yield the highest and lowest amplitude oscillations. Simulation of the model was performed at 30 minute intervals at three different feeding durations (12 hours, 6 hours, and 2 hours). The amplitudes of the feeding signals were adjusted to match the AUC of feeding signal over a 24h period. From Figure 6A, cortisol oscillation amplitudes exhibit identical trends among the three feeding durations where they are initially high when feeding starts soon after the light starting time, decline slowly to reach a minimum, and then recover to the maximum amplitude quickly. However, the specific feeding start time that gives the maximum and minimum amplitudes are different for every feeding duration. For example, under 12h feeding duration condition, the maximum amplitude is reached at feeding start time of ZT3 and the minimum is reached at ZT16. But these are not the times that give maximum and minimum amplitudes for 6h or 2h feeding durations. Interestingly, 12h delay, or complete inversion between light and feeding, does not result in the most reduced oscillation of cortisol. Such asymmetry is observed for PER/CRY amplitude profiles (Figure 6B), but manifested in a different way. Our model predicts that there is a range of feeding start times where PER/CRY amplitudes are also at a minimum value for each feeding duration. For the 12h duration, this minimum range is centered around feeding start time at ZT12. However, the slope of the amplitude profiles before and after the minimum values are asymmetric. The amplitude slowly declines to the minimum, and then recovers fast to reach the maximum either at the end of the dark period or the beginning of the light period. Considering the characteristics of

PER/CRY and cortisol together, these results suggest that starting to eat earlier in the day will give more robust circadian rhythms in the periphery than starting to eat later in the day. The model prediction is consistent not only with the common belief that late-night snacks are disadvantageous for the health, but also with studies where distributing more calories to breakfast resulted in more weight loss under the same caloric intake.[98] Furthermore, amplitude death in coupled limit-cycle oscillators are associated with phase-flip behaviour,[97] where the phase angle between the two oscillators suddenly increases at a threshold difference between the external entrainers. In a symmetric system, where the entrainer strength and the coupling strength between the two oscillators are identical, the phase-flip is centered around 12h delay between the entrainers, provided that the oscillations have a 24h period.[99] However, the timing of phase-flip moves when either the relative strengths of entrainers or the coupling strengths are asymmetric. Integrating these observations, the offset of the minimum cortisol amplitude and asymmetric PER/CRY profile may suggest that our model is an asymmetric system whose entraining strengths of light and feeding are transmitted to the PCGs with different efficiencies. Since the PCGs eventually entrain to the feeding cycle and cortisol peak is phase delayed by 7-8 hours upon a 12h feeding inversion, feeding signals have a greater impact on the downstream events than the light entrainment on the PCGs.

The sensitivity analysis reveals that different sets of parameters have highest sensitivity coefficients under synchronized and anti-synchronized light and feeding signals. When the two external signals are synchronized, parameters associated with the

Goodwin oscillator describing the production of cortisol in the HPA axis have the highest sensitivity coefficients, as shown in Figure 7. These parameters include k_{p1} and K_{p1}, each describing the CRH production and dissociation rates, K_{p2} which estimates dissociation rate of ACTH, and V_{d3}, which describe the rate of cortisol degradation. Together these parameters affect the dynamics of the light-entrained negative feedback loop in the HPA axis (Equations (5)-(7)), and it is expected that these parameters are among the most sensitive parameters, since the secreted cortisol entrains the downstream peripheral clock genes. Parameter k_{4b}, the Michaelis constant of Bmal1 transcription, also has a high sensitivity coefficient, likely due to SIRT1 - BMAL1 binding interaction as well as its involvement in controlling the dynamics of the pro-inflammatory cytokines. The pro-inflammatory cytokine dynamics and BMAL1 dynamics both directly affect the transcription of Per/CRY, leading to higher sensitivity. When light and feeding are anti-synchronized, parameters related to feeding entrainment exhibit higher sensitivity coefficients. This is likely due to that in the anti-synchronized state, feeding entrainment decouples the peripheral clock genes and cortisol from the Goodwin oscillator from the HAP axis, exerting more influence on the downstream events. Parameters k_{m1}, k_{m3}, k_{m6}, k_{m7}, and nad appear to be most sensitive to perturbations. Among these parameters, km1, km3, and nad are associated with the dynamics of NAD^+ concentration in the periphery. Parameter k_{m1} is the maximum extend of NADH converting to NAD^+, and k_{m3} describes the same for NAD^+ converting to NADH upon feeding. The combined concentration of NAD^+ and NADH is parameter nad. The other two parameters, k_{m6} and k_{m7}, describe the dynamics of activated SIRT1. They each describe the maximum extent of SIRT1

activation mediated by NAD+, and maximum extent of SIRT1 degradation. SIRT1 is one of the key components in our model, since it delivers the feeding signal to the peripheral clock machinery. Therefore, the sensitivity caused by SIRT1 is due to multiple interactions SIRT1 has with the PCGs. One of the ways in which SIRT1 interacts with the PCGs is by binding to the CLOCK/BMAL1 complex to form the CLOCK/BMAL1/SIRT1 complex, which drives the expression of NAMPT. Meanwhile, the CLOCK/BMAL1 complex is involved in the promotion of PER and CRY expression. Additionally, the amplitude of the PCGs appears to be more sensitive than the phase angle of the PCGs, indicating that the phase relations achieved by the two entrainers, light and feeding, are robust, while the oscillatory strength can change due to perturbations to the parameters.

In summary, our model qualitatively captures the key features of feeding-entrained peripheral clock machinery. Through the simulations, we could relate the robust circadian rhythms under short duration feeding in active phase to the higher amplitude oscillation of SIRT1, due to strong but short feeding signal. Our prediction suggests that controlling the dynamics of SIRT1 may be helpful in restoring or strengthening the oscillations of the peripheral clock machinery, also supported by a study on methylselenocystein (MSC), where restored NAD^+ oscillations and enhanced SIRT1 activity resulted in restoration of circadian rhythms of rat mammary tumor model.[100] Our model also predicts that the phase relation between light and feeding plays an important role in determining the oscillation amplitude for the PCGs, highlighting the need to study the metabolic implications caused by the interplay between these two environmental cues. Furthermore,

analysis of the model suggests that the reason best feeding time lies earlier in the active phase may be due to the asymmetry between the efficiencies of light and feeding entrainment of the PCGs. Future work could involve studying further downstream metabolic activities such as hepatic gluconeogenesis and lipogenesis to explore the changing dynamics of energy homeostasis in relation to other metabolic genes such as mTOR and AMPK under circadian disruption. Clearly a number of issues remain to be further examined, including but not limited to, assessing the impact of nutritional composition as well as multiple patterns of metabolic rhythms, such as simulating multiple meals etc. A limitation of the model is that the role of melatonin is not incorporated, although this important SCN-entrained hormone appears to have an influence over glucose metabolism by regulating insulin secretion and protecting against reactive oxygen species.[101]

CHAPTER 3: Dynamics of hepatic gluconeogenesis under conflicting *zeitgebers*

3.1 Introduction

Gluconeogenesis takes place in the liver for mammals to synthesize glucose from non-carbohydrate sources such as pyruvate, lactate, glycerol, alanine, and glutamine.[20] Although a chain of many reactions are required for the full process, observing key enzymes such as PEPCK and G6Pase can provide an insight into the link between circadian rhythms and gluconeogenesis. Glucose homeostasis and gluconeogenesis has been linked to dynamics of circadian genes through core clock gene knock-out

experiments. In a mouse study in which liver-specific Bmal1 knock-out was introduced, the animals showed altered rhythms for gluconeogenic genes.[21] The altered rhythms resulted in lower level of glucose during the late fasting phase for the knock-out animals compared to the control animals. The expression level of Cry1 and Cry2 proteins in the liver had an effect on the glucose level in another study.[22] Clock knock-out studies were performed by various groups as well, although the effects on glucose levels are conflicting depending on the enironmental and experimental factors.[23] SIRT1 and cortisol both promote the transcription of gluconeogenic genes. SIRT1 deacetylates PGC-1α, which then activates FOXO1. FOXO1 physically binds to the promotor region of the gluconeogenic gene and is required for transcription. Cortisol and the cortisol receptor complex binds to the GRE on the promotor of the gluconeogenic gene to promote transcription as well. In summary, the transcription of gluconeogenic genes are dependent on the levels of peripheral clock components and molecules that entrain the PCGs such as cortisol and SIRT1. Therefore, it is anticipated that environmental cues that influence the dynamics of the PCGs can also alter the gluconeogenic patterns.

To that end, we developed a semi-mechanistic, mathematical model to study the intertwined network of circadian clocks and metabolism, focusing on hepatic gluconeogenesis as the circadian modulated metabolic activity. Although we recognize that alteration or *Pck1* and *G6pc* expression may not be enough to describe changes in gluconeogenesis, we use the transcription of these two genes to represent hepatic gluconeogenesis as alterations in expression leads to changes in enzymatic activity [102]. During long-term fasting (>6 hours), SIRT1 activity results in increased transcription of

these two genes. SIRT1-mediated deacetylation activates PPARγ-coactivator α (PGC-1α) and Forkhead box O1 (FOXO1) [28]. These two proteins, along with hepatic nuclear factor-4α (HNF-4α), are required for transcription of gluconeogenic genes [31]. Furthermore, it is well established that serum cortisol level increases gluconeogenesis in humans [24]. When a high dose of cortisol is administered to overnight fasted dogs and increase the serum cortisol level, both the blood glucose level and glucose production elevate, where more than 65% of the increase in glucose production is due to gluconeogenesis [25]. This phenomenon is consistent in *ex vivo* studies, where cortisol doubled the net gluconeogenesis in fetal rat liver explants [103].

Based on the aforementioned observations, we propose a mathematical model that describes the interactions among various signaling molecules such as cortisol, SIRT1, PGC-1α, and their influence on hepatic gluconeogenesis, to study the effects of light and feeding cycles on circadian dynamics of the peripheral metabolism. We validate the model by generating predictions under various combinations of feeding and light patterns and comparing them to known behaviors under *ad libitum* feeding and time-restricted feeding conditions. Then, we utilized the model to test the effects of circadian disruption on transcription of gluconeogenic genes and to investigate various non-pharmacological methods to overcome the effects of circadian disruption. We first perturb the model by simulating a knockout (KO) condition for the peripheral clocks, then tested if a change in the feeding pattern can alter the effect of knockout Recognizing that the model is composed of a complex network of regulations involving transcription and translation, we analyze the model using three different approaches: local sensitivity analysis, global

sensitivity analysis using the Morris method, and uncertainty analysis using the random-sampling high dimensional model representations (RS-HDMR). From the sensitivity analysis results, we identify local targets that can overcome the effects of genetic clock knockout. Our model predicts that abnormally high level of fasting gluconeogenesis caused by *Clock* gene can be brought down to the wild type level by changing the feeding time relative to the light/dark cycle. Furthermore, the three different methods of sensitivity analysis consistently show that the dynamics of peripheral clocks (PER/CRY complex), cortisol-receptor complex, and PGC-1α are the most influential in rhythmic expression of gluconeogenic genes.

3.2 Methods

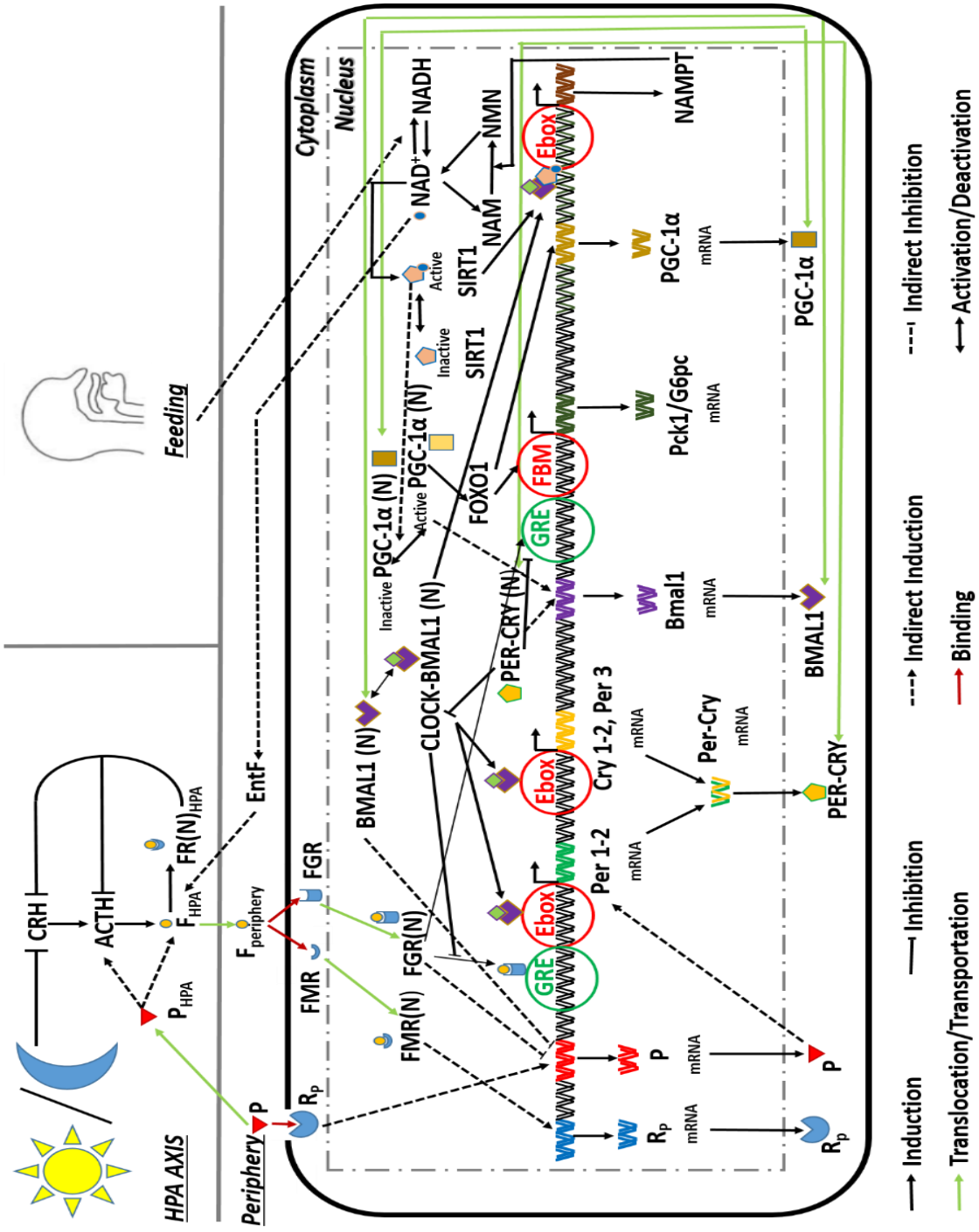

Figure 8: Schematic of the model depicting gluconeogenesis entrained to light and feeding.

We developed a mathematical model that represents a sequence of events describing the circadian dynamics of clock genes and metabolic activities in a human hepatocyte to study the manifestation of two external stimuli, the light/dark cycle and feeding/fasting cycle. The model was built upon our previous works [18,32,104] and is composed of a central compartment that receives and processes the environmental cues, and a peripheral compartment that encompasses the core clock machinery and metabolic gene expression. Only the essential parts of the model directly relevant to gluconeogenic gene expression is described in this section. A complete schematic showing the major driving forces for gluconeogenic gene expression is shown in Figure 8. A working version of the model is deposited in a Git Hub repository: https://github.com/AndroulakisGrp/SB_Gluconeogenesis.

3.3 Incorporation of environmental signals

The photic input from the light/dark cycle is received and processed by the HPA-axis, and entrains the daily rhythms of cortisol release to the periphery [18,32]. The light/dark cycle is modeled as a step function in our model as shown in Equation (40), much like earlier studies incorporating a similar *zeitgeber* [18,36,104,105]. In the HPA-axis, CRH, ACTH, and cortisol are modeled with a Goodwin oscillator modified with Michaelis-Menten kinetics with self-sustained oscillations, entrained by the light/dark cycle. Equations (41)-(43) represent the HPA-axis activity where light-regulated CRH induces secretion of ACTH in the anterior lobe of the pituitary gland, and ACTH acts on the adrenal cortex to produce cortisol. Cortisol then exerts negative regulatory effect on CRH and ACTH, completing the negative feedback loop. The rationale for including the

pro-inflammatory cytokines (P_{HPA}) as well as the secretion of cortisol to the periphery, cortisol's entraining actions on PCGs, and the cortisol receptor ($FR(N)_{HPA}$) dynamics are described in detail in our previous work [104]. Estimated parameter values are reported in Table A2 in the appendix.

The feed/fasting cycle is represented as a step function in Equation (44), similarly to the light/dark cycle. Feeding signal is processed through two transit compartments shown in Equations (45)and (46), each with a delay (τ_f) of 3 hours, eventually controlling the NAD^+ oscillations in the periphery by modifying the redox relations and changing the cellular NAD^+/NADH ratio. The purpose of the transit compartment in the model is to reflect the experimental observation that peak of NAD^+ level occurs 5-6 hours after the beginning of the active phase in rat liver [33]. The dynamics of NAD^+ level is governed by Equation (47). In the first term of this equation, nad represents the sum of NAD^+ and NADH amount; therefore the quantity (nad-NAD) represents the NADH available for conversion to NAD^+. The second term of Equation (47) represents the NAD^+ amount recovered from the NAD^+ salvage cycle. In this term, NMN represents the nicotinamide mononucleotide, the precursor to NAD^+ in the salvage cycle. The third term incorporates the effect of nutrient availability to the NAD^+ dynamics, and the fourth term represents NAD^+ lost due to entering the salvage pathway. Equation (48) describes the activation of SIRT1 by coenzyme NAD^+ [106]. In this equation, sirtT represents the total (active and inactive) amount of SIRT1 available in the cell; therefore the quantity (sirtT-SIRT1) indicates the availability of inactive SIRT1 to be activated by NAD^+. This term was constructed because the protein concentration stays constant throughout the day

while its activity level fluctuates [2]. The second term of this equation represents the degradation, and the third and fourth terms describe the binding of SIRT1 to the CLOCK/BMAL1 complex, which is a critical component in the peripheral clock machinery. The details for bi-directional interaction between SIRT1 and clock genes, as well as the description of peripheral clock network of the model, are available in our previous work [104] and the repository.

$$light = \begin{cases} 1, & 6AM \le t < 6P \\ 0, & 6PM \le t < 6AM \end{cases} \quad (40)$$

$$\frac{dCRH}{dt} = \frac{k_{p1}}{K_{p1} + FR(N)_{HPA}} - V_{d1} \cdot \frac{CRH \cdot \left(1 + \frac{light}{1 + light}\right)}{K_{d1} + CRH} \quad (41)$$

$$\frac{dACTH}{dt} = \frac{k_{p2} \cdot CRH}{K_{p2} + FR(N)_{HPA}} (1 + k_{fp} \cdot P_{HPA}) - V_{d2} \cdot \frac{ACTH}{K_{d2} + ACTH} \quad (42)$$

$$\frac{dF_{HPA}}{dt} = k_{p3} \cdot ACTH \cdot \left(1 + k_{fp} \cdot P_{HPA}\right) \cdot k_n \cdot (1 + \frac{EntF}{1 + EntF}) - V_{d3} \cdot \frac{F_{HPA}}{K_{d3} + F_{HPA}} \quad (43)$$

$$feed = \begin{cases} 1, & 6AM \le t < 6PM \\ 0, & 6PM \le t < 6AM \end{cases} \quad (44)$$

$$\frac{dfeed2}{dt} = \frac{1}{\tau_f}(feed - feed2) \quad (45)$$

$$\frac{dfeed3}{dt} = \frac{1}{\tau_f}(feed2 - feed3)$$

(46)

$$\frac{dNAD}{dt} = \frac{k_{m1}(nad - NAD)}{K_{m1} + nad - NAD} + \frac{k_{m2} \cdot NMN}{K_{m2} \cdot + NMN} - \frac{k_{m3} \cdot feed3 \cdot NAD}{K_{m3} + NAD} - \frac{k_{m4} \cdot NAD}{K_{m4} + NAD}$$

(47)

$$\frac{dSIRT1}{dt} = \frac{k_{m6} \cdot NAD \cdot (sirtT - SIRT1)}{K_{m6} + sirtT - SIRT1} - \frac{k_{m7} \cdot SIRT1}{K_{m7} + SIRT1} - k_{m8a} \cdot CLOCK/BMAL1 \cdot SIRT1 + k_{m8d} \cdot CLOCK/BMAL1/SIRT1$$

(48)

3.4 Expression of gluconeogenic genes

In our model PGC-1α is a key molecule that incorporates the effects of feeding to the transcription of gluconeogenic genes such as *Pck1* and *G6pc*. PGC-1α is involved in regulation of multiple aspects of biological programs, and its function differs in the cellular context. In mitochondria, it stimulates oxidative metabolism in brown fat and skeletal muscles [107]. It is also involved in cytokine or LPS induced increase in respiration and expression of genes associated with mitochondrial uncoupling and energy expenditure [108]. Since glucose uptake is influenced by the rates of mitochondrial oxidation [109], PGC-1α is expected to play a significant role in glucose homeostasis. Indeed, diabetic mice show an enhanced activity of PGC-1α, contributing to the increased hepatic glucose output associated with diabetes [28]. Studies show that PGC-1α expression in liver is increased under fasting condition [31,110]. Moreover, primary hepatocytes infected with adenoviruses encoding for PGC-1α stimulated key genes of gluconeogenesis, including PEPCK and G6PC (51) [31]. Studying the PEPCK promoter structure elucidated

to the mechanism of PGC-1α mediated stimulation of gluconeogenic enzyme expression. Co-activation of HNF-4α, FOXO1, and glucocorticoid response element (GRE) appear to be important in initiating transcription of the *Pck1* gene [111]. Under long-term fasting (>6 hours) condition, SIRT1 deacetylates PGC-1α, a coactivator for HNF-4α and FOXO1, to drive the expression of gluconeogenic genes [28]. PGC-1α binds and co-activates FOXO1 in a manner inhibited by Akt-mediated phosphorylation.

We describe the dynamics of PGC-1α in Equations (49)-(52). Equation (49) describes the dynamics of PGC-1α mRNA. Reporter assays show that FOXO1 stimulates PEPCK promoter activity by interacting with the insulin response sequences (IRSs) on the promoter region, which is reflected as a linear term in Equation (49). Equation (50) represents the translated PGC-1α protein. The dynamics of PGC-1α protein is dependent on the transcription rate (k_{g3b}) of PGC-1α mRNA, degradation rate (k_{g3d}) of the protein, and import (k_{g3t}) and export (k_{g4t}) rates to the nucleus. Equation (51) governs the dynamics of PGC-1α once the protein is translocated to the nucleus. Finally, Equation (52) represents the SIRT1-activated PGC-1α protein. The binding (k_{g5}) and dissociation (k_{g8d}) of SIRT1 as well as the degradation (k_{g8}) of active PGC-1α is modeled in a linear manner. Then, the co-activation of FOXO1 and HNF-4α is lumped into a single variable, FOXO1, for the purpose of simplicity in Equation (53). The level of FOXO1 is dependent on the activation by PGC-1α (k_{g9}) and deactivation (k_{g10}) of activated FOXO1.

The activated FOXO1 binds to a DNA motif upstream of the gluconeogencic genes and activates the transcription of these genes [111,112] (Equation (54)).

Glucocorticoid receptor (GR) is also required along with HNF-4α and PGC-1α for full activation of PEPCK promoter, reflected in the first term of Equation (54). The cortisol-receptor complex binds to the GRE region in the promoter of the gluconeogenic genes to stimulate transcription [111]. This binding reaction appears to be under the influence of CRY proteins in the nucleus. In a study with mice fibroblasts, *Cry* 1 and 2 deficiency doubled the number of dexamethasone-induced genes, along with glucose intolerance and constitutively high levels of circulating corticosterone [27]. In the same study, CRY antibody experiments revealed that CRY proteins interact with glucocorticoid receptors in the liver after ligand stimulation *in vivo* at night, when glucocorticoids are less effective at inducing the expression of *Pck1*. Together, these observations lead to the conclusion that CRY interacts with GR directly on the promoter of *Pck1*, inhibiting the GR and GRE binding interaction. The effect of CRY was incorporated into Equation (54) in a Hill-type function.

$$\frac{dPGC1\alpha_{mRNA}}{dt} = k_{g1} \cdot (1 + FOXO1) \ - k_{g2} \cdot PGC1a_{mRNA}$$

(49)

$$\frac{dPGC1\alpha}{dt} = k_{g3b} \cdot PGC1\alpha_{mRNA} - k_{g3d} \cdot PGC1\alpha - k_{g3t} \cdot PGC1\alpha + k_{g4t} \cdot PGC1\alpha(N)$$

(50)

$$\frac{dPGC1\alpha(N)}{dt} = k_{g3t} \cdot PGC1\alpha - k_{g4t}PGC1\alpha(N) + k_{g8d} \cdot PGC1\alpha(N)_{active} - k_{g5} \cdot PGC\alpha(N)_{active} \cdot SIRT1$$

(51)

$$\frac{dPGC1\alpha(N)_{active}}{dt} = k_{g5} \cdot PGC1\alpha(N) \cdot (1 + SIRT1) - k_{g8} \cdot PGC1\alpha(N)_{active} - k_{g8d} \cdot PGC1\alpha(N)_{active}$$

(52)

$$\frac{dFOXO1}{dt} = k_{g9} \cdot \mathrm{PGC1}\alpha(\mathrm{N})_{active} - k_{g10} \cdot FOXO1$$

(53)

$$\frac{dPck1/G6pc_{mRNA}}{dt} = \mathrm{k_{g11}} \cdot FOXO1 \cdot FGR(N)\left(\frac{1}{1 + (\frac{nucPER/CRY}{k_{g7}})\text{^}s}\right) - k_{g12} \cdot Pck1/G6pc_{mRNA}$$

(54)

3.5 Uncertainty and sensitivity analyses

In a model building process, uncertainty and sensitivity analyses play a very important role in quantifying the output variability and describing the relative importance of each input in determining the output variability [113]. Recognizing that our model

involves a complex network of transcription, translation, and cellular reactions, we analyzed our model using a series of uncertainty and sensitivity analysis methods: 1) local sensitivity analysis, 2) Morris method, and 3) RS-HDMR. Each of the three methods has its own strength and weakness and offered different insights into our model. Local sensitivity analysis is a one-at-a-time (OAT) method that assess how uncertainty in one factor influences the model output while keeping other factors fixed. Although this method is quick and straightforward, it fails to capture any interactions among the parameters. Morris method is an OAT method and is still computationally efficient, but it explores the input design space in such a way that the existence of interaction effects can be identified. However, this method does not identify which specific parameter pair interact with each other. Finally, HDMR provides the interaction effects of specific pair of factors while also giving information about the primary effects. For all three methods, analysis was performed under light and feeding synchronized (both signals on 6am-6pm at 1) condition for consistency. The amplitude of *Pck1/G6pc* mRNA was measured as the response to gain insight into the influence of various parameters on the dynamics of hepatic gluconeogenesis.

3.5.1 Local Sensitivity Analysis

The local sensitivity analysis was performed on all 130 parameters of the model. The relative sensitivity coefficient for every parameter was calculated using the following equation [105]:

$$Sensitivity\ coefficient = \frac{p_k}{y}\left(\frac{\partial y}{\partial p_k}\right)$$

(55)

In Equation (55),

p_k = tested parameter

y = measured response

Each parameter was varied by 1% in the positive direction, and the relative local sensitivity coefficients for each parameter based on the amplitude of *Pck1/G6pc* mRNA were computed.

3.5.2 Morris Method

The Morris method is a computationally effective screening method that identifies a few important parameters in models involving many parameters. The method first computes elementary effects, or the changes in an output due solely to changes in a particular input [114]. In the input space, r trajectories are constructed by first generating a random starting point, then moving one factor at a time in a random order [115]. Once the elementary effects are calculated, they are averaged to assess the overall importance of the input [115]. The elementary effects were calculated for k=112 peripheral parameters using the Morris method. The Morris method calculates the elementary effects for each factor using the following equation [113]:

$$\mathrm{EE_i} = \frac{Y(x_1, \ldots, x_{i-1}, x_i + \Delta_i, x_{i+1}, x_k) - Y(x_1, \ldots, x_k)}{\Delta_\mathrm{i}}$$

(56)

In the above equation, Y is a deterministic function of k input factors (parameters). Because each input parameter x_i is scaled in the interval [0, 1], the right side of the equation is divided by Δ_i, which is a value in {1/(p - 1),…,1 - 1/(p – 1)}. Here, p is the number of levels. The mean (Equation (57)) and variance (Equation (58)) of the elementary effects are considered together to determine the ranking of factors in the order of importance.

$$\mu_\mathrm{i} = \frac{1}{r}\sum_{j=1}^{r} EE_i^j$$

(57)

$$\sigma_\mathrm{i}^2 = \frac{1}{r-1}\sum_{j=1}^{r}\left(EE_i^j - \mu\right)^2$$

(58)

Since radial sampling strategy has proved effective for efficiently covering the input space, Sobol's quasi-random numbers [116,117] were used to generate radial sampling points between ±20% of the nominal values, adopting from the implementation methods presented in [113]. The repetition r = 100 was used for analyzing our model. To create the samples, Sobol's quasi-random sequence was generated to populate a matrix of size (r+1, 2k). Then, the first row of this matrix was removed. The resulting matrix was divided into

matrix **A** (left half), and matrix **B** (right half), each with a dimension of r x k. Each row in matrix **A** is used as a "base point" for the method, defining the set of inputs for the second term of the numerator in Equation (56). Each row in matrix **B** is used as an "auxiliary point" to constitute the radial design. From matrix **A** and **B**, matrix $\mathbf{A_B^{(i)}}$ is created to achieve the radial design such that for each factor i, i^{th} element of i^{th} row of matrix **A** is replaced with the counterpart of matrix **B**, as shown in Figure 9. Then each row in matrix $\mathbf{A_B^{(i)}}$ is the set of input for the first term in the numerator of equation (56). This design yields a computational cost of r(k+1).

$$\mathbf{A} = \begin{bmatrix} a_{11} & a_{12} & \cdots & a_{1k} \\ a_{21} & \ddots & & \vdots \\ \vdots & & \ddots & \vdots \\ a_{r1} & a_{r2} & \cdots & a_{rk} \end{bmatrix} \mathbf{B} = \begin{bmatrix} b_{11} & b_{12} & \cdots & b_{1k} \\ b_{21} & \ddots & & \vdots \\ \vdots & & \ddots & \vdots \\ b_{r1} & b_{r2} & \cdots & b_{rk} \end{bmatrix} \mathbf{A_B^{(i)}} = \begin{bmatrix} a_{11} & b_{1i} & \cdots & a_{1k} \\ a_{21} & \ddots & & \vdots \\ \vdots & & \ddots & \vdots \\ a_{r1} & b_{ri} & \cdots & a_{rk} \end{bmatrix}$$

Figure 9: Radial design of input factors for Morris method. For each parameter, the ith element of ith row of matrix A is replaced with the counterpart of matrix B to constitute the matrix AB(i).

Using this method, the mean and variance of the elementary effects for the peripheral parameters were considered together to sort the factors in the order of importance. This resulted in 20 factors exhibiting the mean of elementary effects greater than 1.5. These factors were further analyzed using RS-HDMR for both primary and interaction effects of input variables in output variance.

3.5.3 RS-HDMR Uncertainty Analysis

HDMR is a variance-based method developed by Rabitz and coworkers [118] aimed to reduce the computational cost for representing input-output relationships in high-dimensional systems. We followed the RSHDMR uncertainty analysis method presented

in [119] to analyze the 20 selected parameters from sensitivity analysis using the Morris Method. The basis for uncertainty analysis using RS-HDMR method is that output f(**x**) can be expressed as a combination of the input x using statistical ANOVA decomposition, as Equation (59) shows.

$$f(\mathbf{x}) = f_0 + \sum_{i=1}^{n} f_i(x_i) + \sum_{1\le i<j\le n} f_{ij}(x_i, x_j) + \cdots + \sum_{1\le i_1<\cdots<i_l\le n} f_{i_1 i_2 \ldots i_l}(x_{i1}, x_{i2}, \ldots\ x_{i_l}) + \cdots + f_{1\ldots n}(x_1, x_2, \ldots, x_n) \quad (59)$$

In Equation (59), f_0 is a constant representing the mean response to f(**x**). First order component function $f_i(x_i)$ gives the independent contributions to f(x) by the i^{th} input variable acting alone. Second order component function $f_{ij}(x_i,x_j)$ gives the pair correlated contribution to f(x) by the input variables x_i and x_j. The last term contains any residual n^{th} order correlated contribution of all input variables. For most real-world applications, HDMR expansion to the second order is sufficient, and Equation (59) reduces to Equation (60).

$$f(\mathbf{x}) \approx f_0 + \sum_{i=1}^{n} f_i(x_i) + \sum_{1\le i<j\le n} f_{ij}(x_i, x_j) \quad (60)$$

The variables x_i were sampled between ±20% of the nominal values using Sobol's quasi-random sequence, and then were rescaled such that $0 \le x_i \le 1$ for all I by performing transformation of the input variables. Then, the output function f(**x**) is defined in the unit hypercube $K^n = \{(x_1,x_2,\ldots,x_n)|0 \le x_i \le 1, i=1,2,\ldots,n\}$, and the component functions of RS-HDMR possess the following forms:

$$f_0 = \int_{K^n} f(\boldsymbol{x}) d\boldsymbol{x}$$

(61)

$$f_i(x_i) = \int_{K^{n-1}} f(x_i, \boldsymbol{x}^i) d\boldsymbol{x}^i - f_0$$

(62)

$$f_{ij}(x_i, x_j) = \int_{K^{n-2}} f(x_i, x_j, \boldsymbol{x}^{ij}) d\boldsymbol{x}^{ij} - f_i(x_i) - f_j(x_j) - f_0 \ldots$$

(63)

Here, $d\mathbf{x}_i$ and $d\mathbf{x}_{ij}$ are the product of $dx_1 dx_2 \ldots dx_n$ without dx_i and $dx_i dx_j$, respectively. The first order component f_0 is simply the mean value of $f(\mathbf{x})$ over the whole domain. The individual component functions presented in Equations (61)-(63) have a direct statistical correlation interpretation which leads to the decomposition of model output variance $\sigma_{\bar{f}}^2$ into its individual input variable contributions. Because of the orthogonality of the component functions, the variance can be expressed as Equation (64).

$$\sigma_{\bar{f}}^2 = \sum_{i=1}^{n} \sigma_i^2 + \sum_{1 \le i < j \le n}^{n} \sigma_{ij}^2 + \cdots$$

(64)

To reduce the sampling effort, the component functions are usually approximated by basis functions of three types: orthonormal polynomials, cubic spline, and polynomials. Among these basis functions, orthonormal polynomials provide the most saving in computational cost [120]. Therefore we employed a set of orthonormal

polynomials in Equations (65)-(67) as a basis to approximate the component functions in Equations (68) and (69) [119].

$$\phi_1(x) = \sqrt{3}(2x - 1) \quad (65)$$

$$\phi_2(x) = 6\sqrt{5}\left(x^2 - x + \frac{1}{6}\right) \quad (66)$$

$$\phi_2(x) = 20\sqrt{7}\left(x^3 - \frac{3}{2}x^2 + \frac{3}{5}x - \frac{1}{20}\right) \quad (67)$$

$$\mathrm{f_i}(x_i) = \sum_{k=1}^{\infty} \alpha_k^i \phi_k(x_i) \quad (68)$$

$$\mathrm{f_{ij}}(x_i, x_j) = \sum_{k,l=1}^{\infty} \beta_{kl}^{ij} \phi_k(x_i)\phi_l(x_j) \quad (69)$$

The coefficients for the component functions in Equations (68) and (69) were estimated using Equations (70) and (71). Finally, these coefficients were used to calculate the first order (primary effect) and second order variance (interaction effect) using the Equations (72) and (73).

$$\begin{pmatrix} \alpha_1^i \\ \alpha_2^i \\ \alpha_3^i \end{pmatrix} \approx \frac{1}{\mathrm{n}} \sum_{s=1}^{N} \begin{pmatrix} f\left(\boldsymbol{x}^{(s)}\right)\phi_1(x_i^{(s)}) \\ f\left(\boldsymbol{x}^{(s)}\right)\phi_2(x_i^{(s)}) \\ f\left(\boldsymbol{x}^{(s)}\right)\phi_3(x_i^{(s)}) \end{pmatrix} \quad (70)$$

$$\begin{pmatrix} \beta_{11}^{ij} \\ \beta_{12}^{ij} \\ \vdots \\ \beta_{32}^{ij} \\ \beta_{33}^{ij} \end{pmatrix} \approx \frac{1}{\mathrm{n}} \sum_{s=1}^{N} \begin{pmatrix} f(\boldsymbol{x}^{(s)}) \phi_1\left(x_i^{(s)}\right) \phi_1\left(x_j^{(s)}\right) \\ f(\boldsymbol{x}^{(s)}) \phi_1\left(x_i^{(s)}\right) \phi_2\left(x_j^{(s)}\right) \\ \vdots \\ f(\boldsymbol{x}^{(s)}) \phi_3\left(x_i^{(s)}\right) \phi_2\left(x_j^{(s)}\right) \\ f(\boldsymbol{x}^{(s)}) \phi_3\left(x_i^{(s)}\right) \phi_3\left(x_j^{(s)}\right) \end{pmatrix}$$

(71)

$$\sigma_i^2 = \sum_{k=1}^{s_i} \left(\alpha_k^i\right)^2$$

(72)

$$\sigma_{ij}^2 = \sum_{k=1}^{s_i\prime} \sum_{l=1}^{s_j} \left(\beta_{kl}^{ij}\right)^2$$

(73)

3.6 Results

Our *in silico* studies aim to explore the effects of circadian disruption and metabolic re-entrainment on the rhythms of hepatic gluconeogenesis. The expression of gluconeogenic genes (*Pck1/G6pc* in our model) is under the modulation of two independent *zeitgebers*, light/dark cycle and feeding/fasting cycle. The simplified schematic of the model encompassing the HPA-axis and the periphery representing human hepatocyte is shown in Figure 10. The schematic depicts the signal transduction from the environment (light and feeding) to the transcription of *Pck1/G6pc*. Cortisol level in the periphery is mediated by the light and the feeding signals, and induces the transcription of *Pck1/G6pc* when bound to its receptor. Induction by cortisol is inhibited by the PER/CRY, one of the key components of the circadian clock machinery. The

changing concentration of NAD^+ following the feeding/fasting cycle regulates FOXO1 through SIRT1 and PGC-1α.

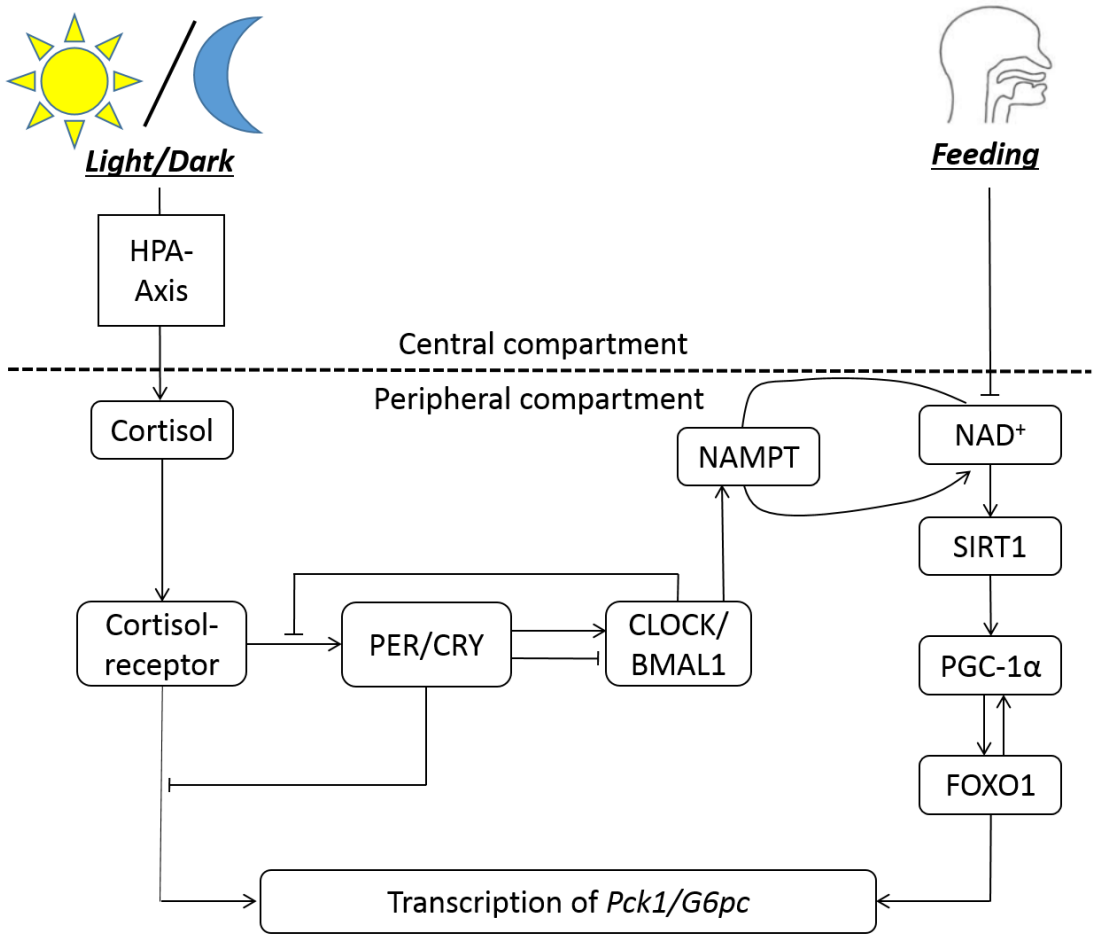

Figure 10: Simplified schematic of the model

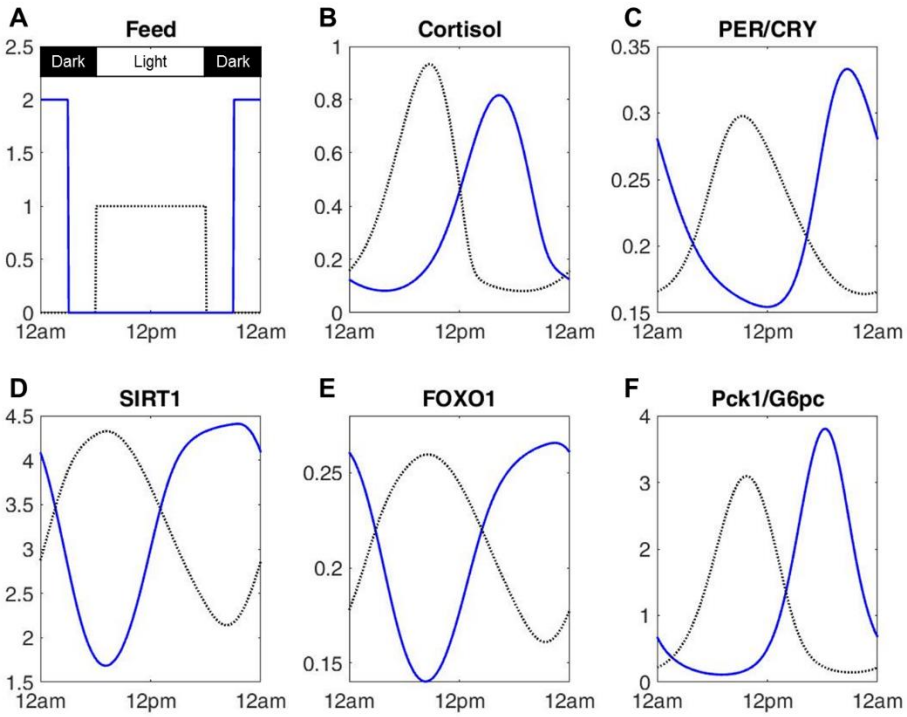

Figure 11: The time profiles of key components throughout the day upon synchronized (dotted line) and time-restricted (solid line) feeding schedules. Light signal was at 1 from 6am to 6pm, and at 0 for the rest of the day. Feeding signals for both conditions are shown in (A). The corresponding cortisol (B), PER/CRY protein (C), SIRT1 (D), FOXO1 (E), and Pck1/G6pc mRNA (F) are shown.

In Figure 11, The behavior of the model throughout the 24-h day upon synchronized (light and feeding schedules are identical) and time-restricted feeding (TRF) schedules are shown. Light signal was at 1 from 6am to 6pm, and at 0 for the rest of the day. Feeding signals for both conditions are shown in Figure 11A. For the light-feeding synchronized condition, feeding signal was at 1 from 6 am to 6 pm, and at 0 for the other 12 hours. To make sure that the system is provided with identical amount of feeding signal, which represents the amount of food available to the system at a given time, the area under the curve (AUC) for feeding were identical between the light-feeding synchronized condition and TRF condition. As such, feeding signal was at 2 from 9 pm

to 3 am and at 0 for the rest of the time for TRF condition. The cortisol (11B) and PER/CRY protein (11C), both regulators of *Pck1/G6pc* transcription, peak in the morning time for the synchronized schedule and evening time for the TRF schedule. For both cases, cortisol and PER/CRY peak in the early active phase, consistent with restricted feeding studies on mice which show ~12h phase shift in cortisol and clock gene levels in the anticipation of meal time [86,87,121]. NAD^+(11D) peaks 4-5 hours after the beginning of feeding time, agreeing with previous experimental work [122]. The circadian rhythm of FOXO1 (11E) closely follows that of SIRT1. Although no experimental data confirms this, the results are expected within the structure of our model because FOXO1 is activated by SIRT1-activated PGC-1α. The expression of *Pck1/G6pc* mRNA (11F) also peak in the early active phase according to our model. In *ad libitum* fed rats, both G6Pase and PEPCK activity peak slightly before the dark (active) phase in rats subjected to 12:12 h light/dark cycle [102,123]. When rats are moved to TRF schedule, G6Pase activity peaks slightly before the feeding start time. G6Pase protein amount still oscillates rhythmically but becomes bimodal, with the major peak slightly before the feeding time and a minor peak in the middle of the dark phase [102]. For PEPCK, the enzymatic activity becomes bimodal with the major peak at the transition from dark to light phase and a minor peak in the middle of the dark phase. The PEPCK protein amount peaks ~2 hours after the feeding start time [102]. Although the phase changes that occur for the PEPCK and G6Pase enzymatic activities and protein amounts slightly differ in details, the common theme for all of them is that the gluconeogenic gene expression is the highest around the transition time from inactive to active phase, consistent with our model. In terms of amplitude

change upon adjustment to feeding schedule, our model was constructed to most closely follow the experimental finding that amplitude of PEPCK protein amount increases when rats are switched from *ad libitum* feeding to TRF [102].

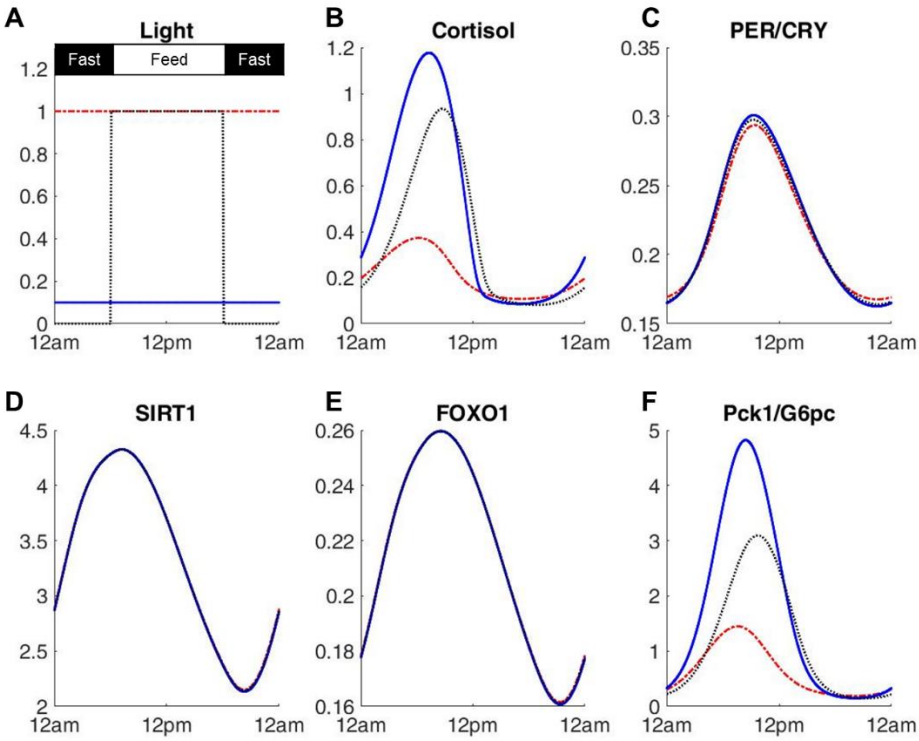

Figure 12: Time profiles of key components under constant light schedule at different intensities are compared. Feeding signals was at 1 from 6am to 6pm, and at 0 for the rest of the day (A). Constant bright light (dotted-dashed line) and constant dim light (solid line) are shown in (A), along with a control (dotted line), in which feeding and light are synchronized. The cortisol (B), PER/CRY protein (C), SIRT1 (D), FOXO1 (E), and Pck1/G6pc mRNA (F) under the different light intensities are also presented.

Figure 12 shows the modifications to gluconeogenic gene expression when the model experiences different type of light signals. In this figure, the response of the model to constant dim light and constant bright light is compared to 12:12 h light/dark cycle, while the feeding schedule is fixed to 12:12 h feeding/fasting cycle for all three conditions (12A). Imposing constant bright light results in reduced amplitude of cortisol

(12B) and *Pck1/G6pc* (12F), while constant bright light increases the amplitude. An animal study conducted in voles confirm the model prediction [123]. In this experiment, female voles were placed in constant light environment while male voles were placed in constant dark environment. When G6Pase activity was measured over a 24h period, animals in constant dark environment showed statistically significant oscillation while the animals in constant light environment did not. Although gender difference may have contributed to the enzyme behavior, the results are aligned with our model prediction. The PER/CRY (12C) oscillation amplitude is slightly decreased when constant bright light is imposed, qualitatively in agreement with experimental observations in mice [88]. SIRT1 (12D) and FOXO1 (12E) dynamics are not influenced by the light schedule change.

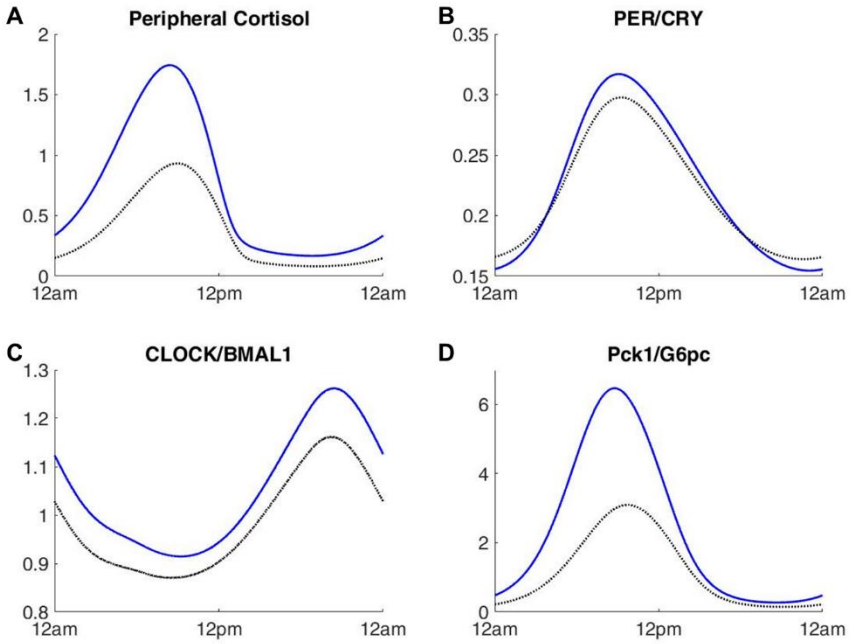

Figure 13: Time profiles of peripheral cortisol (A), PER/CRY protein (B), CLOCK/BMAL1 complex (C) and Pck1/G6pc mRNA (D) are shown under nominal condition (dotted black lines) and high peripheral cortisol (solid blue lines). The light and feeding schedule are synchronized.

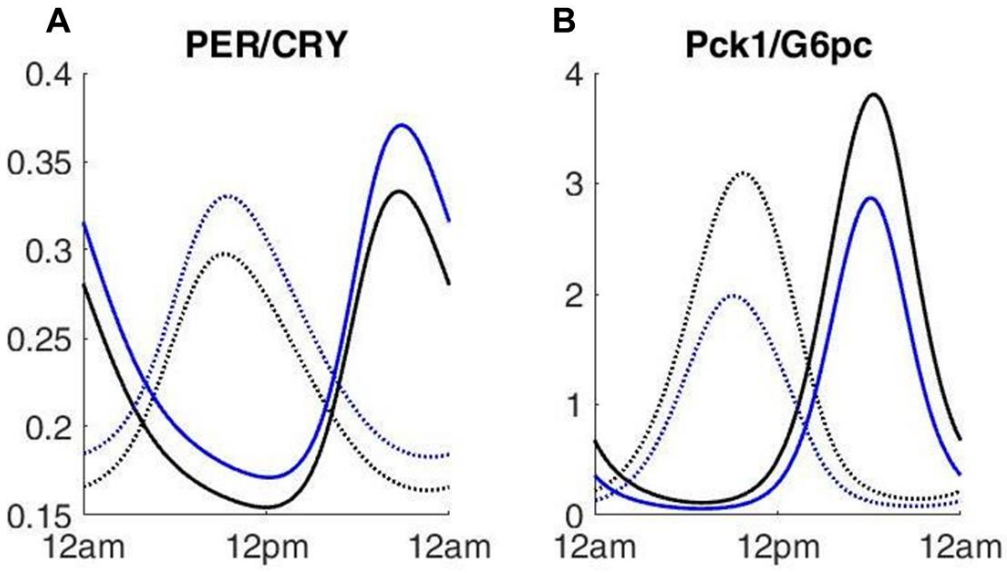

Figure 14: Time profiles of PER/CRY protein (A), and Pck1/G6pc mRNA (B) are shown under nominal condition (black lines) and CRY over-expression condition (blue lines). Dotted lines represent light-feeding synchronized condition, and solid lines represent time-restricted feeding condition.

Next, we examined the effect of cortisol shock and CRY overexpression against experimental findings. Sharp increase in serum cortisol level increases glucose production due to gluconeogenesis in humans [24]. When peripheral cortisol level is elevated in our model while the central compartment is conserved, PER/CRY, CLOCK/BMAL1, and *Pck1/G6pc* levels are all increased (Figure 13). The peripheral cortisol level was increased by doubling the secretion from the central compartment. Since our model does not consider PER and CRY separately, CRY overexpression was simulated by doubling the transcription rate of *Per/Cry* mRNA (V_{1b}). The resulting profiles under *ad libitum* feeding and TRF are shown in Figure 14. Under both feeding schedules, modulating the transcription rate did result in increased expression of PER/CRY protein, and resulted in decreased expression of *Pck1/G6pc*. The results are consistent with recent findings that CRY1 and CRY 2 inhibit gluconeogenesis by cortisol-receptor complex in the nucleus from binding to the GRE region of the gluconeogenic genes [27].

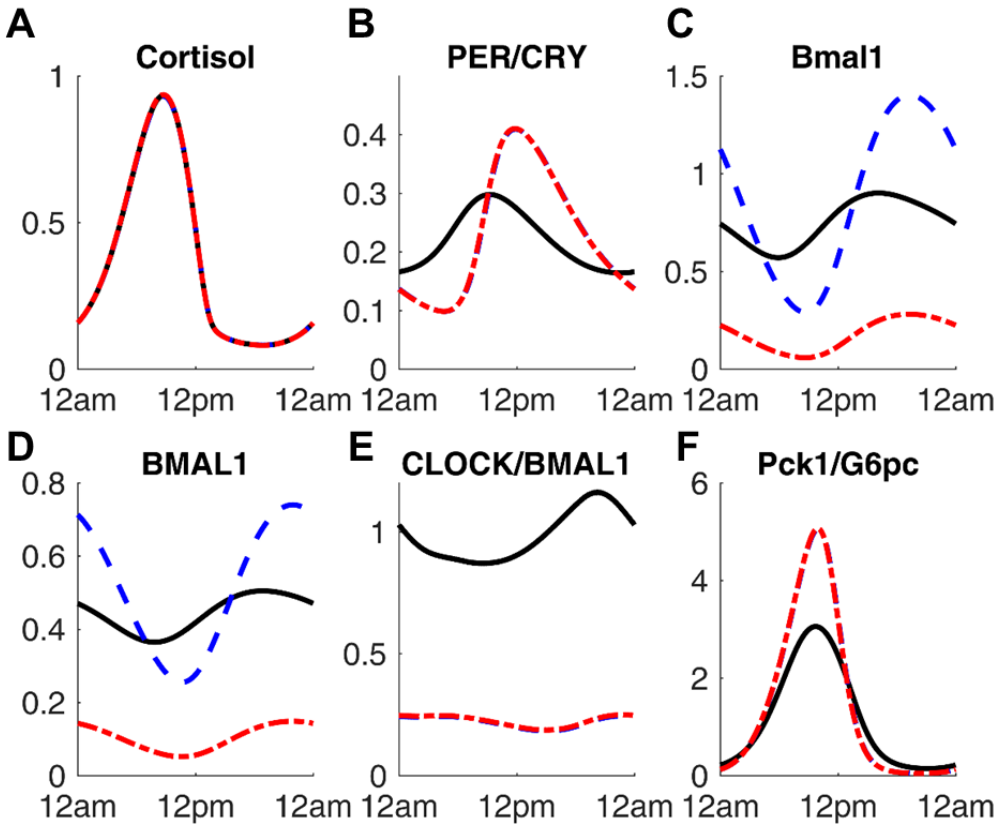

Figure 15: Time profiles of cortisol (A), PER/CRY protein (B), Bmal1 mRNA (C), BMAL1 protein (D), CLOCK/BMAL1 complex (E) and Pck1/G6pc mRNA (F) are shown under nominal condition (black lines), Clock knockout condition (blue lines), and Bmal1 knockout condition (red lines).

To simulate genetic circadian disruption, we tested the model under very low CLOCK and BMAL1 expression and showed the results in Figure 15. *Clock* and *Bmal1* knockouts were simulated by 80% reduction in expression level. As Figure 15C shows, the concentration of CLOCK/BMAL1 heterocomplex is lower in both knockout conditions compared to the nominal condition. Circadian cortisol profile (15A) is unaffected by the knockout in our model. BMAL1 protein and *Bmal1* mRNA levels are suppressed for the BMAL1 knockout model, but the same components are expressed with increased amplitude for CLOCK knockout model. PER/CRY protein (15B) oscillation

amplitude becomes greater under the knockout conditions, and *Pck1/G6pc* (15D) also oscillate with a higher amplitude. Experimental studies on whole-body CLOCK knockouts give conflicting results depending on the experimental/environmental conditions as well as the genetic background of the animals [23]. Some studies show that knockout of CLOCK results in decreased or normal blood glucose level [124,125] while others report increased blood glucose level [126,127] and impaired glucose tolerance. Our model supports the latter case where fasting glucose level is elevated upon CLOCK knockout due to higher amplitude of gluconeogenesis.

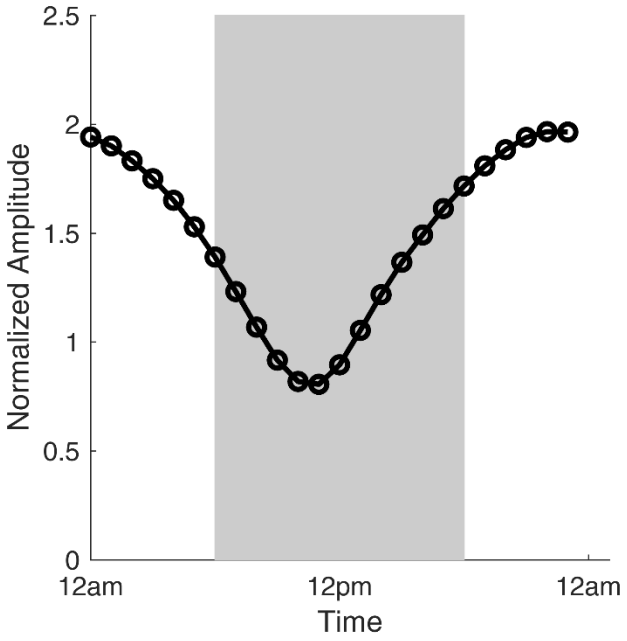

Figure 16: Amplitude of Pck1/G6pc for Clock KO model normalize by the wile type amplitude under light-feeding synchronized schedule. Normalized amplitudes are plotted against the feeding start time. For all cases, feeding lasted for 12 hours, and light schedule was fixed to be on from 6am to 6pm.

Next, we investigated whether the increased amplitude of *Pck1/G6pc* in *Clock* KO condition can be adjusted back to the nominal amplitude by changing the feeding rhythm relative to the light/dark cycle. To examine the effect of phase relations between light and

feeding, we simulated 12h feeding period starting at different times of the day while fixing the light period from 6 am to 6 pm. In Figure 16, the amplitude of *Pck1/G6pc* for different feeding schedule normalized by the wild type amplitude under synchronized condition are plotted. The x-axis represents the start time of the feeding period. The figure shows that amplitude of *Pck1/G6pc* under *Clock* KO condition changes with the feeding start time. Amplitudes are greater when feeding is started in the dark phase. If feeding starts in the afternoon (3pm-6pm), the amplitude for KO model reaches below the wild type amplitude under synchronized condition. Next, we present the analysis of the model using the uncertainty and sensitivity analyses on the amplitude of *Pck1/G6pc*.

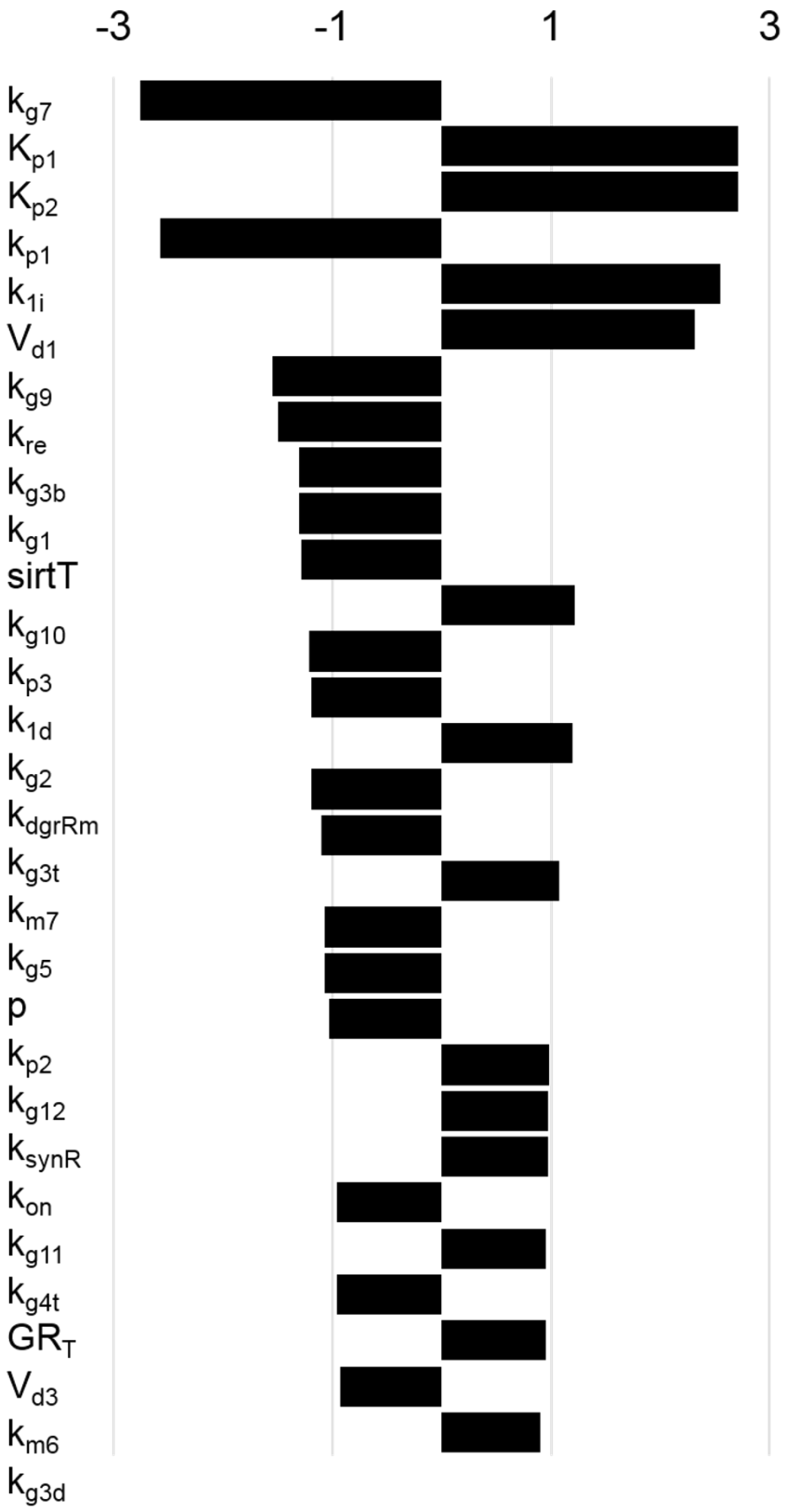
-3
-1
1
3
k_{g7}
K_{p1}
K_{p2}
k_{p1}
k_{1i}
V_{d1}
k_{g9}
k_{re}
k_{g3b}
k_{g1}
sirtT
k_{g10}
k_{p3}
k_{1d}
k_{g2}
k_{dgrRm}
k_{g3t}
k_{m7}
k_{g5}
p
k_{p2}
k_{g12}
k_{synR}
k_{on}
k_{g11}
k_{g4t}
GR_T
V_{d3}
k_{m6}
k_{g3d}

Figure 17: Sensitivity coefficients for 30 most sensitive parameters using local sensitivity analysis

In Figure 17, the sensitivity coefficients computed from local sensitivity analysis using Equation (56) are shown for the 30 most sensitive parameters. The sensitivity coefficients for all parameters are available the repository. Among the parameters with high sensitivity coefficients, K_{p1}, K_{p2}, k_{p1}, V_{d1}, and V_{d3} mediate the dynamics of the HPA-axis. A group of parameters that control the dynamics of PGC-1α and FOXO1, such as k_{g7}, k_{g9}, k_{g1}, k_{g10}, k_{g2}, k_{g3t}, k_{g4t}, and k_{g3d} also had high sensitivity coefficients. Other than these two groups, parameters associated with *Per/Cry* transcription (k_{1i} and p) cortisol-receptor dynamics (k_{re}, k_{dgrRm}, and k_{synR}) also exhibited high sensitivity coefficients.

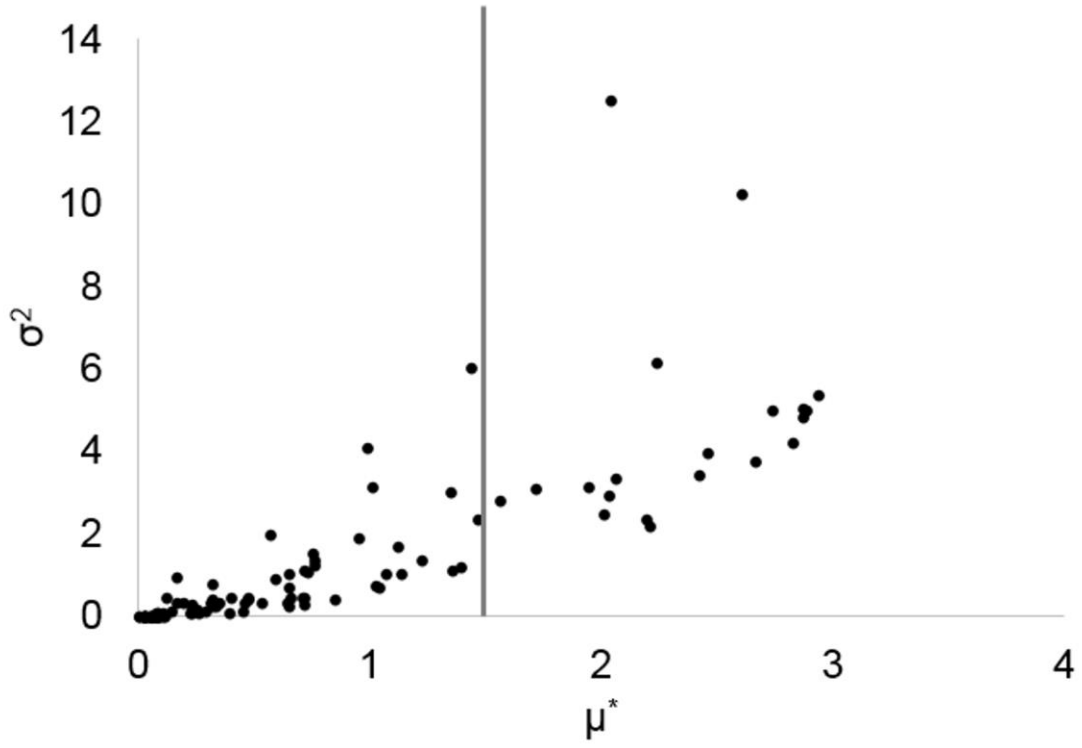

Figure 18: Sample results from sensitivity analysis using Morris method performed on the amplitude of Pck1/G6pc mRNA amplitude. 100 repetitions of sampling was used to generate this figure. The variance (σ^2) is plotted against μ^*.

In Figure 18, the results from sensitivity analysis using Morris method performed on peripheral parameters is visualized on a variance (σ^2) versus absolute mean (μ^*) plot. Morris method was used as a screening method for identifying the most important parameters, because this method will compute both elementary and interaction effects without high computational cost. In general, the parameters that has greater mean elementary effects also had greater variance. We selected 20 samples that had μ^* values greater than 1.5 as important parameters, and listed them in Table 1 along with the μ^* values. Examining the table, the parameters pertaining to the dynamics of PGC-1α, FOXO1, *Per/Cry* transcription, *Bmal1* transcription, and cortisol receptor had the greatest elementary effects.

Table 1: Absolute value of mean of elementary effects for 20 most sensitive parameters identified using Morris Methods on amplitude of *Pck1/G6pc*.

Rank	Parameter	μ^*	σ^2	Rank	Parameter	μ^*	σ^2
1	k_{g10}	2.9330	5.4027	11	k_{g8}	2.2431	6.1479
2	k_{g9}	2.8870	4.9604	12	k_{g11}	2.2097	2.1702
3	k_{g1}	2.8673	4.8427	13	k_{g12}	2.1902	2.3458
4	k_{g2}	2.8631	5.0442	14	$sirt_T$	2.0553	3.3711
5	k_{g3b}	2.8250	4.2164	15	k_{4b}	2.0430	12.5589
6	k_{g3d}	2.7314	4.9744	16	GRT	2.0307	2.9139
7	k_{g3t}	2.6627	3.7803	17	$k_{on,GR}$	2.0089	2.4504
8	k_{1i}	2.6072	10.242	18	$k_{re,GR}$	1.9427	3.1098
9	k_{g4t}	2.4582	3.9920	19	k_{g7}	1.7077	3.1010
10	k_{g5}	2.4166	3.4337	20	k_{m1}	1.5650	2.8073

The parameters in Table 1 were further analyzed with RS-HDMR uncertainty analysis, which is a variance based method that is capable of identifying pair-wise interaction effects in addition to the main effects. Since our model is expected to be highly nonlinear, we first tried to identify the appropriate sample size for analyzing our

model. Table 2 reports the main results from RS-HDMR uncertainty analysis for different sample sizes: output (mean amplitude of *Pck1/G6pc*); the total variance in output (σ^2); the sum of all first order variances ($\Sigma\sigma^2_i$); and the sum of all second order variances ($\Sigma\sigma^2_{ij}$) from the RS-HDMR uncertainty analysis. For Equation (64) to hold true, the condition $\sigma^2 \geq \sum\sigma_i^2 + \sum\sigma_{ij}^2$ has to be met. Therefore, only the sample size of 20,000 and 100,000 yield valid uncertainty analysis. Since greater sample size should provide the most accurate results, only the analysis resulting from the sample size of 100,000 is presented in Table 3 and Figure 19. In Table 3, the first order variance for the 20 tested parameters are presented in the order of importance. Parameters related to the dynamics of PGC-1α and FOXO1 are the most important parameters in determining the variance in amplitude of *Pck1/G6pc* according to the RS-HDMR method. In Figure 19, the second order interaction effects to output variance are shown in a color scheme, with bigger interaction effects in darker color and smaller interaction effects lighter color. The pair k_{1i} and k_{4b} show the largest second order interaction, while the parameters pertaining to the PGC-1α and FOXO1 level show the next largest second order interaction.

Table 2: Summary of results from HDMR uncertainty analysis on amplitude of *Pck1/G6pc*.

Sample Size	f_0	σ^2	$\Sigma\sigma^2_i$	$\Sigma\sigma^2_{ij}$
1000	5.8266	15.9072	11.4909	34.9030
2000	5.8149	14.5537	10.8716	15.0472
3000	5.7970	13.8447	10.4087	10.4486
5000	5.8049	14.1645	10.5303	7.3712
10000	5.7963	13.2363	10.1985	3.9241
20000	5.7881	12.6472	9.9297	2.5715

100000	5.7884	12.6021	9.9391	2.0946

Table 3: First order variance from HDMR uncertainty analysis. Correction factor to get nominal *Pck1/G6pc* amplitude for CLOCK knockout model is also presented.

Parameter	σ^2_i (from HDMR)	Correction factor	Influence on PGC-1α(N)
k_{g2}	**0.836349**	**1.58**	**decrease**
k_{g10}	**0.833797**	**1.57**	**decrease**
k_{g9}	**0.793650**	**0.64**	**increase**
k_{g1}	**0.792885**	**0.63**	**increase**
k_{g3b}	**0.790013**	**0.63**	**increase**
k_{g3d}	**0.720930**	**1.62**	**decrease**
k_{g3t}	**0.686181**	**0.62**	**increase**
k_{g4t}	**0.575706**	**1.69**	**decrease**
k_{g5}	**0.556384**	**0.59**	**increase**
k_{g12}	0.450824	1.73	
k_{g11}	0.449879	0.58	
k_{g8}	**0.409953**	**1.82**	**decrease**
$sirt_T$	0.398856	0.59	
GR_T	0.359445	0.64	
$k_{on,GR}$	0.347152	0.64	
$k_{re,GR}$	0.317100	1.60	
k_{g7}	0.233719	1.71	
k_{1i}	0.191373	1.18	
k_{m1}	0.166523	1.65	
k_{4b}	0.028383	0.45	

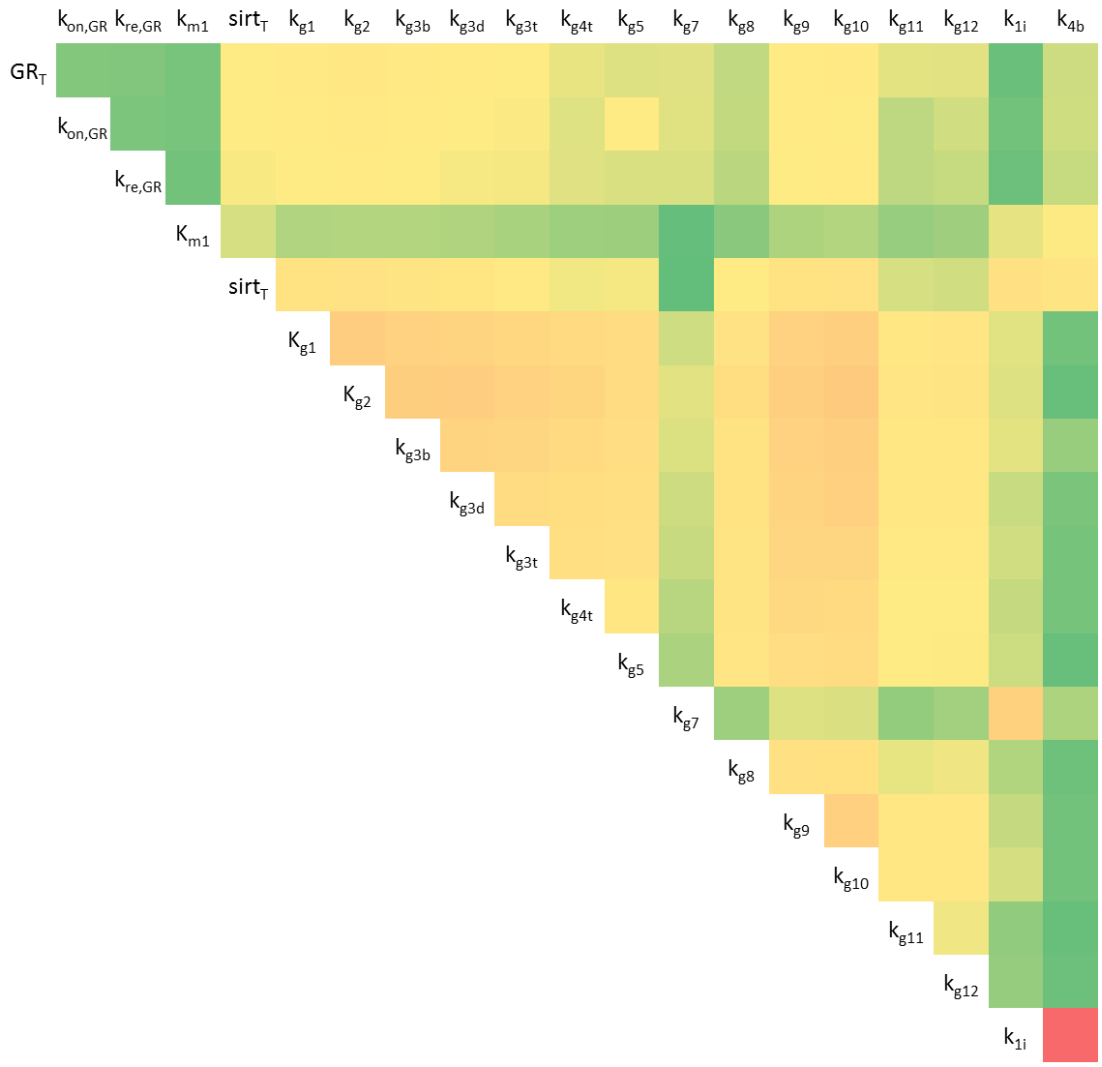

Figure 19: Second order interaction contributions to output variance from RS-HDMR uncertainty analysis. Darker color indicates higher interaction effect.

Finally, we attempted changing the amplitude of *Pck1/G6pc* of the *Clock* KO model by applying a correction factor to different parameters. The correction factor that most closely adjusts the *Pck1/G6pc* amplitude back to the nominal amplitude for each parameter was calculated. These factors are listed in Table 3. The parameters that either contribute to increasing or decreasing level of nuclear PGC-1α are indicated. The correction factors for these parameters show that parameters with larger first order

variance require a correction factor with a smaller percentage change of the original value of the parameter. Time profiles for the *Clock* KO model with select correction factors are shown in Figure 20. Adjusting k_{g1} (PGC-1α transcription rate) reduced the amplitude of the *Clock* KO model by decreasing the nuclear PGC-1α level (20D), which is a direct activator of FOXO1 that stimulates the expression of gluconeogenic genes (20E). Adjusting k_{1i} (inhibition constant for *Per/Cry* transcription) increased the PER/CRY (20B), CLOCK/BMAL1 (20C), and nuclear PGC-1α (20D) level. Finally, adjusting k_{4b} returned the PER/CRY profile (20B) to the wild type condition, increased the CLOCK/BMAL1 (20C) level and nuclear PGC-1α (20D) level.

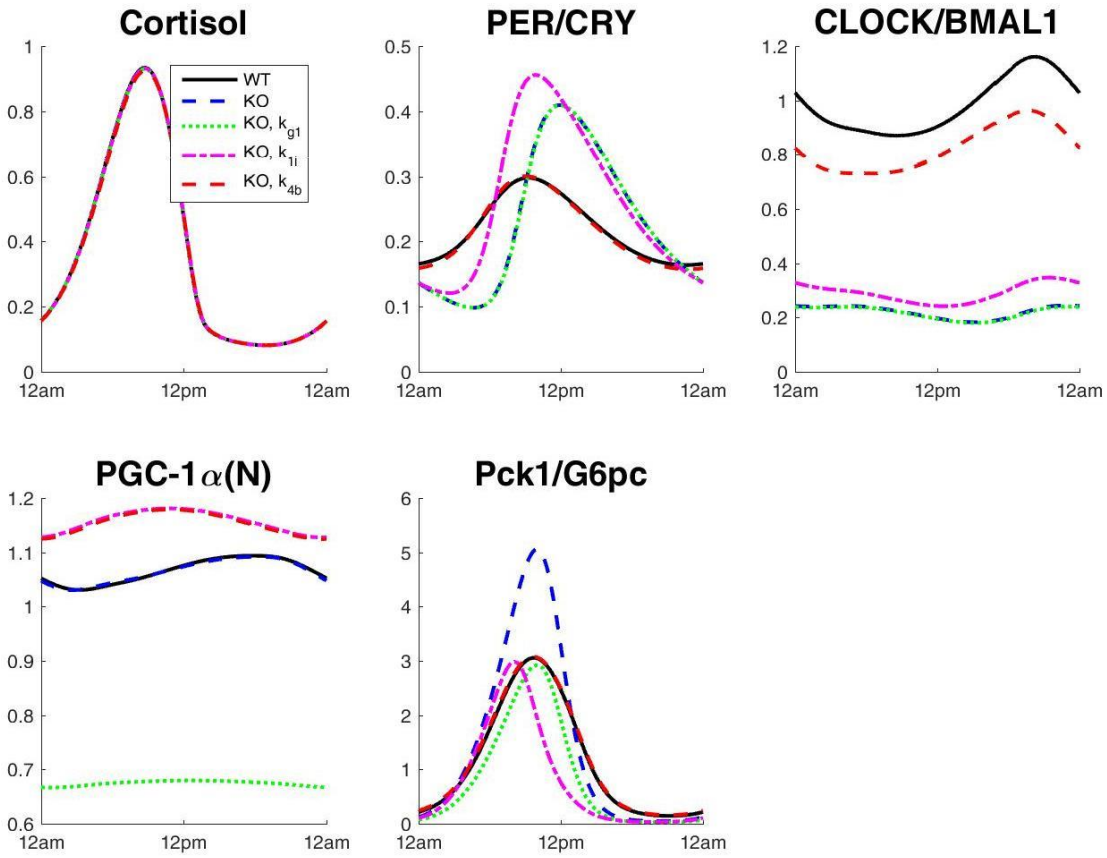

Figure 20: Time profiles of cortisol (A), PER/CRY protein (B), CLOCK/BMAL1 complex (C) , nuclear PGC-1α, and Pck1/G6pc mRNA (E) are shown under nominal condition and Clock KO condition. The rest of the profiles show Clock

KO condition adjusted by correction factor for certain parameters: k_{g1}, k_{1i}, and k_{4b}. The light and feeding schedule are synchronized for all profiles.

3.7 Discussion

The circadian rhythms modulate important metabolic pathways including gluconeogenesis [21,22] and lipid metabolism [90,91]. Because of the intimate relationship between circadian rhythms and metabolism, disruption in the daily rhythms often result in metabolic syndromes such as obesity and high triglycerides [6]. In mammals, it is important that plasma glucose level stays within a physiologically relevant bound since some key biological functions such as neuronal activity and balancing of electrolytes depend on homeostatic plasma glucose level [89]. Various clock gene knockout studies support that plasma glucose homeostasis is under the regulation of circadian components. For example, double knockout of liver-specific *Bmal1* results in altered expression of gluconeogenic genes as well as fasting hypoglycemia [21]. Similarly, hepatic *Cry* overexpression lowers the blood glucose level after 6 hours of fasting [22]. These studies motivate the need to elucidate the mechanisms of how circadian rhythms modulate glucose homeostasis throughout the day. Since glucose homeostasis is maintained through a complex network of regulations and chemical reactions involving multiple organs and numerous hormones, we chose to focus on hepatic gluconeogenesis specifically to simplify the problem while drawing meaningful conclusions.

Figure 11 shows the model behavior when either *ad libitum* feeding or TRF is applied. The model predicts that the fasting level of *Pck1/G6pc* (11F) will be elevated under TRF, compared to that of *ad libitum* feeding. The dynamics of *Pck1/G6pc* is driven

by three different forces in our model: 1) FOXO1 binding to a DNA motif on the promoter region and stimulating the transcription; 2) nuclear cortisol-receptor complex binding to the GRE region on the promoter and stimulating the transcription; and 3) PER/CRY inhibiting the binding of nuclear cortisol-receptor complex from binding to the GRE. Figure 11A shows that cortisol peak at the transition from light to dark period is decreased when feeding schedule is changed from a*d libitum* to TRF, and 11B shows that PER/CRY level is increased around the same transition time. These two results together imply that the *Pck1/G6pc* level should decrease since cortisol stimulates the expression of gluconeogenic genes while PER/CRY inhibits it. However, 11E shows that FOXO1 amplitude and level increases when the model is exposed to TRF condition. These competing effects ultimately result in an increased amplitude and level in the expression of *Pck1/G6pc*, suggesting that the influence of FOXO1 is stronger than the effects of cortisol and PER/CRY. The increased amplitude of FOXO1 can be attributed to the higher amplitude of feeding signal, which transduces down to FOXO1 via SIRT1 (11D) and PGC-1α. The phase of all major components are re-entrained to the feeding rhythm, since cortisol, clock genes, and FOXO1 are all phase shifted. When the increase in amplitude and phase change of PEPCK protein was observed for the TRF condition [102], animals were given a 2 hour window during the rest period for food consumption, which would have resulted in high caloric intake during a short period of time, similarly to the simulation condition.

To validate that the other two driving forces, stimulation by cortisol and inhibition by PER/CRY, produce expected behavior in *Pck1/G6pc* expression, we tested

overexpression of PER/CRY in Figure 14 and elevated peripheral cortisol in Figure 13. Increased level of PER/CRY protein does result in a decreased expression of *Pck1/G6pc*, for both *ad libitum* feeding and TRF, agreeing with animal studies [22,27]. Increase in peripheral cortisol also results in an increased expression of *Pck1/G6pc*. A side effect of increase in peripheral cortisol is the increased level CLOCK/BMAL1 complex, which activates the expression of PER/CRY protein. Stimulation of *Pck1/G6pc* expression by increased cortisol amount outperforms the increased inhibition by PER/CRY protein, resulting in a behavior consistent with experimental findings [24].

While the feeding pattern can completely re-entrain the *Pck1/G6pc* expression, modifications to the light signal also influence hepatic gluconeogenesis. As shown in [123] keeping the animals in constant bright light for an extended time period abolishes the circadian rhythms for G6Pase activity. From this study, we hypothesized that imposing a constant bright light on our model would result in a decreased amplitude for *Pck1/G6pc*. Figure 12F shows that our hypothesis is valid. When the light signal was on at 1 constitutively to simulate constant bright light condition, the amplitude of *Pck1/G6pc* was reduced, mainly due to the decline in the cortisol level and amplitude (12B). The dampening of the rhythm in cortisol for the bright light condition is due to light-mediated degradation of CRH [40-42], which results in decreased secretion of cortisol from the HPA-axis. PER/CRY (12C) amplitude was also decreased by a small percentage, but had negligible effect on the amplitude of *Pck1/G6pc*. Figure 12D and E show that SIRT1, PGC-1α, FOXO1 pathway was unaffected by the modified light.

Next, we challenged the model by simulating a *Clock* KO condition. Figure 15 shows that the amplitude of *Pck1/G6pc* is higher for the *Clock* KO model compared to the wild type model, under both feeding schedules. CLOCK/BMAL1 complex in the nucleus influences the dynamics of PER/CRY protein in two opposing ways as depicted inFigure 10. It binds to the Ebox enhancer on the promoter of *Per* and *Cry* genes and stimulates the expression of PER/CRY. It can also inhibit the expression of PER/CRY by preventing the cortisol-receptor complex in the nucleus from binding to the GRE of the promoter and preventing the expression of PER/CRY. Figure 15 shows that decreased level of CLOCK/BMAL1 (15C) resulted in increased level and amplitude of PER/CRY (15B) due to lost inhibition effect. Then, the increased amplitude of PER/CRY caused the amplitude of *Pck1/G6pc* (15D) to increase. For both PER/CRY and *Pck1/G6pc*, the amplitude difference between wild type and KO is greater for *ad libitum* feeding compared to TRF, probably due to stronger signal from the FOXO1 pathway. CLOCK knockout studies report conflicting results where some result in decreased or normal blood glucose level [124,125] while others report increased blood glucose level[124]; our model supports the latter case. The discrepancy in CLOCK knockout studies point to an importance in genetic background of the animals.[23] However, one should also note that decreased or normal blood glucose level for CLOCK knockout mice were observed under high-fat diet, and disruption in circadian rhythms can lead to a problem in fat absorption.[124] Thus this phenomenon cannot be accurately captured with my model which does not distinguish between different fat contents in feeding.

Since animal experiments [102] and our model support the idea that feeding pattern can re-entrain the expression of gluconeogenic genes, we hypothesized that the increased amplitude of *Pck1/G6pc* under *Clock* KO condition can be returned to the nominal level by adjusting the feeding schedule. Figure 16 shows the amplitude change for *Clock* KO model normalized by the wild type amplitude for different feeding schedules, and conveys that our hypothesis is valid. Figure 16 shows that there exists a feeding schedule which produces an amplitude for *Pck1/G6pc* very similar to the nominal amplitude although CLOCK/BMAL1 complex level is very low. Delaying the feeding phase by 2 or 7 hours resulted in amplitude very similar to the wild type amplitude. Although it should be noted that the decrease in *Pck1/G6pc* amplitude was accompanied by a wide phase shift, such behavior is expected since the phase relationship between feeding/fasting cycle and the *Pck1/G6pc* remained unchanged, which would leave the fasting level of gluconeogenesis similar to the nominal case in physiological situations. Because our model consists of a complex network of transcription and translation, often times it is difficult to understand and/or predict how a perturbation introduced to one part of the model will affect the dynamics of the rest of the model. Uncertainty and sensitivity analyses can help understand the behavior of the model when challenged with a parameter change as well as to predict what pathways play the most important role in producing a certain output. We first analyzed the entire 130 parameters using the method of local sensitivity analysis, which tells us the behavior of the output when a specific parameter is changed alone. Then we used the computationally efficient Morris method to screen for the most important parameters, both in terms of the impact of single

parameter as well as interaction with other parameters. Finally, we used the RS-HDMR uncertainty analysis on the select parameters from Morris method and ranked them in the order of importance, and extracted interaction effects for specific parameter pairs.

The local sensitivity analysis results in Figure 17 indicate that there are four groups of parameters that have the greatest influence on the amplitude of *Pck1/G6pc*: 1) parameters that mediate the dynamics of the HPA-axis; 2) parameters the modulate the activation of FOXO1 through SIRT1 and PGC-1α; 3) parameters related to cortisol-receptor dynamics; and 4) parameter that govern the *Per/Cry* transcription. In our model, the HPA-axis is responsible for processing the photic input from the light/dark cycle and entraining the cortisol secretion to the peripheral compartment. Since cortisol is one of the main driver for stimulating the expression of *Pck1/G6pc*, it is not surprising that the parameters that mediate the Goodwin oscillator in the HPA-axis plays an important role in modulating the dynamics of gluconeogenesis. The activation of FOXO1 is directly linked to the feeding/fasting cycle via the concentration of NAD^+, the co-activator for SIRT1. FOXO1 is also a driving force for activating the transcription for *Pck1/G6pc*. Therefore, the parameters related to the pathways that process the environmental signals appear to play an important role in modulating hepatic gluconeogenesis in our model. Parameters related to cortisol-receptor dynamics also exhibited high sensitivity coefficients, since it binds to the GRE on the promoter of *Pck1/G6pc*. Finally, parameters modulating *Per/Cry* transcription had high importance because PER/CRY inhibits the cortisol-receptor binding to GRE and activating expression of *Pck1/G6p*.

Morris method performed on 112 peripheral parameters identify overlapping groups of parameters. The results are shown in Figure 18 and Table 1. In Figure 18 where each parameter is plotted on a variance (σ^2) versus absolute mean (μ^*) grid, parameters with great μ^* tend to have a greater σ^2 most of the time. The μ^* and σ^2 values for these 20 parameters are shown along with their identifications in Table 1. Similarly to the local sensitivity analysis, the parameters pertaining to the dynamics of FOXO1, *Per/Cry* transcription, and cortisol receptor has the greatest elementary effects. Morris method identified k_{4b} (Michaelis constant for *Bmal1* transcription) as an important parameter, disagreeing with the local sensitivity analysis. This parameter has the greatest σ^2 value according to Morris method; however, the limitation of Morris method is that it fails to identify parameter pairs are interacting. Furthermore, the method of determining the order of importance from the Morris method results is ambiguous as μ^* and σ^2 must be considered simultaneously.

To address these issues, we used RS-HDMR uncertainty analysis on the 20 parameters identified by Morris method. , From Table 2, we first determined if the sample size of 100,000 would be sufficient for analyzing our model. Since the sum of first and second order variances are less than the total variance, Monte-Carlo integration error is negligible. Furthermoer, the sum of first and second order variances accounted for more than 95% of the total variance; therefore, a sufficient analysis of the model can be performed without considering any higher order variances.

The first order variances for the 20 parameters are listed in the order of importance in Table 3. The parameters related to the PGC-1α and FOXO1 concentrations are the

most important ones according to the HDMR uncertainty analysis, followed by cortisol-receptor dynamics, *Per/Cry* transcription, and *Bmal1* transcription in this order. The second order variances that help identify the most convoluted pathways are presented in a color scheme inFigure 19. Darker cells represent high interaction effects while lighter cells represent low interaction effects. The parameter pair k_{1i} & k_{4b} show the highest interaction effects according to the HDMR analysis. These parameters are each involved in controlling the transcription rate of *Per/Cry* transcription and *Bmal1* transcription. Indeed, PER/CRY and BMAL1 dynamics are closely linked with each other as these proteins influence the transcription rates of each other and of its own. The transcription of *Per* and *Cry* genes are promoted by the CLOCK/BMAL1 heterocomplex. The translated PER/CRY protein inhibits the activation of its own transcription by CLOCK/BMAL1 protein complex. On the other hand, *Bmal1* transcription is indirectly stimulated by the nuclear PER/CRY protein. The interrelated nature of the two clock genes are reflected as a high second order variance in the RS-HDMR analysis. Additionally, parameters contributing to the PGC-1α and FOXO1 dynamics exhibit the next largest second order variance values. While activated PGC-1α in the nucleus activates FOXO1, FOXO1 also regulates PGC-1α by influencing the transcription of PGC-1α gene..

Considering the local sensitivity analysis, Morris method, and RS-HDMR uncertainty analysis together, the local pathways that directly interact with the promoter of the *Pck1/G6pc* (PGC-1α and FOXO1 dynamics, cortisol-receptor dynamics, and PER/CRY dynamics) are the most influential in changing the amplitude of *Pck1/G6pc*. Local sensitivity analysis, the simplest and computationally the most efficient method of

the three, alone, was sufficient for arriving to this conclusion. However, local sensitivity analysis failed to identify parameters that have high interaction effect and low primary effect, such as the Michaelis constant for *Bmal1* (k_{4b}). RS-HDMR uncertainty analysis combined with the Morris method for identifying important parameters was able to identify the interaction of this parameter with inhibition constant for *Per/Cry* transcription (k_{1i}).

Finally, we utilized the results from the sensitivity and uncertainty analyses to alter the behavior of *Clock* KO model. For each of the 20 parameters identified as important from the Morris method, a correction factor was determined so that when the parameter is multiplied with this factor, the *Pck1/G6pc* amplitude will return to a value close to the nominal under light/feeding synchronized condition. These correction factors are listed in Table 3. We took a closer look at the parameters involved in the PGC-1α dynamics. The parameters that contribute to increased concentration of nuclear PGC-1α are below 1, and those that contribute to decreased concentration of nuclear PGC-1α are above 1. Since nuclear PGC-1α activates FOXO1 which promotes the expression of PGC-1α, decreased concentration of PGC-1α would help bring down the high amplitude of *Pck1/G6pc* in the *Clock* KO model back to the nominal amplitude. Moreover, the parameters with larger values of first order variance had correction factors with smaller percentage change from 1, as expected. We then examined if applying these correction factors influenced the system in various ways depending on the local pathways that the parameters belong to, and showed the results in Figure 20. When a parameter involved in the PGC-1α pathway (k_{g1}) was multiplied with the correction factor, the amplitude of *Pck1/G6pc* (20E) was

decreased due to the reduced level of nuclear PGC-1α (20D). When k_{1i}, involved in *Per/Cry* transcription was modified with the correction factor, nuclear PGC-1α level increased slightly (20D), but CLOCK/BMAL1 level (20C) and PER/CRY level (20B) increased compared to the KO model. Due to the increased inhibition effect from PER/CRY, the amplitude of *Pck1/G6pc* was adjusted back down to nominal. When k_{4b}, related to *Bmal1* transcription, was multiplied with the correction factor, The CLOCK/BMAL1 level (20C) was increased closer to the nominal level, and PER/CRY (20B) level was brought back to the nominal level, which resulted in amplitude change for *Pck1/G6pc* (20E). For the three parameters shown inFigure 20, cortisol dynamics (20A) were not changed.

In summary, our model qualitatively captures the dynamics of hepatic gluconeogenesis represented by the transcription of *Pck1/G6pc* entrained to the light/dark cycle and feeding/fasting cycle. The dynamics of *Pck1/G6pc* mRNA are governed by three main driving forces in our model, the cortisol-receptor activating transcription, PER/CRY inhibiting transcription, and FOXO1 mediated by PGC-1α activating transcription. The uncertainty and sensitivity analyses of our model using three different approaches tell us that these three forces, in addition to the cortisol secretion rate from the HPA-axis, are the most important local pathways in the complex network we built. Our model successfully predicts the experimental findings that higher level of cortisol in the periphery increases the level of gluconeogenesis while overexpression of CRY protein results lower level of gluconeogenesis. Using the semi-mechanistic model, we were able to simulate a clock gene knockout condition by forcing very small expression of

CLOCK/BMAL1 protein. Subsequently, we demonstrated that the abnormally high level and amplitude of *Pck1/G6pc* in the KO model can be modified to resemble the nominal level by either targeting specific local pathways in our model and modifying parameters identified through the uncertainty analyses or imposing modifications to the feeding patterns relative to the light/dark cycle. Comparing the correction factors revealed that within a specific local pathway, the parameters with the highest uncertainty in output variance require the smallest correction factor, possibly suggesting that targeting these reactions would be the most efficient in causing alternate behavior for hepatic gluconeogenesis. Furthermore, our model predicts that exposure to constant bright light is detrimental to the robust oscillations of metabolic gene expression. Of course, our model is limited since it does not describe the enzymatic activity of PEPCK and G6PC, changes in glucose and glycogen levels, and other features of hepatic gluconeogenesis. Furthermore, a number of important questions still remain, such as the impact of nutritional composition and the duration of light signal, etc. In the future, we plan to address these questions and incorporate the role of insulin.

CHAPTER 4: Circadian secretion of insulin and its effects on gluconeogenesis

4.1 Introduction

Insulin has a suppressing effect on glucose production and secretion into the bloodstream, the opposite effect of cortisol and SIRT1 from Chapters 2 and 3. Like many

other regulators involved in glucose homeostasis, insulin exhibits circadian rhythmicity. Experiment with perifused rat pancreatic islets show evidence for circadian rhythmicity of insulin release from pancreas.[128] In this study, 30 minute interval measurements over 4 days showed oscillating insulin levels with a period of ~24 hours. Further relationship between insulin level and circadian rithymicity was revealed when adding melatonin advanced the phase by 9h and also enhanced the amplitude of oscillating. Insulin rhythmicity was also confirmed in healthy human volunteers.[129] Glucose clamping experiments showed that insulin secretion rate increased from a nadir between midnight and 6am and reached a peak between noon and 6pm. The study concluded that increasing insulin release during the day and falling insulin release during the night may be one explanation for higher glucose tolerance and insulin response in the morning than at night.

At a molecular level, insulin appears to influence hepatic gluconeogenesis by interacting with transcriptional coactivators and the clock components, summarized in Figure 21. The promoter of PGC-1, an activator of gluconeogenic transcription along with FOXO1 and cortisol-receptor complex, includes insulin response sequences (IRSs).[130] Among the clock genes, hepatic *Bmal1* bi-directionally influence each other. *Bmal1* is post-transcriptionally regulated by signals from insulin.[131] Insulin promotes postprandial Akt-mediated Ser42-phosphorylation of *Bmal1* to induce its dissociation from DNA, eventually leading to nuclear exclusion. Ultimately insulin activity on *Bmal1* results in the suppression of *Bmal1* transcriptional activity. On the other hand, *Bmal1* (and *Per1*) knock-out mice showed lacking clock function in the pancreas, severe

glucose, intolerance, and defective insulin production compared to their littermate controls.[132] Since the isolated pancreatic islets from the mutant mice showed normal insulin content while glucose-stimulated insulin secretion was defective, *Bmal1* may control the release of insulin from the pancreatic islets as opposed to the production of insulin. In addition to *Bmal1*, *Clock* seems to have an important role in controlling insulin secretion in mice.[127] Both *Clock* and *Bmal1* mutants showed impaired glucose tolerance and reduced insulin secretion. Defects in size and proliferation of pancreatic islets were also observed, which worsened with age. Clock disruption resulted in transcriptome-wide alterations in the genes related to growth, survival, and synaptic vesicle assembly. Pancreatic clock disruption also resulted in defective β-cell function, which led to diabetes mellitus for the animals.

More direct evidence for the requirement of functional clock genes for human islet function was found in 2016.[133] In this study, human pancreatic islet cells with knock-out of Clock were assessed for insulin secretion. The results indicated that clock knock-out cells showed a significant decrease in both acute and chronic glucose-stimulated insulin secretion. The synchrony of insulin secretion rhythm was also perturbed upon clock disruption. RNA sequencing results further elucidated that clock genes are involved in insulin secretion rather than production, as among ~300 altered genes were key regulators of insulin secretion (GNAQ, ATP1A1, ATP5G2, and KCNJ11) as well as transcripts required for granule maturation and release (VAMP3, STX6, and SLC30A8).

Since the circadian rhythmicity of insulin secretion appears to be largely driven by the oscillations in insulin granule dynamics, we chose to focus on the dynamics of insulin

granule formation, translocation to the cell membrane, and release to the extracellular space. Briefly, glucose stimulated insulin secretion is tightly related to the cellular ATP/ADP ratio and Ca^{2+} concentration. Increase in glucose concentration causes cellular ATP/ADP ratio to increase, causing closures of ATP-dependent K^{+} channels. When cell membrane is depolarized, opening Ca^{2+} channels and allowing the influx of Ca^{2+} ions. Increased concentration of Ca^{2+} ions mediates the exocitosis of insulin granules.[134,135]

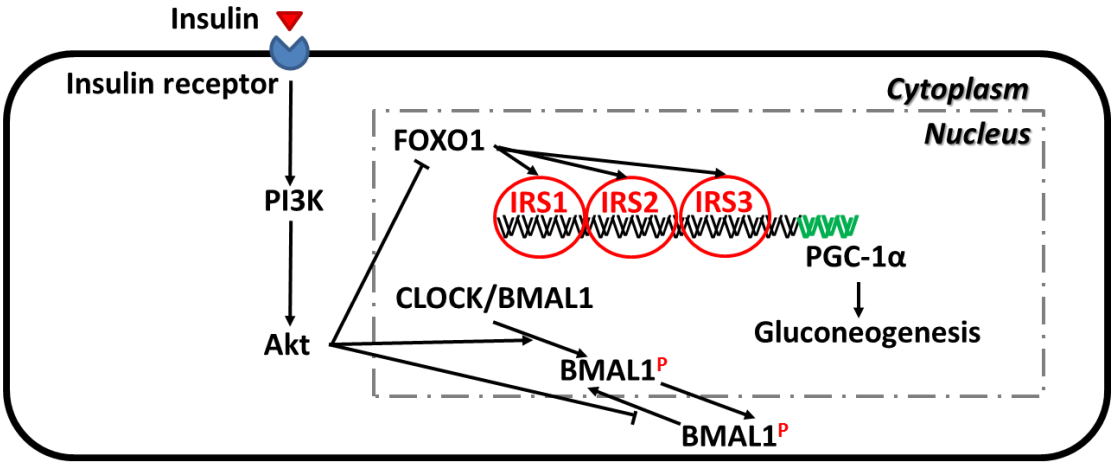

Figure 21: Possible schematic of insulin influence on hepatic gluconeogenesis

To evaluate the role of light of light-feeding phase relations on insulin secretion, we modified the insulin granule trafficking model originally developed by Bertuzzi et al.[136] to describe circadian secretion of insulin from the pancreatic β-cells. In this new model, the parameter describing the production of membrane material oscillates in a circadian manner, resulting in graded insulin secretion response to glucose stimulation. The model predicts that there exists an optimal light-feeding phase relation that maximizes insulin sensitivity, and that meal size distribution also plays an important role in determining the amount of insulin secretion.

4.2 Methods

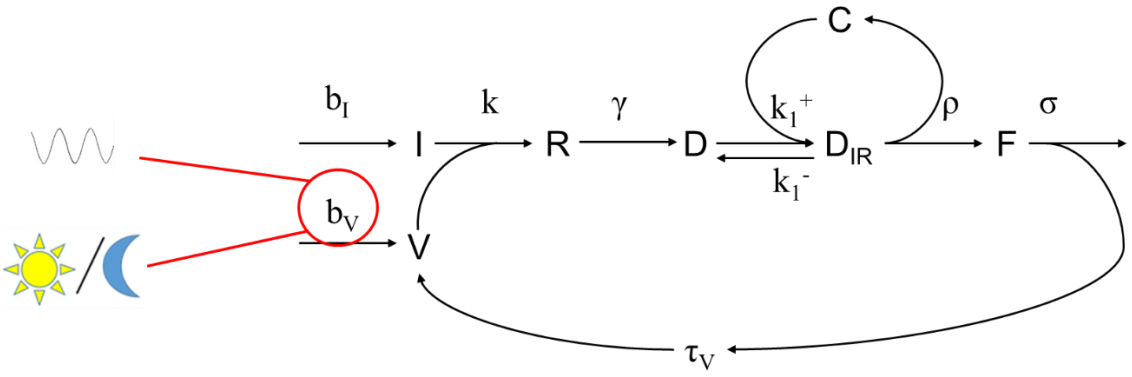

Figure 22: Schematic of the insulin model, adapted from the granule trafficking model[136]

The insulin model was adapted and modified from the insulin granule trafficking model by Bertuzzi et al.[136] and describes the kinetics of four intracellular pools of insulin granules: the reserve pool (R), the pool of docked granules (D), the pool of immediately releasable granules (D_{IR}), and the pool of granules fused with cell membrane (F). The schematic of the model is shown in Figure 22. The dynamics of the above four pools and the pool of proinsulin (I) are described by the following equations:

$$\frac{\mathrm{dI}}{\mathrm{dt}} = -k \cdot I(t) \cdot V(t) - \alpha_I \cdot I(t) + b_I \quad (74)$$

$$\frac{\mathrm{dV}}{\mathrm{dt}} = -k \cdot I(t) \cdot V(t) - \alpha_V \cdot V(t) + b_V + \sigma \cdot F_2 \quad (75)$$

$$\mathrm{b_V} = \begin{cases} k_{Ia} \cdot \sin(k_{Ib} \cdot t - k_{Ic}) + k_{Id} \\ k_{I1} \cdot Bmal - k_{I2} \cdot b_V \end{cases} \quad (76)$$

$$\frac{db_I}{dt} = k_{I5} \frac{k_{I3} \cdot G_2^{k_{In}}}{k_{I4}^{k_{In}} + G_2^{k_{In}}}$$

(77)

$$\frac{\mathrm{dR}}{\mathrm{dt}} = k \cdot I(t) \cdot V(t) - \gamma \cdot R(t)$$

(78)

$$\frac{\mathrm{dD}}{\mathrm{dt}} = \gamma \cdot R(t) - k_1^+ \cdot [C_T - D_{IR}(t)] \cdot D(t) + k_1^- \cdot D_{IR}(t)$$

(79)

$$\frac{\mathrm{dD_{IR}}}{dt} = k_1^+ \cdot [C_T - D_{IR}(t)] \cdot D(t) - k_1^- \cdot D_{IR}(t) - \rho \cdot D_{IR}(t)$$

(80)

$$\frac{\mathrm{dF}}{\mathrm{dt}} = \rho \cdot D_{IR}(t) - \sigma \cdot F(t)$$

(81)

$$\frac{\mathrm{dF_2}}{dt} = \frac{1}{\tau_V} \cdot (F - F_2)$$

(82)

In Equation (74), the dynamics of proinsulin I is described. Here, k is the segregation rate constant for granule membrane material, α_I is the degradation rate of proinsulin, and b_I is a baseline production rate of proinsulin. Equation (75) describes the granule membrane material, V. In this equation, α_V is a degradation rate of granule membranes, b_V is the rate of production of the granule membranes, σ is the rate constant

for the fusion of granule to cellular membrane, and τ_V is the constant time interval required for recycling. In Equation (76), the circadian oscillation of membrane material production is incorporated into the model. The synthesis rate of V, or b_V, is either forced with a sine function that has a nadir at 6am and peak at 6pm, or is an indirect response of *Bmal1* mRNA. The equation was constructed based on the observation that dysfunction of *Bmal1* results in reduced secretion of insulin as well as lost in rhythmicity of insulin secretion.[132] In Equation (78) that describes the insulin reserve pool R, γ is a rate constant that is dependent on the glucose concentration G and represents a main rate-limiting step in the response to glucose (described in Equation (83) later). In Equations (79) and (80), the docked granules D and immediately releasable granules D_{IR} are represented. In these equations, C_T is the constant pool of total Ca^{2+} channels, k_1^+ and k_1^- are the association and dissociation rate constants, and ρ is the rate coefficient that accounts for the factors that promote the fusion of granules with cell membrane (described in Equation (86)). In Equation (82), a transit compartment was added for F to account for the membrane material recycling time τ_V.

$$\frac{\mathrm{d}\gamma}{\mathrm{dt}} = \eta \cdot \{-\gamma(t) + \gamma_b + h_\gamma[G_2]\}$$

(83)

$$\frac{\mathrm{dG_2}}{dt} = \frac{1}{\tau_G} \cdot (G - G_2)$$

(84)

$$\mathrm{h}_{\gamma}(G) = \begin{cases} 0, & G \le G^{*} \\ \dfrac{\hat{h}(G - G^{*})}{\hat{G} - G^{*}}, & G^{*} < G \le \hat{G} \\ \hat{h}, & G > \hat{G} \end{cases}$$

(85)

$$\frac{\rho}{\mathrm{dt}} = \zeta \cdot \{\rho(t) + \rho_{b} + h_{\rho}[\gamma(t)]\}$$

(86)

$$\mathrm{h}_{\rho}(\gamma) = \begin{cases} 0, & \gamma < \gamma_{b} \\ k_{\rho} \cdot (\gamma - \gamma_{b}), & \gamma \ge \gamma_{b} \end{cases}$$

(87)

Equations (83)-(87) describe the triggering of insulin secretion by glucose stimulation. In Equation (83), γ represents the rate coefficient of granule externalization, related to the ratio ATP/ADP, previously appeared in Equation (79) to describe the docked pool. In the same equation, η is a rate constant, and γ_b is the basal value at low glucose. Equation (84) is a transit compartment for smoothing out the glucose concentration. Here, τ_G, the time required for glucose metabolism, was selected to replicate the daily glucose concentration profile in healthy subjects[137]. The The glucose activation model h_γ is described by Equation (85), where $\hat{h}$ is the maximal value of h_γ and is reached at $G=\hat{G}$. Below the threshold of G*, h_γ is 0, and between G* and $\hat{G}$, the function increases linearly. Equation (86) describes the behavior of ρ, the rate coefficient of granule fusion with cell membrane, determined by the calcium concentration. In Equation (86), ζ is a rate constant, and ρ_b is the basal value of $[Ca^{2+}]$.

The function h_ρ, which embodies the action of ATP on Ca^{2+}, is described in Equation (87).

$$\mathrm{ISR(t)} = \mathrm{I_0} \cdot \sigma \cdot F(t) \cdot f(t) \cdot N \quad (88)$$

$$\mathrm{f(G)} = \begin{cases} f_b, & G < G^* \\ f_b + (1 - f_b)\dfrac{G - G^*}{K_f + G - G^*}, & G \geq G^* \end{cases} \quad (89)$$

The insulin secretion rate is defined in Equation (88), where I_0 is the insulin amount contained in granule, and N is the total number of β-cells in the pancreas. The fraction of the total cell population which responds to glucose, f, is defined in Equation (89).

4.3 Results

Our insulin secretion model aims to depict the dependence of glucose-stimulated insulin response on circadian time. To achieve this goal, we first tried to investigate how imposing an oscillatory behavior on production of granule membrane material V can alter the insulin granule dynamics under glucose stimulation. In

Figure 23: Sample simulation results for pulse glucose stimulation. The time profiles for glucose concentration in mmol/L (A), reserve pool R (B), docked pool D (C), and ISR in μg/hr (D) are shown., a sample of the simulation results for pulse glucose stimulations is available. For this figure, the amplitude of oscillation of b_V (k_{Ia}) was set to

3, and the average level of the vertical shift (k_{Id}) was set to 6. The values of the rest of the parameters are shown in Table A3. The resulting V profile has a nadir at 4m and a peak at 4pm, 2 hours before the starting and ending time of the light (active) period, to simulate the effect of *Bmal1* mRNA which peaks in the afternoon. The system was first stabilized at a glucose concentration of 1 mmol/L for 24 hours. Then a 1 hr pulse at 16.7 mmol/L was applied at different times of the day in 2 hour increments, returning to 1 mmol/L immediately after the pulse. Example profiles of glucose is shown in

Figure 23: Sample simulation results for pulse glucose stimulation. The time profiles for glucose concentration in mmol/L (A), reserve pool R (B), docked pool D (C), and ISR in μg/hr (D) are shown.A. The resulting ISR profiles are shown in

Figure 23: Sample simulation results for pulse glucose stimulation. The time profiles for glucose concentration in mmol/L (A), reserve pool R (B), docked pool D (C), and ISR in μg/hr (D) are shown.D. From this figure, it is evident that identical pulse glucose stimulations at different times of the day can cause differences in ISR. ISR peak is the highest if the pulse is applied at 4pm, at the peak of b_V. Once glucose concentration is returned to 1mmol/L, ISR also becomes 0. However, lasting effects of glucose stimulation are observed post pulse time in intermediates such as R (23B) and D (23C).

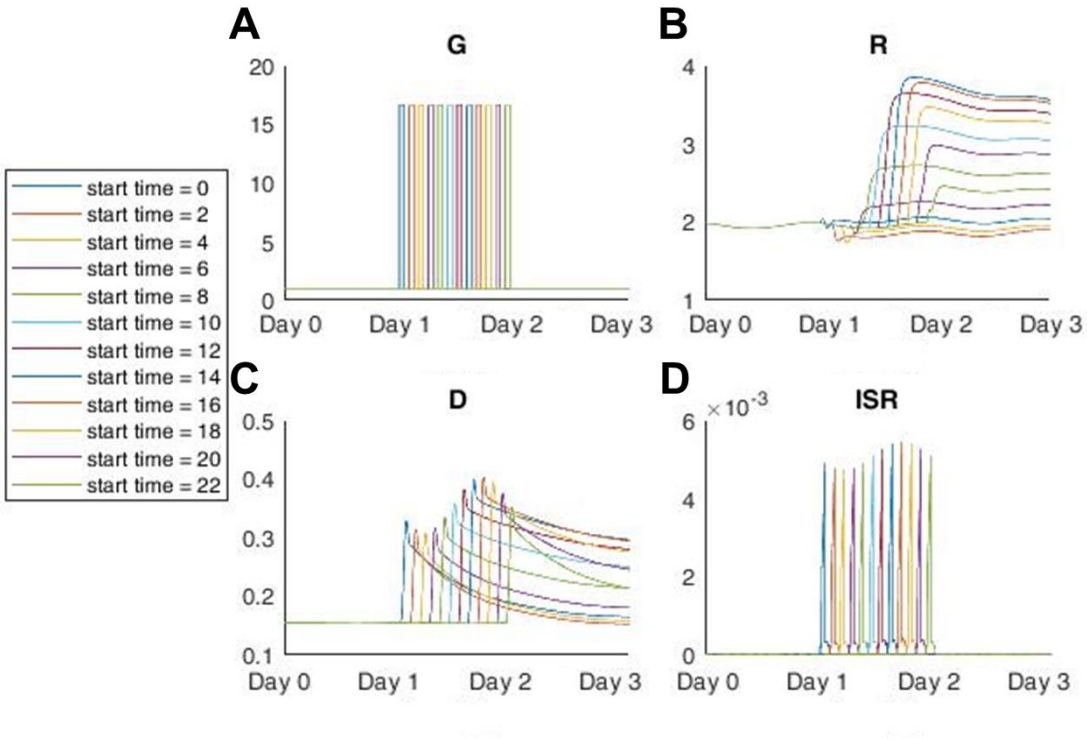

Figure 23: Sample simulation results for pulse glucose stimulation. The time profiles for glucose concentration in mmol/L (A), reserve pool R (B), docked pool D (C), and ISR in µg/hr (D) are shown.

In Figure 24, a sample model simulation using glucose infusion as stimulus is shown. In this figure, glucose concentration was initially set to 0 mmol/L for the first 24 hours, then the glucose concentration was raised to 16.7 mmol/L at different times of the day in 2 hour increments in the next 24 hours. The glucose concentration profiles are shown in Figure 24A, and the resulting ISR profiles are shown in 23D. Among the intermediate pools, R (23B) and D (23C) are also shown. The intermediates R and D oscillate with very low amplitude prior to glucose stimulation. Once glucose infusion is started, the amplitude of R and D increase and insulin secretion begins. After the initial 24 hours into glucose infusion (by Day 3), system reaches steady state and all profiles oscillate with an identical amplitude and phase regardless of when glucose infusion

started. However, the transient behavior for the initial 24 hours into glucose infusion depends on stimulation start time. For example, the maximum value and AUC of ISR and R over the first 24 hours depends on the circadian time of infusion start.

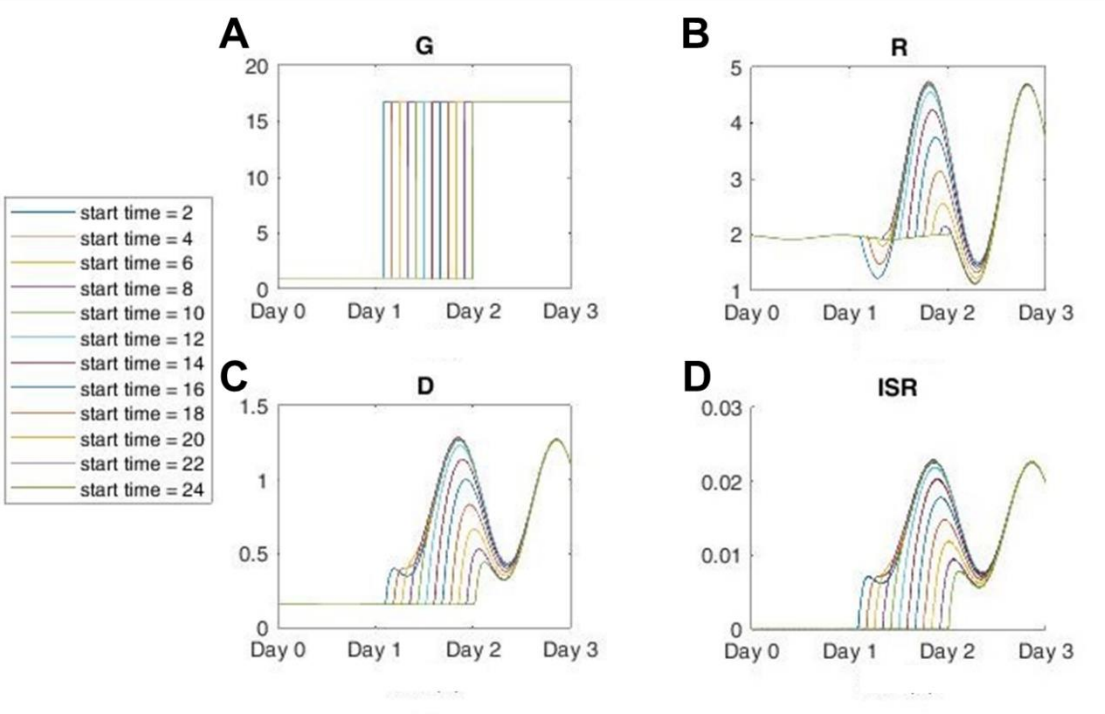

Figure 24: Sample simulation results for glucose infusion. The time profiles for glucose concentration in mmol/L (A), reserve pool R (B), docked pool D (C), and ISR in µg/hr (D) are shown.

Next, we wished to evaluate the effect of glucose concentration insulin secretion under glucose pulse and infusion stimulations. The previously described simulations using 1 hr pulse and continuous glucose infusion were performed again at glucose concentration of 9 mmol/L and 5 mmol/L. Then, the maximum value and AUC of the R and ISR during the first 24 hours after glucose stimulation were found and plotted in Figure 25. Examining Figure 25A, we observe that AUC of ISR after glucose pulse is greater when glucose stimulation concentration is greater. The peak value of ISR follows the same pattern. AUC and maximum value of R has a greater circadian dependence

when glucose concentration is greater. For both R and ISR, maximum AUC is achieved if pulse occurs at 16 circadian hours, 2 hours prior to the peak of b_V. In the case of infusion stimulation, maximum insulin secretion during the transient phase is achieved if infusion starts at 8 or 10 circadian hours. If infusion starts at the peak of b_V, the transient secretion rate is at the minimum.

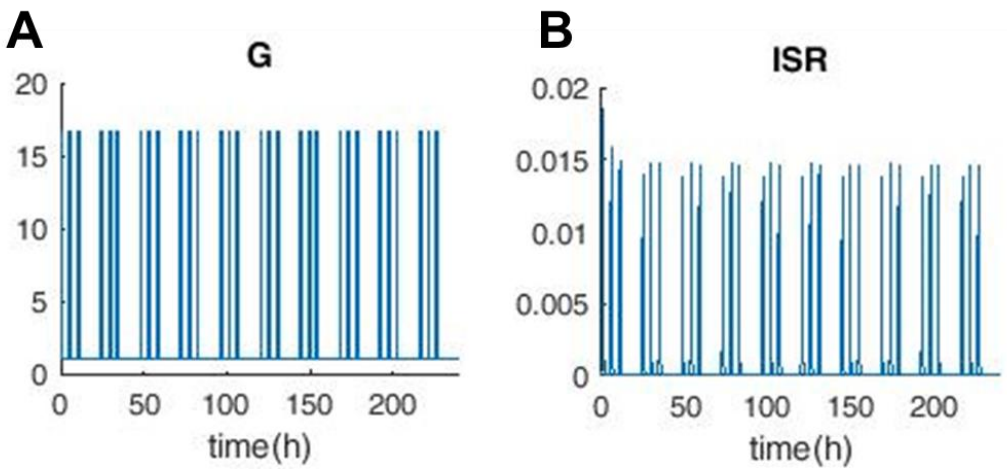

Figure 25: Sample simulation results for 3 meals/day glucose stimulation. Glucose concentration G is in mmol/L (A) and ISR is in μg/hr (B).

In Figure 26, we attempt to show the effect of oscillation characteristics of b_V on ISR under 3 meals/day glucose stimulation pattern. In this figure, the AUC of ISR on the 10^{th} day are plotted against the breakfast start time. In Figure 26A, the data for low vertical shift (average level of b_V) is plotted. Figure 26B shows the data for medium vertical shift, and 26C shows the data for high vertical shift. For each vertical shift, three different amplitude of b_V was tested. Examining the data together, higher level of b_V leads to higher AUC of ISR while greater amplitude of b_V leads to greater differences in AUC of ISR depending on the meal start time. For all cases, the most amount of insulin is secreted if breakfast is started at 10am.

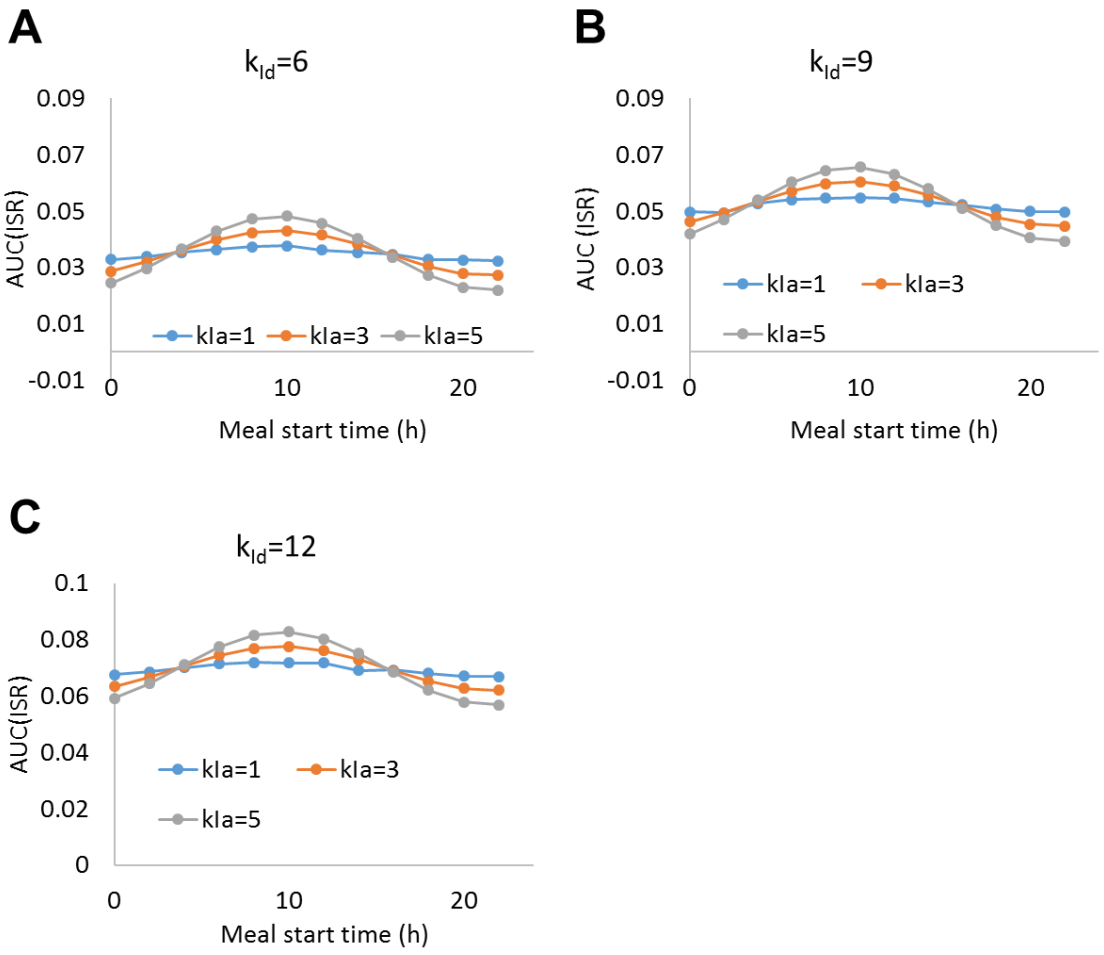

Figure 26: Effect of breakfast start time on AUC of ISR (µg) with differing rhythms of b_V. In this figure, k_{id} is the vertical shift and k_{ia} is the amplitude of the V rhythm.

In Figure 27, the effect of circadian characteristics on glucose stimulated insulin secretion is examined in more detail. In this figure, first peaks (resulting from breakfast) are shown as squares, second peaks are depicted as circles, and third peaks are denoted as triangles. Data for b_V oscillating with low amplitude (27A), medium amplitude (27B), and high amplitude (27C) are shown on separate plots. For each amplitude, data from b_V rhythms with low level (green), medium level (yellow), and high level (red) are shown. From Figure 27, we observe that the ISR peak level is higher for later meals in general. If the glucose stimulation is started during the light period (between 6am and 6pm),

breakfast peak is the lowest and dinner peak is the highest. Interestingly, the difference between breakfast and lunch peaks is larger than the difference between lunch and dinner peaks, a phenomenon observed in human subjects.[138] The increased insulin secretion for dinner under identical caloric intake was also confirmed by a study that provided identical meals in 6 or 12 hour increments.[139] The difference between ISR peaks within a day is greater if the breakfast is started during the light phase. If the meals are started during the eark phase, the peak differences are reduced, especially between lunch and dinner. Additionally, peak differences are greater if b_V rhythm has a higher amplitude (27B and 27C). However, for low amplitude rhythms (27A), the peak differences are consistent regardless of meal start time.

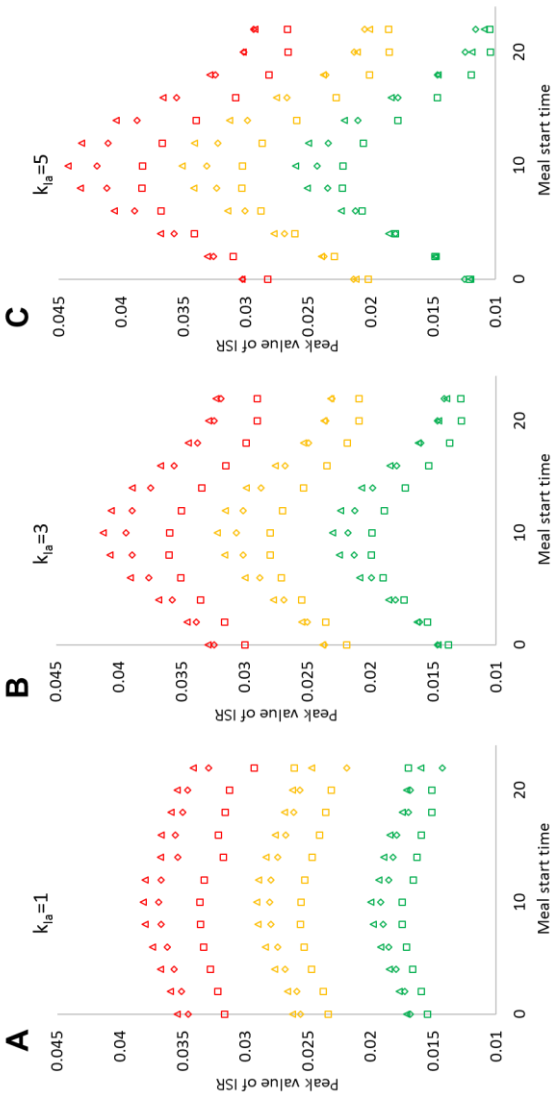

Figure 27: Relative ISR (µg) peak values for the three meals. First peaks are depicted as squares, second peaks as circles, and third peaks as triangles. Data for low amplitude rhythm (A), medium amplitude rhythm (B), and high amplitude rhythm (C) are shown separately. Within each figure, data for rhythms with low (green), medium (yellow), and high (red) vertical shifts are shown next to one another.

Figure 26 and Figure 27 show that insulin secretion is greatest with identical glucose stimulation if the first meal of the day is started at 10am. In Figure 28, the AUC of ISR during the dark period and light period over a 24 hour day are compared. Data for b_V oscillating with low amplitude (28A), medium amplitude (28B), and high amplitude (28C) are shown on separate plots. For each amplitude, data from b_V rhythms with low

level, medium level, and high level are compared next to each other. For all rhythms of V, insulin secretion during the light period is greatest if the meals are started at 6am. If the meals are started at 6pm, most of the insulin is secreted during the dark phase. The relative insulin secretion between light and dark periods are similar among meal start times between 8am and 12pm.

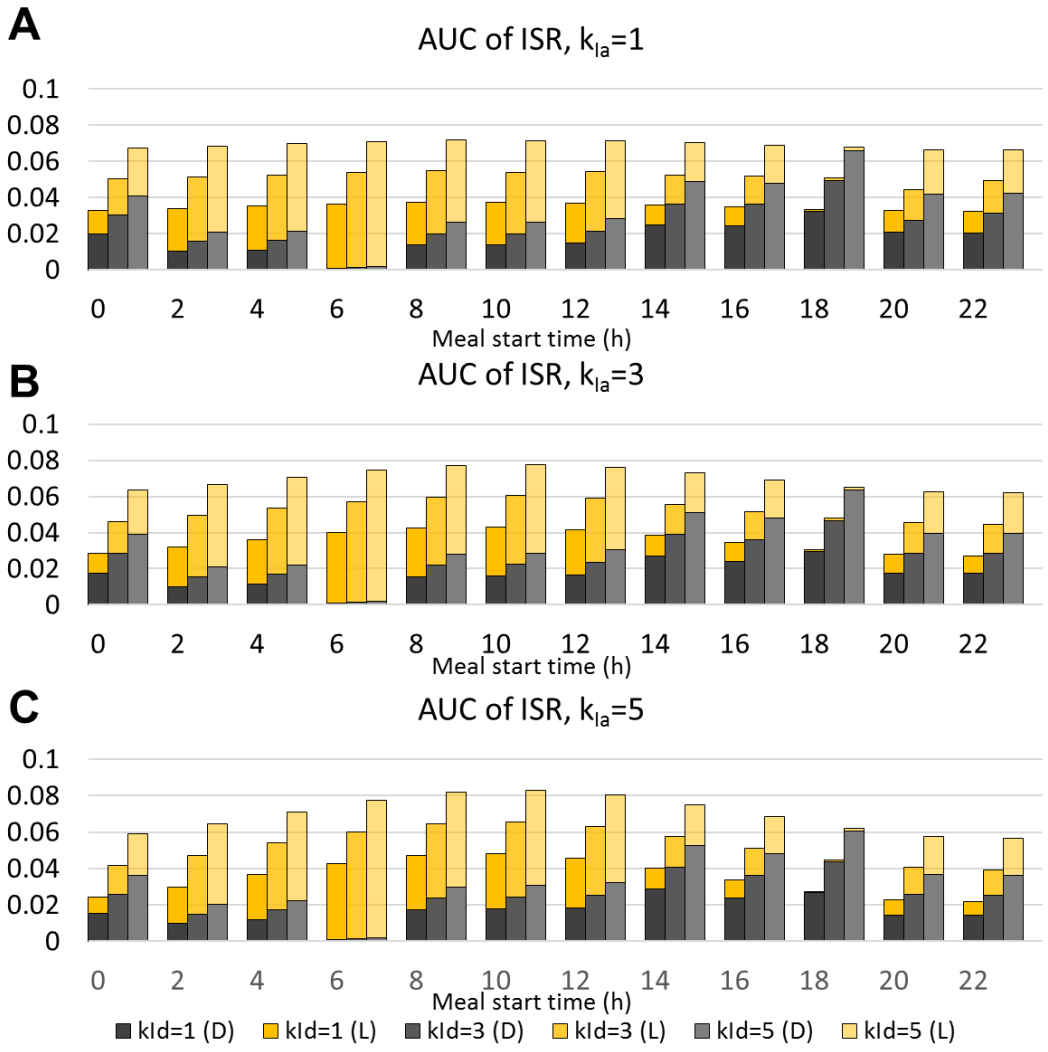

Figure 28: AUC of ISR (µg) during the light and dark period for different rhythms of bV. Data for low amplitude rhythm (A), medium amplitude rhythm (B), and high amplitude rhythm (C) are shown separately. Within each figure, data for rhythms with low, medium, and high vertical shifts are shown next to one another.

Next, we tested weather having meals of different size throughout the 3-meal day can have an effect on the overall insulin secretion, and showed the results in Figure 29. For the “small dinner” meal pattern, three glucose pulses occur during the 12 hour active phase, starting with a 1 hour pulse at 16.7 mmol/L. The lunch is a 1 hour pulse glucose stimulation at 75% of the breakfast concentration, and the diner is 1 hour pulse at 50% of the breakfast concentration. For the “small breakfast” meal pattern, the pulses appear in the reverse order. For the “3 equal meals” meal pattern, all pulses are at 75% of the maximum concentration. Therefore, for all three meal patterns, the AUC of glucose concentration over a 24 hour day is identical. The system was allowed to reach steady-state and the AUC of ISR on the 10^{th} day was calculated and plotted. Figure 29 shows that when compared to 3 equal meals, small dinner meal pattern will produce less insulin if meals are started during late night morning time. In contrast, big dinner meal pattern will produce less insulin than the 3 equal meals in almost all cases, although the difference between the two during the late night phase is small.

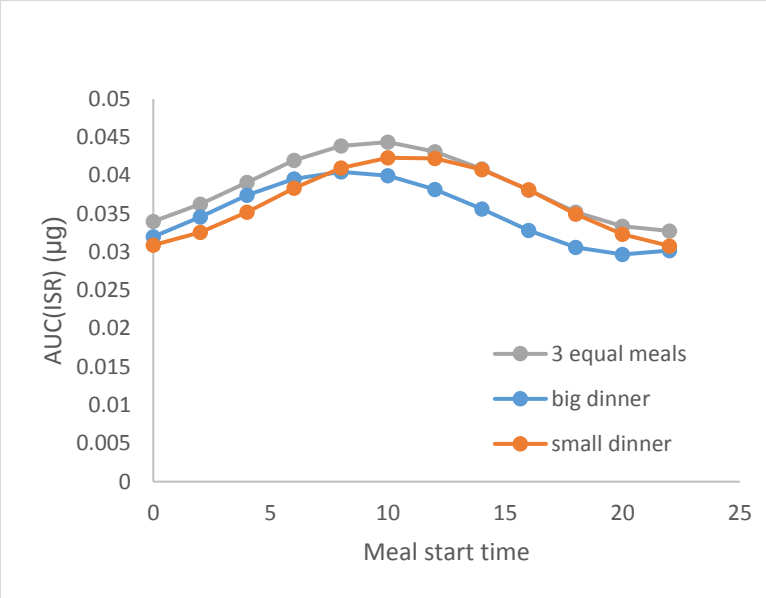

Figure 29: AUC of ISR for different meal size distributions

The relative ISR peak values for breakfast, lunch, and dinner are also changed depending on the meal size distribution (Figure 30). As described previously, providing 3 equal meals causes ISR peak level to increase toward the end of the day. If dinner concentration is higher than breakfast, the peaks still increase toward the later meals, with smaller breakfast peaks and higher dinner peaks. If breakfast concentration is higher than dinner, peak values decrease toward the end of the day.

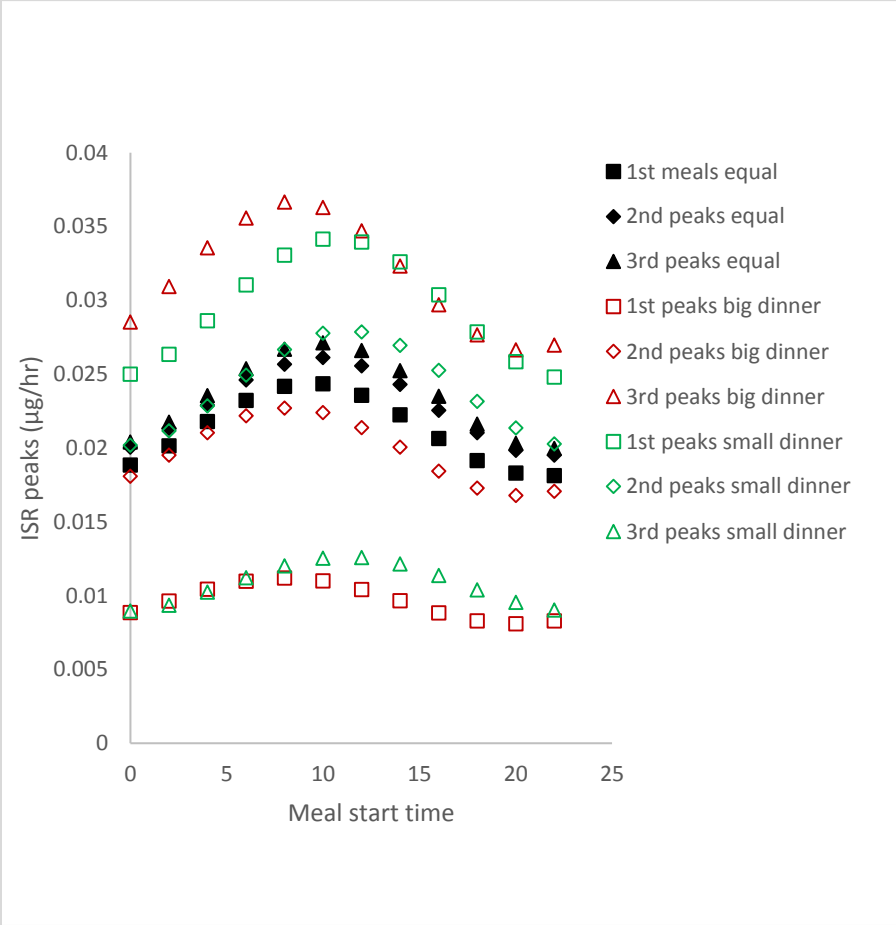

Figure 30: ISR peak values for breakfast, lunch, and dinner for different meal size distributions

To evaluate the role of light-feeding phase relations on insulin secretion, the gluconeogenesis model from Chapter 3 was incorporated into the insulin model. The production rate of V was expressed as an indirect response from *Bmal1* mRNA, as shown in Equation (76). Three 1 hr meals at 16.7 mmol/L spread out over 12 hours was given to the model. When glucose stimulation was on, feeding signal was set to 4, so that the AUC of feeding matches the AUC of light, which was on at 1 from 6am to 6pm. This set up was tested with the first meal starting at different times of the day in 2 hour increments. The resulting AUC of ISR on the 10^{th} day is shown in Figure 31A, along with the amplitude of *Bmal1* mRNA. Increase in *Bmal1* oscillation amplitude results in

higher ISR, resulting in highest insulin secretion if the meal is started at 8am, 2 hours after the light phase starts. We applied a constant light condition (light is set to 1 constitutively) to test the effect of circadian disruption on ISR. Figure 31A and B show that insulin secretion is reduced if the system experiences constant light, consistent with data from rodents exposed to bright light.[140,141]

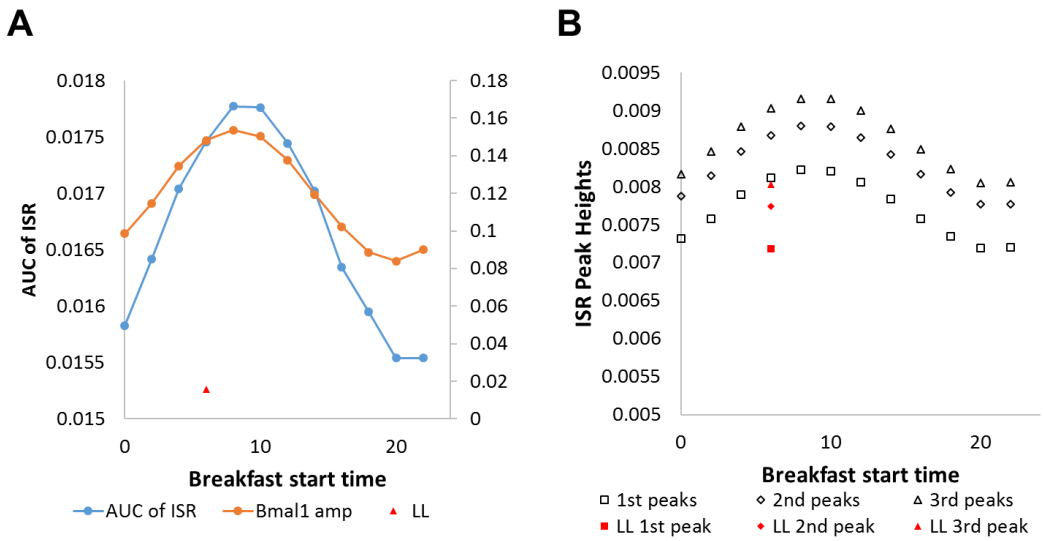

Figure 31: The light/dark cycle and feeding/fasting cycle drives the oscillation of b_V. The AUC of ISR (µg) is shown with amplitude of Bmal1 mRNA (A). The effect of constant light is shown in red.

Figure 32 shows the effects of meal size distribution in the circadian insulin model. For the small dinner meal pattern, 1 hour breakfast pulse was set at feeding level of 4 and glucose concentration of 16.7 mmol/L. Lunch was a 1 hour pulse with 75% of the breakfast amplitude, and dinner was a 1 hour pulse with 50% of the breakfast amplitude. For the big dinner meal pattern, the pulses appeared in the reverse order. For 3 equal meals, all pulses were set at 66% of the maximum level to achieve identical AUC of feeding and glucose stimulation over a 24 hour period. Light was on at 1 from 6am to 6pm. For all meal patterns, the system was allowed to reach steady state and the AUC

over ISR on the 10th day was calculated and plotted on Figure 32, along with the AUC of granule membrane V. For all meal patterns, AUC of ISR is greatest when AUC of V is greatest. For 3 equal meals and small dinner, insulin secretion is greatest if meals are started at 8am. However, insulin secreation peaks if meals are started at 10 am if dinner is the largest meal of the day. Additionally, providing 3 equal meals results in highest insulin secretion regardless of the meal start time. Large dinner results in the lowest insulin secretion.

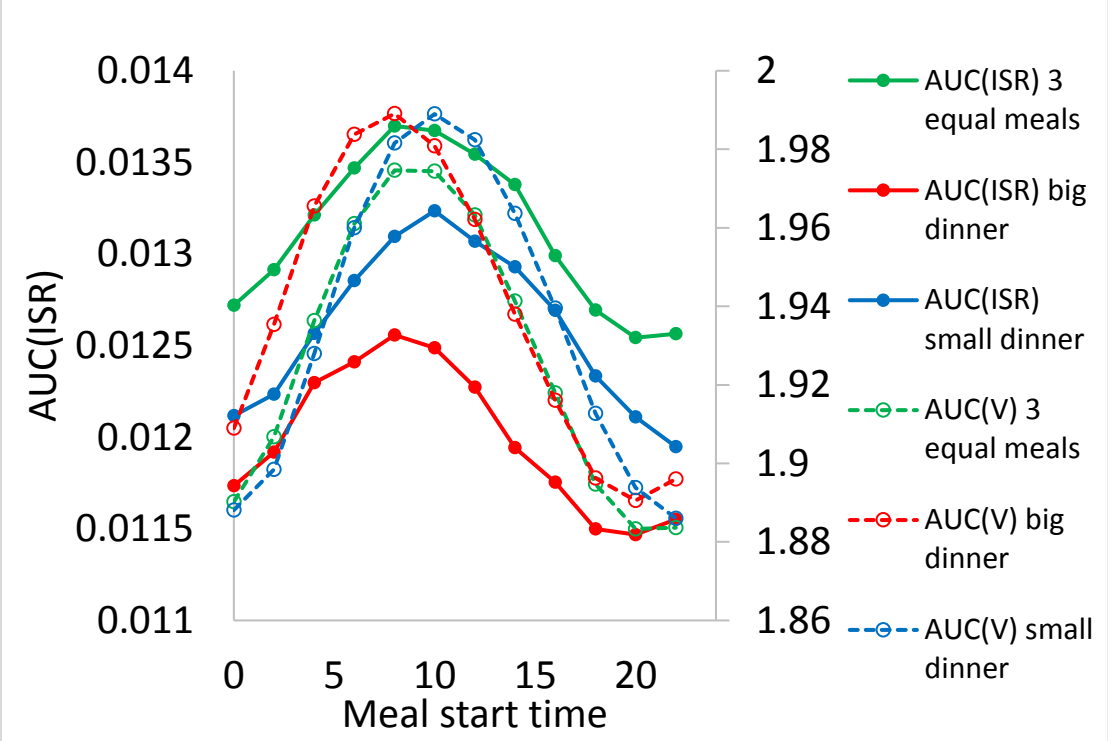

Figure 32: The effect of meal distribution and meal time on AUC of ISR (μg) is shown for the insulin model where b_V is driven by light/dark cycle and feeding/fasting cycle.

4.4 Discussion

Evidence for circadian secretion of insulin exist at multiple levels, from tissue cultures of rat pancreatic islets[128] to healthy human volunteers.[129] RNA sequencing of human pancreatic islet cells with knock-out of clock genes suggest that insulin secretion, rather than production, is under circadian control.[133] As such, we have developed a model to study the circadian rhythmicity in glucose-stimulated insulin secretion, incorporating the dynamics of granule maturation and release.[136] Using this model, we investigated how the oscillatory characteristics of circadian rhythms can influence the time of the day dependence on insulin secretion rate. Furthermore, we studied how meal size distribution can change the insulin secretion rate throughout a 24-hour day.

In Figure 27 and Figure 30, the model predicts that the first ISR peak of the day is the lowest peak of the day. The second and third peaks are higher than the first peak in most cases, except for the case where the granule membrane synthesis rate (b_V) oscillates with a high amplitude and low level and meals are started during the middle of the dark phase. Since we observe that this peak pattern appears regardless of when the first meal of the day is started, we can deduce that the increase in peak level for later meals is not due to the oscillations in b_V. Instead, the increase is due to the lasting effects of the meal on the granule dynamics. Figure 23 shows that although ISR returns to zero immediate after glucose pulse is over, the increased level of the reserved pool (R) and docked granules (D) remain at higher levels. Additionally, the increase in levels of these intermediates is higher when b_V is increased. Highest ISR peaks and AUC of ISR are achieved when b_V has a steep positive slope.

Figure 26 shows that overall ISR over a 24-hour day is dependent on the oscillatory characteristics of b_V. We observe a vertical shift in the AUC of ISR as the average level of b_V is increased. If average level of b_V is identical but the amplitude of oscillation is increased, AUC of ISR also varies in greater magnitude depending on when the meals are started. The same trend is observed in Figure 28. Additionally in Figure 28, the proportion between AUC of ISR during the light and dark periods vary depending on the meal start time, but is not affected by the amplitude or the level of b_V. An interesting phenomenon is jump in the proportion of ISR during the light and dark periods between certain times of the day. Alternatively, the proportion is very similar for some meal start times. For example, meals started at 8am, 10am, and 12pm would yield similar proportions. We observe this due to the spacing of the meal times. Since the three meals are equally distributed between 12 hours, starting the first meal at these times would result in two meals given during the light phase and one meal given during the dark phase, resulting in similar ISR proportions.

Figure 29**,** Figure 30**,** and Figure 32 show the effects of unequal meal sizes on ISR. Figure 32 shows that when the light/dark cycle is incorporated into the model maximum ISR is achieved if three equal meals are presented to the system. Having a big dinner and small breakfast will result in the lowest ISR, and the ISR from combination of small dinner and big breakfast will be in the middle. Additionally, the meal start time that results in the greatest ISR for small dinner is the earliest, followed by 3 equal meals, and then big dinner. The same meal start times also result in the greatest AUC of V for each meal pattern, as represented in the dotted line in the same graph. This pattern is consistent

in Figure 29, before the light/dark cycle was incorporated into the model. Figure 30 can provide more insight into the differences in ISR resulting from meal size distributions. For three equal meals, ISR peaks increase toward the later meals, but the three peaks are close together compared to the other two meal patterns. In the case of big dinner, the peaks still increase toward the end of the day but the differences between the peaks are greater compared to the equal meals. In the case of small dinner, the peaks decrease toward the end of the day. Examining Figure 30 more closely can help elucidate the reason for observing lower AUC of ISR for big dinner meal patter in Figure 32. In Figure 30, the second peaks for small dinner are always higher than the second peaks for big dinner, although the meal sizes are identical. The above relationship occurs because a larger breakfast will cause the reserve pool (R) to be at a higher level when the system receives the lunch pulse. Because granule levels are already more elevated at the time of lunch, identical stimulation results in greater ISR for small dinner case.

In summary, our model shows that glucose-stiulated insulin release from the pancreatic β-cells can change due to the oscillatory characteristics of circadian rhythms in insulin granule formation and fusion. Although ISR is raised for later meals of the day, this pattern can be altered depending on the oscilation amplitude and level of granule membrane material. Furthermore, our model suggests that distributing the meal sizes differently can alter the level of ISR.When the effects of light/dark cycle is incorporated, the model predicts that having a small breakfast and large dinner results in lower ISR compared to other meal patterns, regardless of what circadian time the meals are first

started. In the future, the influence of insulin on clock genes should be represented in for more accurate description of the interaction between insulin and circadian clocks.

CHAPTER 5: Conclusions

Metabolic diseases caused by circadian disruption has been extensively reported in literature, both at the molecular level and the clinical level. Restoration of circadian rhythms by time-restricted feeding has been shown to reverse the metabolic abnormalities in some cases. Therefore, there is a need to understand how the biological clock affects metabolic reactions, and how environmental factors such as light and feeding cycles can modulate a downstream biological process at a molecular level. I have developed a semi-mechanical mathematical model to predict the effect of phase relation between light and feeding cycles on hepatic gluconeogenesis. As a first step, the entrainment of peripheral clock genes by two conflicting environmental cues, light and food availability, was described. Then, the model was further extended to include the downstream hepatic gluconeogenesis. Finally, circadian secretion of insulin was modeled based on granule trafficking mechanism. The works described in this thesis provide an insight into the dynamics of glucose metabolism under various environmental factors, transmitted through multiple entrainers such as cortisol SIRT1, and insulin. The models predict that a few hours of restricted feeding in the early active phase is beneficial for robust oscillation of peripheral clock genes, appropriate level of gluconeogenesis, and maximum secretion of insulin. Analyzing the dynamics of the model also contributes to understanding how circadian disruption or restoration affects the progression of metabolic diseases.

Furthermore, this understanding could ultimately be applied in the development of non-pharmacological interventions, such as chronotherapy, for metabolic diseases. There are limitations to the model including the lack of consideration for the roles of melatonin and sexual dimorphism in controlling glucose metabolism, and future studies should address these issues.

Acknowledgements of previous publications

This dissertation contains significant portions of the following publications:

1. Bae SA, Androulakis IP. Mathematical Analysis of Circadian Disruption and Metabolic Re-entrainment of Hepatic Gluconeogenesis: The intertwining entraining roles of light and feeding. 2018. **American Journal of Physiology Endocrinology and Metabolism**.

2. Bae SA, Androulakis IP. The Synergistic Role of Light-Feeding Phase Relations on Entraining Robust Circadian Rhythms in the Periphery. **Gene regulation and systems biology**. 2017; 11. PMCID: PMC5404903

References

1. Asher G, Schibler U. Crosstalk between Components of Circadian and Metabolic Cycles in Mammals. *Cell Metab.* 2011;13(2):125-137.

2. Bellet MM, Orozco-Solis R, Sahar S, Eckel-Mahan K, Sassone-Corsi P. The time of metabolism: NAD+, SIRT1, and the circadian clock. *Cold Spring Harb Symp Quant Biol.* 2011;76:31-38.

3. Eckel-Mahan K, Sassone-Corsi P. Metabolism control by the circadian clock and vice versa. *Nat Struct Mol Biol.* 2009;16(5):462-467.

4. Spiegel K, Tasali E, Leproult R, Van Cauter E. Effects of poor and short sleep on glucose metabolism and obesity risk. *Nat Rev Endocrinol.* 2009;5(5):253-261.

5. Gallou-Kabani C, Vige A, Junien C. Lifelong circadian and epigenetic drifts in metabolic syndrome. *Epigenetics.* 2007;2(3):137-146.

6. Karlsson B, Knutsson A, Lindahl B. Is there an association between shift work and having a metabolic syndrome? Results from a population based study of 27,485 people. *Occup Environ Med.* 2001;58(11):747-752.

7. Chaput JP, Brunet M, Tremblay A. Relationship between short sleeping hours and childhood overweight/obesity: results from the 'Quebec en Forme' Project. *Int J Obes (Lond).* 2006;30(7):1080-1085.

8. Vollmers C, Gill S, DiTacchio L, Pulivarthy SR, Le HD, Panda S. Time of feeding and the intrinsic circadian clock drive rhythms in hepatic gene expression. *Proc Natl Acad Sci U S A.* 2009;106(50):21453-21458.

9. Reppert SM, Weaver DR. Coordination of circadian timing in mammals. *Nature.* 2002;418(6901):935-941.

10. Rutter J, Reick M, Wu LC, McKnight SL. Regulation of clock and NPAS2 DNA binding by the redox state of NAD cofactors. *Science.* 2001;293(5529):510-514.

11. Bellet MM, Sassone-Corsi P. Mammalian circadian clock and metabolism - the epigenetic link. *J Cell Sci.* 2010;123(Pt 22):3837-3848.

12. Mohawk JA, Green CB, Takahashi JS. Central and peripheral circadian clocks in mammals. *Annu Rev Neurosci.* 2012;35:445-462.

13. Luna A, McFadden GB, Aladjem MI, Kohn KW. Predicted Role of NAD Utilization in the Control of Circadian Rhythms during DNA Damage Response. *PLoS Comput Biol.* 2015;11(5):e1004144.

14. Shi M, Zheng X. Interactions between the circadian clock and metabolism: there are good times and bad times. *Acta Biochim Biophys Sin (Shanghai).* 2013;45(1):61-69.

15. Thakran S, Sharma P, Attia RR, et al. Role of sirtuin 1 in the regulation of hepatic gene expression by thyroid hormone. *J Biol Chem.* 2013;288(2):807-818.

16. Bishop NA, Guarente L. Genetic links between diet and lifespan: shared mechanisms from yeast to humans. *Nat Rev Genet.* 2007;8(11):835-844.

17. Sahar S, Sassone-Corsi P. Regulation of metabolism: the circadian clock dictates the time. *Trends Endocrinol Metab.* 2012;23(1):1-8.

18. Mavroudis PD, Corbett SA, Calvano SE, Androulakis IP. Mathematical modeling of light-mediated HPA axis activity and downstream implications on the entrainment of peripheral clock genes. *Physiol Genomics.* 2014;46(20):766-778.

19. Nelson DL, Lehninger AL, Cox MM. *Lehninger principles of biochemistry.* Macmillan; 2008.

20. Young JW. Gluconeogenesis in cattle: significance and methodology. *J Dairy Sci.* 1977;60(1):1-15.

21. Lamia KA, Storch KF, Weitz CJ. Physiological significance of a peripheral tissue circadian clock. *Proc Natl Acad Sci U S A.* 2008;105(39):15172-15177.

22. Zhang EE, Liu Y, Dentin R, et al. Cryptochrome mediates circadian regulation of cAMP signaling and hepatic gluconeogenesis. *Nat Med.* 2010;16(10):1152-1156.

23. Kalsbeek A, la Fleur S, Fliers E. Circadian control of glucose metabolism. *Mol Metab.* 2014;3(4):372-383.

24. Khani S, Tayek JA. Cortisol increases gluconeogenesis in humans: its role in the metabolic syndrome. *Clin Sci (Lond).* 2001;101(6):739-747.

25. Goldstein RE, Reed GW, Wasserman DH, et al. The effects of acute elevations in plasma cortisol levels on alanine metabolism in the conscious dog. *Metabolism.* 1992;41(12):1295-1303.

26. Seubert W, Henning HV, Schoner W, L'Age M. Effects of cortisol on the levels of metabolites and enzymes controlling glucose production from pyruvate. *Adv Enzyme Regul.* 1968;6:153-187.

27. Lamia KA, Papp SJ, Yu RT, et al. Cryptochromes mediate rhythmic repression of the glucocorticoid receptor. *Nature.* 2011;480(7378):552-556.

28. Schwer B, Verdin E. Conserved metabolic regulatory functions of sirtuins. *Cell Metab.* 2008;7(2):104-112.

29. Matsuzaki H, Daitoku H, Hatta M, Tanaka K, Fukamizu A. Insulin-induced phosphorylation of FKHR (Foxo1) targets to proteasomal degradation. *Proc Natl Acad Sci U S A.* 2003;100(20):11285-11290.

30. Frescas D, Valenti L, Accili D. Nuclear trapping of the forkhead transcription factor FoxO1 via Sirt-dependent deacetylation promotes expression of glucogenetic genes. *J Biol Chem.* 2005;280(21):20589-20595.

31. Yoon JC, Puigserver P, Chen G, et al. Control of hepatic gluconeogenesis through the transcriptional coactivator PGC-1. *Nature.* 2001;413(6852):131-138.

32. Mavroudis PD, Corbett SA, Calvano SE, Androulakis IP. Circadian characteristics of permissive and suppressive effects of cortisol and their role in homeostasis and the acute inflammatory response. *Math Biosci.* 2015;260:54-64.

33. Ramsey KM, Yoshino J, Brace CS, et al. Circadian clock feedback cycle through NAMPT-mediated NAD+ biosynthesis. *Science.* 2009;324(5927):651-654.

34. Gonze D, Bernard S, Waltermann C, Kramer A, Herzel H. Spontaneous synchronization of coupled circadian oscillators. *Biophys J.* 2005;89(1):120-129.

35. Ramakrishnan R, DuBois DC, Almon RR, Pyszczynski NA, Jusko WJ. Fifth-generation model for corticosteroid pharmacodynamics: application to steady-state receptor down-regulation and enzyme induction patterns during seven-day continuous infusion of methylprednisolone in rats. *J Pharmacokinet Pharmacodyn.* 2002;29(1):1-24.

36. Pierre K, Schlesinger N, Androulakis IP. The role of the hypothalamic-pituitary-adrenal axis in modulating seasonal changes in immunity. *Physiol Genomics.* 2016:physiolgenomics 00006 02016.

37. Newman LA, Walker MT, Brown RL, Cronin TW, Robinson PR. Melanopsin forms a functional short-wavelength photopigment. *Biochemistry.* 2003;42(44):12734-12738.

38. Dibner C, Schibler U, Albrecht U. The mammalian circadian timing system: organization and coordination of central and peripheral clocks. *Annu Rev Physiol.* 2010;72:517-549.

39. Skene DJ, Lockley SW, James K, Arendt J. Correlation between urinary cortisol and 6-sulphatoxymelatonin rhythms in field studies of blind subjects. *Clin Endocrinol.* 1999;50(6):715-719.

40. Kow LM, Pfaff DW. Vasopressin Excites Ventromedial Hypothalamic Glucose-Responsive Neurons Invitro. *Physiology & Behavior.* 1986;37(1):153-158.

41. Kalsbeek A, vanderVliet J, Buijs RM. Decrease of endogenous vasopressin release necessary for expression of the circadian rise in plasma corticosterone: A reverse microdialysis study. *Journal of Neuroendocrinology.* 1996;8(4):299-307.

42. Mazzocchi G, Malendowicz LK, Rebuffat P, Tortorella C, Nussdorfer GG. Arginine-vasopressin stimulates CRH and ACTH release by rat adrenal medulla, acting via the V1 receptor subtype and a protein kinase C-dependent pathway. *Peptides.* 1997;18(2):191-195.

43. Aronsson M, Fuxe K, Dong Y, Agnati LF, Okret S, Gustafsson JA. Localization of glucocorticoid receptor mRNA in the male rat brain by in situ hybridization. *Proc Natl Acad Sci U S A.* 1988;85(23):9331-9335.

44. Guan XM, Yu H, Palyha OC, et al. Distribution of mRNA encoding the growth hormone secretagogue receptor in brain and peripheral tissues. *Brain Res Mol Brain Res.* 1997;48(1):23-29.

45. Schwartz MW, Seeley RJ, Campfield LA, Burn P, Baskin DG. Identification of targets of leptin action in rat hypothalamus. *J Clin Invest.* 1996;98(5):1101-1106.

46. Unger J, McNeill TH, Moxley RT, 3rd, White M, Moss A, Livingston JN. Distribution of insulin receptor-like immunoreactivity in the rat forebrain. *Neuroscience.* 1989;31(1):143-157.

47. Pinto S, Roseberry AG, Liu H, et al. Rapid rewiring of arcuate nucleus feeding circuits by leptin. *Science.* 2004;304(5667):110-115.

48. Spanswick D, Smith MA, Mirshamsi S, Routh VH, Ashford ML. Insulin activates ATP-sensitive K+ channels in hypothalamic neurons of lean, but not obese rats. *Nat Neurosci.* 2000;3(8):757-758.

49. van den Top M, Lee K, Whyment AD, Blanks AM, Spanswick D. Orexigen-sensitive NPY/AgRP pacemaker neurons in the hypothalamic arcuate nucleus. *Nat Neurosci.* 2004;7(5):493-494.

50. Yi CX, van der Vliet J, Dai J, Yin G, Ru L, Buijs RM. Ventromedial arcuate nucleus communicates peripheral metabolic information to the suprachiasmatic nucleus. *Endocrinology.* 2006;147(1):283-294.

51. Angeles-Castellanos M, Salgado-Delgado R, Rodriguez K, Buijs RM, Escobar C. The Suprachiasmatic Nucleus Participates in Food Entrainment: A Lesion Study. *Neuroscience.* 2010;165(4):1115-1126.

52. Wust S, Wolf J, Hellhammer DH, Federenko I, Schommer N, Kirschbaum C. The cortisol awakening response - normal values and confounds. *Noise Health.* 2000;2(7):79-88.

53. Hara R, Wan K, Wakamatsu H, et al. Restricted feeding entrains liver clock without participation of the suprachiasmatic nucleus. *Genes to Cells.* 2001;6:269-278.

54. Petrovsky N, McNair P, Harrison LC. Diurnal rhythms of pro-inflammatory cytokines: regulation by plasma cortisol and therapeutic implications. *Cytokine.* 1998;10(4):307-312.

55. Racanelli V, Rehermann B. The liver as an immunological organ. *Hepatology.* 2006;43(2):S54-S62.

56. Rowell DL, Eckmann L, Dwinell MB, et al. Human hepatocytes express an array of proinflammatory cytokines after agonist stimulation or bacterial invasion. *Am J Physiol-Gastr L.* 1997;273(2):G322-G332.

57. Cermakian N, Lange T, Golombek D, et al. Crosstalk between the circadian clock circuitry and the immune system. *Chronobiology International.* 2013;30(7):870-888.

58. Leonard BE. HPA and immune axes in stress: involvement of the serotonergic system. *Neuroimmunomodulation.* 2006;13(5-6):268-276.

59. Knudsen PJ, Dinarello CA, Strom TB. Glucocorticoids inhibit transcriptional and post-transcriptional expression of interleukin 1 in U937 cells. *J Immunol.* 1987;139(12):4129-4134.

60. Kutteh WH, Rainey WE, Carr BR. Glucocorticoids inhibit lipopolysaccharide-induced production of tumor necrosis factor-alpha by human fetal Kupffer cells. *J Clin Endocrinol Metab.* 1991;73(2):296-301.

61. Amano Y, Lee SW, Allison AC. Inhibition by glucocorticoids of the formation of interleukin-1 alpha, interleukin-1 beta, and interleukin-6: mediation by decreased mRNA stability. *Mol Pharmacol.* 1993;43(2):176-182.

62. Paliogianni F, Boumpas DT. Glucocorticoids regulate calcineurin-dependent trans-activating pathways for interleukin-2 gene transcription in human T lymphocytes. *Transplantation.* 1995;59(9):1333-1339.

63. Curtis AM, Fagundes CT, Yang G, et al. Circadian control of innate immunity in macrophages by miR-155 targeting Bmal1. *Proc Natl Acad Sci U S A.* 2015;112(23):7231-7236.

64. Gibbs JE, Blaikley J, Beesley S, et al. The nuclear receptor REV-ERBalpha mediates circadian regulation of innate immunity through selective regulation of inflammatory cytokines. *Proc Natl Acad Sci U S A.* 2012;109(2):582-587.

65. Nguyen KD, Fentress SJ, Qiu Y, Yun K, Cox JS, Chawla A. Circadian gene Bmal1 regulates diurnal oscillations of Ly6C(hi) inflammatory monocytes. *Science.* 2013;341(6153):1483-1488.

66. Akira S, Hirano T, Taga T, Kishimoto T. Biology of multifunctional cytokines: IL 6 and related molecules (IL 1 and TNF). *FASEB J.* 1990;4(11):2860-2867.

67. Hipkiss AR. Energy metabolism, altered proteins, sirtuins and ageing: converging mechanisms? *Biogerontology.* 2008;9(1):49-55.

68. Ramsey KM, J. Y, C.S. B, et al. Circadian Clock Feedback Cycle Through NAMPT-Mediated NAD+ Biosynthesis. *SCIENCE.* 2009;324:651-654.

69. Bellet MM, Nakahata Y, Boudjelal M, et al. Pharmacological modulation of circadian rhythms by synthetic activators of the deacetylase SIRT1. *Proc Natl Acad Sci U S A.* 2013;110(9):3333-3338.

70. Zhao X, Allison D, Condon B, et al. The 2.5 A crystal structure of the SIRT1 catalytic domain bound to nicotinamide adenine dinucleotide (NAD+) and an indole (EX527 analogue) reveals a novel mechanism of histone deacetylase inhibition. *J Med Chem.* 2013;56(3):963-969.

71. Cao D, Wang M, Qiu X, et al. Structural basis for allosteric, substrate-dependent stimulation of SIRT1 activity by resveratrol. *Genes Dev.* 2015;29(12):1316-1325.

72. Napper AD, Hixon J, McDonagh T, et al. Discovery of indoles as potent and selective inhibitors of the deacetylase SIRT1. *J Med Chem.* 2005;48(25):8045-8054.

73. Alcain FJ, Villalba JM. Sirtuin activators. *Expert Opin Ther Pat.* 2009;19(4):403-414.

74. Villalba JM, Alcain FJ. Sirtuin activators and inhibitors. *Biofactors.* 2012;38(5):349-359.

75. Tareen SH, Ahmad J. Modelling and analysis of the feeding regimen induced entrainment of hepatocyte circadian oscillators using petri nets. *PLoS One.* 2015;10(3):e0117519.

76. Yamamoto T, Nakahata Y, Tanaka M, et al. Acute physical stress elevates mouse period1 mRNA expression in mouse peripheral tissues via a glucocorticoid-responsive element. *J Biol Chem.* 2005;280(51):42036-42043.

77. Motzkus D, Albrecht U, Maronde E. The human PER1 gene is inducible by interleukin-6. *J Mol Neurosci.* 2002;18(1-2):105-109.

78. Perez-Aso M, Feig JL, Mediero A, Cronstein BN. Adenosine A2A receptor and TNF-alpha regulate the circadian machinery of the human monocytic THP-1 cells. *Inflammation.* 2013;36(1):152-162.

79. Yoshida K, Hashiramoto A, Okano T, Yamane T, Shibanuma N, Shiozawa S. TNF-alpha modulates expression of the circadian clock gene Per2 in rheumatoid synovial cells. *Scand J Rheumatol.* 2013;42(4):276-280.

80. Duez H, Staels B. Rev-erb-alpha: an integrator of circadian rhythms and metabolism. *J Appl Physiol (1985).* 2009;107(6):1972-1980.

81. Eckel-Mahan K, Sassone-Corsi P. Metabolism and the circadian clock converge. *Physiol Rev.* 2013;93(1):107-135.

82. Asher G, Schibler U. Crosstalk between components of circadian and metabolic cycles in mammals. *Cell Metab.* 2011;13(2):125-137.

83. Asher G, Gatfield D, Stratmann M, et al. SIRT1 regulates circadian clock gene expression through PER2 deacetylation. *Cell.* 2008;134(2):317-328.

84. Fries E, Dettenborn L, Kirschbaum C. The cortisol awakening response (CAR): facts and future directions. *Int J Psychophysiol.* 2009;72(1):67-73.

85. von Schantz M, Archer SN. Clocks, genes and sleep. *J R Soc Med.* 2003;96(10):486-489.

86. Hara R, Wan K, Wakamatsu H, et al. Restricted feeding entrains liver clock without participation of the suprachiasmatic nucleus. *Genes Cells.* 2001;6(3):269-278.

87. Filipski E, Innominato PF, Wu M, et al. Effects of light and food schedules on liver and tumor molecular clocks in mice. *J Natl Cancer Inst.* 2005;97(7):507-517.

88. Sudo M, Sasahara K, Moriya T, Akiyama M, Hamada T, Shibata S. Constant light housing attenuates circadian rhythms of mPer2 mRNA and mPER2 protein expression in the suprachiasmatic nucleus of mice. *Neuroscience.* 2003;121(2):493-499.

89. Tzamaloukas AH, Ing TS, Siamopoulos KC, et al. Pathophysiology and management of fluid and electrolyte disturbances in patients on chronic dialysis with severe hyperglycemia. *Semin Dial.* 2008;21(5):431-439.

90. Yang X, Downes M, Yu RT, et al. Nuclear receptor expression links the circadian clock to metabolism. *Cell.* 2006;126(4):801-810.

91. Lau P, Nixon SJ, Parton RG, Muscat GE. RORalpha regulates the expression of genes involved in lipid homeostasis in skeletal muscle cells: caveolin-3 and CPT-1 are direct targets of ROR. *J Biol Chem.* 2004;279(35):36828-36840.

92. Laposky AD, Shelton J, Bass J, Dugovic C, Perrino N, Turek FW. Altered sleep regulation in leptin-deficient mice. *Am J Physiol Regul Integr Comp Physiol.* 2006;290(4):R894-903.

93. Li XM, Delaunay F, Dulong S, et al. Cancer inhibition through circadian reprogramming of tumor transcriptome with meal timing. *Cancer Res.* 2010;70(8):3351-3360.

94. Ogawa A, Yano M, Tsujinaka T, et al. Modulation of circadian expression of D-site binding protein by the schedule of parenteral nutrition in rat liver. *Hepatology.* 1997;26(6):1580-1586.

95. Le Minh N, Damiola F, Tronche F, Schütz G, Schibler U. Glucocorticoid hormones inhibit food-induced phase-shifting of peripheral circadian oscillators. *The EMBO Journal.* 2001;20(24):7128-7136.

96. Hatori M, Vollmers C, Zarrinpar A, et al. Time-restricted feeding without reducing caloric intake prevents metabolic diseases in mice fed a high-fat diet. *Cell Metab.* 2012;15:848-860.

97. Resmi V, Ambika G, Amritkar RE. General mechanism for amplitude death in coupled systems. *Phys Rev E Stat Nonlin Soft Matter Phys.* 2011;84(4 Pt 2):046212.

98. Garaulet M, G??mez-Abell??n Pn. Timing of food intake and obesity: a novel association. *Physiology & behavior.* 2014;134:44-50.

99. Oda GA, Friesen WO. Modeling two-oscillator circadian systems entrained by two environmental cycles. *PLoS One.* 2011;6(8):e23895.

100. Fang M, Guo WR, Park Y, Kang HG, Zarbl H. Enhancement of NAD(+)-dependent SIRT1 deacetylase activity by methylselenocysteine resets the circadian clock in carcinogen-treated mammary epithelial cells. *Oncotarget.* 2015;6(40):42879-42891.

101. Lardone PJ, Alvarez-Sanchez SN, Guerrero JM, Carrillo-Vico A. Melatonin and glucose metabolism: clinical relevance. *Curr Pharm Des.* 2014;20(30):4841-4853.

102. Perez-Mendoza M, Rivera-Zavala JB, Diaz-Munoz M. Daytime restricted feeding modifies the daily variations of liver gluconeogenesis: adaptations in biochemical and endocrine regulators. *Chronobiol Int.* 2014;31(7):815-828.

103. Coufalik AH, Monder C. Stimulation of gluconeogenesis by cortisol in fetal rat liver in organ culture. *Endocrinology.* 1981;108(4):1132-1137.

104. Bae S-A, Androulakis IP. The Synergistic Role of Light-Feeding Phase Relations on Entraining Robust Circadian Rhythms in the Periphery. *Gene Regulation and Systems Biology.* 2017;2017(11):0-0.

105. Rao R, DuBois D, Almon R, Jusko WJ, Androulakis IP. Mathematical modeling of the circadian dynamics of the neuroendocrine-immune network in experimentally induced arthritis. *Am J Physiol Endocrinol Metab.* 2016;311(2):E310-324.

106. Bordone L, Guarente L. Calorie restriction, SIRT1 and metabolism: understanding longevity. *Nat Rev Mol Cell Biol.* 2005;6(4):298-305.

107. Puigserver P, Spiegelman BM. Peroxisome proliferator-activated receptor-gamma coactivator 1 alpha (PGC-1 alpha): transcriptional coactivator and metabolic regulator. *Endocr Rev.* 2003;24(1):78-90.

108. Puigserver P, Rhee J, Lin J, et al. Cytokine stimulation of energy expenditure through p38 MAP kinase activation of PPARgamma coactivator-1. *Mol Cell.* 2001;8(5):971-982.

109. Randle PJ, Priestman DA, Mistry SC, Halsall A. Glucose fatty acid interactions and the regulation of glucose disposal. *J Cell Biochem.* 1994;55 Suppl:1-11.

110. Herzig S, Long F, Jhala US, et al. CREB regulates hepatic gluconeogenesis through the coactivator PGC-1. *Nature.* 2001;413(6852):179-183.

111. Yabaluri N, Bashyam MD. Hormonal regulation of gluconeogenic gene transcription in the liver. *J Biosci.* 2010;35(3):473-484.

112. Puigserver P, Rhee J, Donovan J, et al. Insulin-regulated hepatic gluconeogenesis through FOXO1-PGC-1alpha interaction. *Nature.* 2003;423(6939):550-555.

113. Campolongo F, Saltelli A, Cariboni J. From screening to quantitative sensitivity analysis. A unified approach. *Comput Phys Commun.* 2011;182(4):978-988.

114. Morris MD. Factorial Sampling Plans for Preliminary Computational Experiments. *Technometrics.* 1991;33(2):161-174.

115. Campolongo F, Cariboni J, Saltelli A. An effective screening design for sensitivity analysis of large models. *Environ Modell Softw.* 2007;22(10):1509-1518.

116. Sobol' IyM. On the distribution of points in a cube and the approximate evaluation of integrals. *Zhurnal Vychislitel'noi Matematiki i Matematicheskoi Fiziki.* 1967;7(4):784-802.

117. Sobol IM. Uniformly distributed sequences with an additional uniform property. *USSR Computational Mathematics and Mathematical Physics.* 1976;16(5):236-242.

118. Rabitz H, Alis OF, Shorter J, Shim K. Efficient input-output model representations. *Comput Phys Commun.* 1999;117(1-2):11-20.

119. Li GY, Wang SW, Rabitz H, Wang SY, Jaffe P. Global uncertainty assessments by high dimensional model representations (HDMR). *Chem Eng Sci.* 2002;57(21):4445-4460.

120. Li GY, Wang SW, Rabitz H. Practical approaches to construct RS-HDMR component functions. *Journal of Physical Chemistry A.* 2002;106(37):8721-8733.

121. Stephan FK. The "other" circadian system: food as a Zeitgeber. *J Biol Rhythms.* 2002;17(4):284-292.

122. Nakahata Y, Kaluzova M, Grimaldi B, et al. The NAD+-dependent deacetylase SIRT1 modulates CLOCK-mediated chromatin remodeling and circadian control. *Cell.* 2008;134(2):329-340.

123. Ashman PU, Seed JR. Biochemical studies in the vole, Microtus montanus. II. The effects of a Trypanosoma brucei gambiense infection on the diurnal variation of hepatic glucose-6-phosphatase and liver glycogen. *Comp Biochem Physiol B.* 1973;45(2):379-392.

124. Oishi K, Atsumi G, Sugiyama S, et al. Disrupted fat absorption attenuates obesity induced by a high-fat diet in Clock mutant mice. *Febs Letters.* 2006;580(1):127-130.

125. Rudic RD, McNamara P, Curtis AM, et al. BMAL1 and CLOCK, two essential components of the circadian clock, are involved in glucose homeostasis. *Plos Biol.* 2004;2(11):1893-1899.

126. Turek FW, Joshu C, Kohsaka A, et al. Obesity and metabolic syndrome in circadian Clock mutant mice. *Science.* 2005;308(5724):1043-1045.

127. Marcheva B, Ramsey KM, Buhr ED, et al. Disruption of the clock components CLOCK and BMAL1 leads to hypoinsulinaemia and diabetes. *Nature.* 2010;466(7306):627-631.

128. Peschke E, Peschke D. Evidence for a circadian rhythm of insulin release from perifused rat pancreatic islets. *Diabetologia.* 1998;41(9):1085-1092.

129. Boden G, Ruiz J, Urbain JL, Chen X. Evidence for a circadian rhythm of insulin secretion. *Am J Physiol.* 1996;271(2 Pt 1):E246-252.

130. Daitoku H, Yamagata K, Matsuzaki H, Hatta M, Fukamizu A. Regulation of PGC-1 promoter activity by protein kinase B and the forkhead transcription factor FKHR. *Diabetes.* 2003;52(3):642-649.

131. Dang F, Sun X, Ma X, et al. Insulin post-transcriptionally modulates Bmal1 protein to affect the hepatic circadian clock. *Nat Commun.* 2016;7:12696.

132. Sadacca LA, Lamia KA, deLemos AS, Blum B, Weitz CJ. An intrinsic circadian clock of the pancreas is required for normal insulin release and glucose homeostasis in mice. *Diabetologia.* 2011;54(1):120-124.

133. Saini C, Petrenko V, Pulimeno P, et al. A functional circadian clock is required for proper insulin secretion by human pancreatic islet cells. *Diabetes Obes Metab.* 2016;18(4):355-365.

134. Maechler P, Wollheim CB. Mitochondrial signals in glucose-stimulated insulin secretion in the beta cell. *J Physiol.* 2000;529 Pt 1:49-56.

135. Henquin JC. Triggering and amplifying pathways of regulation of insulin secretion by glucose. *Diabetes.* 2000;49(11):1751-1760.

136. Bertuzzi A, Salinari S, Mingrone G. Insulin granule trafficking in beta-cells: mathematical model of glucose-induced insulin secretion. *Am J Physiol Endocrinol Metab.* 2007;293(1):E396-409.

137. Freckmann G, Hagenlocher S, Baumstark A, et al. Continuous glucose profiles in healthy subjects under everyday life conditions and after different meals. *J Diabetes Sci Technol.* 2007;1(5):695-703.

138. Saad A, Dalla Man C, Nandy DK, et al. Diurnal pattern to insulin secretion and insulin action in healthy individuals. *Diabetes.* 2012;61(11):2691-2700.

139. Van Cauter E, Shapiro ET, Tillil H, Polonsky KS. Circadian modulation of glucose and insulin responses to meals: relationship to cortisol rhythm. *Am J Physiol.* 1992;262(4 Pt 1):E467-475.

140. Qian J, Block GD, Colwell CS, Matveyenko AV. Consequences of exposure to light at night on the pancreatic islet circadian clock and function in rats. *Diabetes.* 2013;62(10):3469-3478.

141. Coomans CP, van den Berg SA, Houben T, et al. Detrimental effects of constant light exposure and high-fat diet on circadian energy metabolism and insulin sensitivity. *FASEB J.* 2013;27(4):1721-1732.

142. Becker-Weimann S, Wolf J, Herzel H, Kramer A. Modeling feedback loops of the Mammalian circadian oscillator. *Biophys J.* 2004;87(5):3023-3034.

Appendix

Table A1

#	Parameter	Value	Units	Description/Reference
1	k_{p1}	0.7965	$\mu M.h^{-1}$	Rate constant of CRH production[18]
2	K_{p1}	1.0577	μM	Dissociation constant for CRH production[18]
3	V_{d1}	0.5084	$\mu M.h^{-1}$	Rate of CRH enzymatic degradation[18]
4	K_{d1}	1.9627	μM	Michaelis constant of CRH enzymatic degradation[18]
5	k_{fp}	0.15	μM^{-1}	Efficiency of P on ACTH and F stimulation/ estimated[36]
6	k_{p2}	0.6857	$\mu M.h^{-1}$	Rate of ACTH production[18]
7	K_{p2}	1.0577	μM	Dissociation constant for ACTH production[18]
8	V_{d2}	0.5129	$\mu M.h^{-1}$	Rate of ACTH enzymatic degradation[18]
9	K_{d2}	0.3069	μM	Michaelis constant of ACTH enzymatic degradation[18]
10	k_{p3}	1.0302	$\mu M.h^{-1}$	Rate of F central production/ estimated[36]
11	k_n	1.2		Coupling constant of cortisol to cellular energy state
12	V_{d3}	0.3618	$\mu M.h^{-1}$	Rate of F central enzymatic degradation[18]
13	K_{d3}	0.4695	μM	Michaelis constant of F central enzymatic degradation[18]
14	$k_{syn_{Rm}}$	2.9	$fmol.g^{-1}.h^{-1}$	Synthesis rate or glucocorticoid receptor mRNA[35]
15	$I_{C50_{Rm}}$	26.2	$nmol.L^{-1}.mgprotein^{-1}$	Concentration of FR(N) at which mRNA, Rsynthesis drops to its half[35]
	R_0	540.7	$nmol.L^{-1}.mgprotein^{-1}$	Baseline value of free cytosolic glucocorticoid receptor[35]
	R_{m0}	25.8	$fmol.g^{-1}$	Baseline value of glucocorticoid receptor mRNA[35]

16	$k_{dgr_{Rm}}$	$k_{syn_{Rm}}/R_{m0}$		Degradation rate of glucocorticoid receptor mRNA[35]
17	k_{syn_R}	$(R_0/R_{m0})*k_{dgr_R}$		Synthesis rate of free cytosolic receptor[35]
18	r_f	0.49		Fraction of cortisol recycled[35]
19	k_{re}	0.57	h^{-1}	Rate of receptor recycling from nucleus to cytoplasm[35]
20	k_{on}	0.00329	$L.nmol^{-1}.h^{-1}$	Second order rate constant of glucocorticoid receptor binding[35]
21	k_{dgr_R}	0.0572	h^{-1}	Degradation rate of cytosolic glucocorticoid receptor[35]
22	k_t	0.63	h^{-1}	Rate of receptor translocation to the nucleus[35]
23	τ	0.25	h	Delay in Cortisol production following ACTH stimulation
24	k_{MR}	0.34	$nM.h^{-1}$	Base transcription rate of MR[32]
25	$k_{F,MR}$	1.1011	1	Maximum extent of $F_{periphery}$ mediated activation of MR[32]
26	$K_{F,MR}$	0.5	nM	Michaelis constant for $F_{periphery}$ mediated activation of MR[32]
27	MR_T	1.45	nM	Total MR concentration[32]
28	K_{MR}	0.21	nM	Michaelis constant for MR production[32]
29	$k_{MR,deg}$	0.70	$nM.h^{-1}$	Degradation rate for MR[32]
30	$K_{MR,deg}$	1.65	nM	Michaelis constant for degradation of MR[32]
31	$k_{b,MR}$	0.00329	$nM^{-1}.h^{-1}$	Degradation rate for cortisol/mineralocorticoid receptor binding[35]
32	$k_{on,MR}$	1	$L.nmol^{-1}.h^{-1}$	Second order rate constant of mineralocorticoid and receptor binding[32]
33	$k_{t,MR}$	1	h^{-1}	Rate of mineralocorticoid receptor translocation to the nucleus/[35]

34	$k_{re,MR}$	1	h^{-1}	Rate of mineralocorticoid receptor recycling from nucleus to cytoplasm[32]
35	k_{GR}	1.18	$nM.h^{-1}$	Base transcription rate of GR[32]
36	$k_{F,GR}$	15	1	Maximum extent of $F_{periphery}$ mediated activation of GR[32]
37	$K_{F,GR}$	30	nM	Michaelis constant for $F_{periphery}$ mediated activation of GR[32]
38	GR_T	1.81	nM	Total GR concentration[32]
39	K_{GR}	0.74	nM	Michaelis constant for GR production[32]
40	$k_{GR,deg}$	1.52	$nM.h^{-1}$	Degradation rate for GR[32]
41	$K_{GR,deg}$	1.05	nM	Michaelis constant for degradation of GR[32]
42	$k_{b,GR}$	0.00329	$nM^{-1}.h^{-1}$	Degradation rate for cortisol/glucocorticoid receptor binding[35]
43	$k_{on,GR}$	1	$L.nmol^{-1}.h^{-1}$	Second order rate constant of mineralocorticoid and receptor binding[35]
44	$k_{t,GR}$	1	h^{-1}	Rate of mineralocorticoid receptor translocation to the nucleus[35]
45	$k_{re,GR}$	1	h^{-1}	Rate of mineralocorticoid receptor recycling from nucleus to cytoplasm[35]
46	$k_{mRNA_{R_{pin}}}$	0.61	$\mu M.h^{-1}$	Base transcription rate of $mRNAR_P$[32]
47	k_{fr2}	0.8	1	Maximum extent of FMR(N) mediated transcription of $mRNAR_P$[32]
48	K_{fr2}	0.5	µM	Michaelis constant for FMR(N) mediated transcription of $mRNAR_P$[32]
49	k_{pc}	0.3	1	Maximum extent of BMAL1 mediated suppression of $mRNA_P$ and $mRNA_{TLR4}$ estimated

50	K_{pc}	25	µM	Michaelis constant for BMAL1 mediated suppression of $mRNA_P$ and $mRNA_{TLR4}$ estimated
51	$k_{mRNA_{Rpout}}$	0.19	h^{-1}	Degradation rate of $mRNAR_P$[32]
52	k_{in_P}	0.29	h^{-1}	Translation rate of P[32]
53	k_{out_P}	1.06	h^{-1}	Degradation rate of P[32]
54	$k_{mRNA_{Rpin}}$	0.61	$\mu M.h^{-1}$	Base transcription rate of $mRNAR_P$[32]
55	k_{fr2}	0.8	1	Maximum extent of FMR(N) mediated transcription of $mRNAR_P$[32]
56	$k_{mRNA_{Rpout}}$	0.19	h^{-1}	Degradation rate of $mRNAR_P$[32]
57	$k_{in_{R_p}}$	1.11	h^{-1}	Translation rate of R_P[32]
58	k_d	0.14	$\mu M^{-1}.h^{-1}$	$P–R_p$ binding rate constant[32]
59	$k_{out_{R_p}}$	0.26	h^{-1}	Degradation rate of R_P[32]
60	$k_{out_{PR_p}}$	1.3	h^{-1}	Dissociation rate of PR_P[32]
61	v_{1b}	9	$nM.h^{-1}$	Maximal rate of Per-Cry transcription[142]
62	k_{1b}	1	nM	Michaelis constant of Per-Cry transcription[142]
63	k_{1i}	0.56	nM	Inhibition constant of Per-Cry transcription[142]
64	c	0.01	nM	Concentration of constitutive activator[142]
65	p	8		Hill coefficient of inhibition of Per-Cry transcription[142]
66	k_f	1.2	nM^{-1}	Efficiency of P on transcription of Per-Cry/estimated[36]
67	k_c	0.009	$nM.h^{-1}$	Coupling strength/estimated
68	k_{1d}	0.12	h^{-1}	Degradation rate of Per-Cry mRNA[142]
69	k_{2b}	0.3	$nM^{-1}.h^{-1}$	Complex formation rate of Per-Cry mRNA[142]
70	q	2		No. of PER-CRY complex forming subunits[142]
71	k_{2d}	0.05	h^{-1}	Degradation rate of cytoplasmatic PER-CRY[142]

72	k_{2t}	0.24	h^{-1}	Nuclear import rate of the PER-CRY complex
73	k_{3t}	0.02	h^{-1}	Nuclear export rate of PER-CRY complex
74	k_{3d}	0.02	h^{-1}	Degradation rate of the nuclear PER-CRY complex
75	v_{4b}	3.6	$nM.h^{-1}$	Maximal rate of Bmal1 transcription[142]
76	k_{4b}	2.16	nM	Michaelis constant of Bmal1 transcription[142]
77	r	3		Hill coefficient of activation of Bmal1 transcription[142]
78	k_{4d}	0.75	h^{-1}	Degradation rate of Bmal1 mRNA[142]
79	k_{5b}	0.24	h^{-1}	Translation rate of BMAL1[142]
80	k_{5d}	0.06	h^{-1}	Degradation rate of cytoplasmatic BMAL1[142]
81	k_{5t}	0.45	h^{-1}	Nuclear import rate of BMAL1[142]
82	k_{6t}	0.06	h^{-1}	Nuclear export rate of BMAL1[142]
83	k_{6d}	0.12	h^{-1}	Degradation rate of nuclear BMAL1[142]
84	k_{6a}	1	h^{-1}	Activation rate of nuclear CLOCK-BMAL1
85	k_{7a}	0.1	h^{-1}	Deactivation rate of CLOCK-BMAL1
86	k_{7d}	0.5	h^{-1}	Degradation rate of CLOCK-BMAL1
87	k_{m8a}	10	h^{-1}	Association rate of CLOCK-BMAL1-SIRT1
88	k_{m8d}	20	h^{-1}	Dissociation rate of CLOCK-BMAL1-SIRT1
89	τ_f	3	h	Delay between feeding and NAD^+ reduction to NADH
90	k_{m1}	5	1	Maximum extent of NADH converting to NAD^+
91	K_{m1}	2	μM	Michaelis constant for NADH converting to NAD^+
92	k_{m2}	40	1	Maximum extent of NMN converting to NAD^+

93	K_{m2}	1	μM	Michaelis constant for NMN converting to NAD^+
94	k_{m3}	5	1	Maximum extent of NAD^+ converting to NADH upon feeding
95	K_{m3}	1	μM	Michaelis constant NAD^+ converting to NADH upon feeding
96	k_{m4}	20	1	Maximum extent of NAD^+ converting to NAM
97	K_{m4}	20	μM	Michaelis constant for NAD^+ converting to NAM
98	k_{m5}	40	1	Maximum extent of NAM converting to NMN, mediated by NAMPT
99	K_{m5}	5	μM	Michaelis constant for of NAM converting to NMN, mediated by NAMPT
100	k_{m11}	5	1	Maximum extent of entrainment of cortisol by feeding
101	K_{m11}	2	μM	Michaelis constant for entrainment of cortisol by feeding
102	k_{m12}	1	μMh^{-1}	Rate of cortisol entraining signal degradation
103	k_{m6}	5	1	Maximum extent of SIRT1 activation mediated by NAD
104	K_{m6}	1	μM	Michaelis constant of SIRT1 activation mediated by NAD
105	sirtT	5	μM	Sum of active and inactive SIRT1
106	k_{m7}	2	1	Maximum extent of SIRT1 degradation
107	K_{m7}	1	μM	Michaelis constant for SIRT1 degradation
108	k_{m8a}	10	$\mu M^{-2}h^{-1}$	Rate of SIRT1 and CLOCK/BMAL1 complex association
109	k_{m8d}	20	$\mu M^{-1}h^{-1}$	Rate of SIRT1 and CLOCK/BMAL1 complex dissociation
110	k_{m9d}	0.1	$\mu M^{-1}h^{-1}$	Rate of CLOCK/BMAL1/SIRT1 complex degradation
111	k_{m10a}	2	μMh^{-1}	Rate of NAMPT production mediated by

				CLOCK/BMAL1/SIRT1 complex
112	k_{m10d}	2	h^{-1}	Rate of NAMPT degradation
113	nad	1	µM	Sum of NAD^+ and NADH

Table A2

#	Parameter	Value	Units	Description/Reference
1	k_{p1}	0.7965	$\mu M.h^{-1}$	Rate constant of CRH production[18]
2	K_{p1}	1.0577	µM	Dissociation constant for CRH production[18]
3	V_{d1}	0.5084	$\mu M.h^{-1}$	Rate of CRH enzymatic degradation[18]
4	K_{d1}	1.9627	µM	Michaelis constant of CRH enzymatic degradation[18]
5	k_{fp}	0.1	μM^{-1}	Efficiency of P on ACTH and F stimulation/ estimated
6	k_{p2}	0.4	$\mu M.h^{-1}$	Rate of ACTH production
7	K_{p2}	1.0577	µM	Dissociation constant for ACTH production[18]
8	V_{d2}	0.5129	$\mu M.h^{-1}$	Rate of ACTH enzymatic degradation[18]
9	K_{d2}	0.3069	µM	Michaelis constant of ACTH enzymatic degradation[18]
10	k_{p3}	0.15	$\mu M.h^{-1}$	Rate of F central production/ estimated[36]
11	k_n	1.5		Coupling constant of cortisol to cellular energy state
12	V_{d3}	3.4	$\mu M.h^{-1}$	Rate of F central enzymatic degradation

13	K_{d3}	0.4695	µM	Michaelis constant of F central enzymatic degradation[18]
14	$k_{syn_{Rm}}$	2.9	$fmol.g^{-1}.h^{-1}$	Synthesis rate or glucocorticoid receptor mRNA[35]
15	$I_{C50_{Rm}}$	26.2	$nmol.L^{-1}.mgprotein^{-1}$	Concentration of FR(N) at which mRNA, Rsynthesis drops to its half[35]
	R_0	540.7	$nmol.L^{-1}.mgprotein^{-1}$	Baseline value of free cytosolic glucocorticoid receptor[35]
	R_{m0}	25.8	$fmol.g^{-1}$	Baseline value of glucocorticoid receptor mRNA[35]
16	$k_{dgr_{Rm}}$	$k_{syn_{Rm}}/R_{m0}$		Degradation rate of glucocorticoid receptor mRNA[35]
17	k_{syn_R}	$(R_0/R_{m0})*k_{dgr_R}$		Synthesis rate of free cytosolic receptor[35]
18	r_f	0.49		Fraction of cortisol recycled[35]
19	k_{re}	0.57	h^{-1}	Rate of receptor recycling from nucleus to cytoplasm[35]
20	k_{on}	0.00329	$L.nmol^{-1}.h^{-1}$	Second order rate constant of glucocorticoid receptor binding[35]
21	k_{dgr_R}	0.0572	h^{-1}	Degradation rate of cytosolic glucocorticoid receptor[35]
22	k_t	0.63	h^{-1}	Rate of receptor translocation to the nucleus[35]
23	τ	0.25	h	Delay in Cortisol production following ACTH stimulation
24	k_{MR}	0.34	$nM.h^{-1}$	Base transcription rate of MR[32]

25	$k_{F,MR}$	1.1011	1	Maximum extent of $F_{periphery}$ mediated activation of MR[32]
26	$K_{F,MR}$	0.5	nM	Michaelis constant for $F_{periphery}$ mediated activation of MR[32]
27	MR_T	1.45	nM	Total MR concentration[32]
28	K_{MR}	0.21	nM	Michaelis constant for MR production[32]
29	$k_{MR,deg}$	0.70	$nM.h^{-1}$	Degradation rate for MR[32]
30	$K_{MR,deg}$	1.65	nM	Michaelis constant for degradation of MR[32]
31	$k_{b,MR}$	0.00329	$nM^{-1}.h^{-1}$	Degradation rate for cortisol/mineralocorticoid receptor binding[35]
32	$k_{r,MR}$	0.001		
33	$k_{on,MR}$	1	$L.nmol^{-1}.h^{-1}$	Second order rate constant of mineralocorticoid and receptor binding[32]
34	$k_{t,MR}$	1	h^{-1}	Rate of mineralocorticoid receptor translocation to the nucleus/[35]
35	$k_{re,MR}$	1	h^{-1}	Rate of mineralocorticoid receptor recycling from nucleus to cytoplasm[32]
36	k_{GR}	1.18	$nM.h^{-1}$	Base transcription rate of GR[32]
37	$k_{F,GR}$	15	1	Maximum extent of $F_{periphery}$ mediated activation of GR[32]
38	$K_{F,GR}$	30	nM	Michaelis constant for $F_{periphery}$ mediated activation of GR[32]

39	GR_T	1.81	nM	Total GR concentration[32]
40	K_{GR}	0.74	nM	Michaelis constant for GR production[32]
41	$k_{GR,deg}$	1.52	$nM.h^{-1}$	Degradation rate for GR[32]
42	$K_{GR,deg}$	1.05	nM	Michaelis constant for degradation of GR[32]
43	$k_{b,GR}$	0.00329	$nM^{-1}.h^{-1}$	Degradation rate for cortisol/glucocorticoid receptor binding[35]
44	$kr_{,GR}$	0.001		
45	$k_{on,GR}$	1	$L.nmol^{-1}.h^{-1}$	Second order rate constant of mineralocorticoid and receptor binding[35]
46	$k_{t,GR}$	1	h^{-1}	Rate of mineralocorticoid receptor translocation to the nucleus[35]
47	$k_{re,GR}$	1	h^{-1}	Rate of mineralocorticoid receptor recycling from nucleus to cytoplasm[35]
48	$k_{mRNA_{R_{pin}}}$	0.61	$\mu M.h^{-1}$	Base transcription rate of $mRNAR_P$[32]
49	k_{fr}	1.07	1	Maximum extent of FMR(N) mediated transcription of $mRNAR_P$[32]
50	K_{fr}	0.5	µM	Michaelis constant for FMR(N) mediated transcription of $mRNAR_P$[32]
51	k_{pc}	0.3	1	Maximum extent of BMAL1 mediated suppression of $mRNA_P$ and $mRNA_{TLR4}$ estimated
52	K_{pc}	25	µM	Michaelis constant for BMAL1 mediated suppression of

				$mRNA_P$ and $mRNA_{TLR4}$ estimated
53	$k_{mRNA_{Rpout}}$	0.19	h^{-1}	Degradation rate of $mRNAR_P$[32]
54	k_{in_P}	0.29	h^{-1}	Translation rate of P[32]
55	k_{out_P}	1.06	h^{-1}	Degradation rate of P[32]
56	$k_{mRNA_{Rpin}}$	0.61	$\mu M.h^{-1}$	Base transcription rate of $mRNAR_P$[32]
57	k_{fr2}	0.8	1	Maximum extent of FMR(N) mediated transcription of $mRNAR_P$[32]
58	K_{fr2}	0.5	μM	Michaelis constant for FMR(N) mediated suppression of $mRNAR_P$[32]
59	$k_{mRNA_{Rpout}}$	0.19	h^{-1}	Degradation rate of $mRNAR_P$[32]
60	$k_{in_{R_p}}$	1.11	h^{-1}	Translation rate of R_P[32]
61	k_d	0.14	$\mu M^{-1}.h^{-1}$	$P–R_p$ binding rate constant[32]
62	$k_{out_{R_p}}$	0.26	h^{-1}	Degradation rate of R_P[32]
63	$k_{out_{PR_p}}$	1.3	h^{-1}	Dissociation rate of PR_P[32]
64	v_{1b}	4	$nM.h^{-1}$	Maximal rate of Per-Cry transcription[142]
65	k_{1b}	1	nM	Michaelis constant of Per-Cry transcription[142]
66	k_{1i}	0.56	nM	Inhibition constant of Per-Cry transcription[142]
67	c	0.01	nM	Concentration of constitutive activator[142]
68	p	8		Hill coefficient of inhibition of Per-Cry transcription[142]

69	k_f	0.1	nM^{-1}	Efficiency of P on transcription of Per-Cry/estimated[36]
70	(ent)k_c	0.009	$nM.h^{-1}$	Coupling strength/estimated
71	k_{1d}	0.12	h^{-1}	Degradation rate of Per-Cry mRNA[142]
72	k_{2b}	0.3	$nM^{-1}.h^{-1}$	Complex formation rate of Per-Cry mRNA[142]
73	q	2		No. of PER-CRY complex forming subunits[142]
74	k_{2d}	0.05	h^{-1}	Degradation rate of cytoplasmatic PER-CRY[142]
75	k_{2t}	0.24	h^{-1}	Nuclear import rate of the PER-CRY complex
76	k_{3t}	0.02	h^{-1}	Nuclear export rate of PER-CRY complex
77	k_{3d}	0.02	h^{-1}	Degradation rate of the nuclear PER-CRY complex
78	v_{4b}	3.6	$nM.h^{-1}$	Maximal rate of Bmal1 transcription[142]
79	k_{4b}	2.16	nM	Michaelis constant of Bmal1 transcription[142]
80	r	3		Hill coefficient of activation of Bmal1 transcription[142]
81	k_{4d}	0.75	h^{-1}	Degradation rate of Bmal1 mRNA[142]
82	k_{5b}	0.24	h^{-1}	Translation rate of BMAL1[142]
83	k_{5d}	0.06	h^{-1}	Degradation rate of cytoplasmatic BMAL1[142]
84	k_{5t}	0.45	h^{-1}	Nuclear import rate of BMAL1[142]
85	k_{6t}	0.06	h^{-1}	Nuclear export rate of BMAL1[142]

86	k_{6d}	0.12	h^{-1}	Degradation rate of nuclear BMAL1[142]
87	k_{6a}	1	h^{-1}	Activation rate of nuclear CLOCK-BMAL1
88	k_{7a}	0.1	h^{-1}	Deactivation rate of CLOCK-BMAL1
89	k_{7d}	0.5	h^{-1}	Degradation rate of CLOCK-BMAL1
90	k_{m8a}	10	h^{-1}	Association rate of CLOCK-BMAL1-SIRT1
91	k_{m8d}	20	h^{-1}	Dissociation rate of CLOCK-BMAL1-SIRT1
92	τ_f	3	h	Delay between feeding and NAD^+ reduction to NADH
93	k_{m1}	5	1	Maximum extent of NADH converting to NAD^+
94	K_{m1}	2	μM	Michaelis constant for NADH converting to NAD^+
95	k_{m2}	40	1	Maximum extent of NMN converting to NAD^+
96	K_{m2}	1	μM	Michaelis constant for NMN converting to NAD^+
97	k_{m3}	5	1	Maximum extent of NAD^+ converting to NADH upon feeding
98	K_{m3}	1	μM	Michaelis constant NAD^+ converting to NADH upon feeding
99	k_{m4}	20	1	Maximum extent of NAD^+ converting to NAM

100	K_{m4}	20	μM	Michaelis constant for NAD^+ converting to NAM
101	k_{m5}	40	1	Maximum extent of NAM converting to NMN, mediated by NAMPT
102	K_{m5}	5	μM	Michaelis constant for of NAM converting to NMN, mediated by NAMPT
103	k_{m11}	5	1	Maximum extent of entrainment of cortisol by feeding
104	K_{m11}	2	μM	Michaelis constant for entrainment of cortisol by feeding
105	k_{m12}	1	μMh^{-1}	Rate of cortisol entraining signal degradation
106	k_{m6}	5	1	Maximum extent of SIRT1 activation mediated by NAD
107	K_{m6}	1	μM	Michaelis constant of SIRT1 activation mediated by NAD
108	sirtT	5	μM	Sum of active and inactive SIRT1
109	k_{m7}	2	1	Maximum extent of SIRT1 degradation
110	K_{m7}	1	μM	Michaelis constant for SIRT1 degradation
111	k_{m9d}	0.1	$\mu M^{-1}h^{-1}$	Rate of CLOCK/BMAL1/SIRT1 complex degradation
112	k_{m10a}	2	μMh^{-1}	Rate of NAMPT production mediated by CLOCK/BMAL1/SIRT1 complex
113	k_{m10d}	2	h^{-1}	Rate of NAMPT degradation
114	nad	1	μM	Sum of NAD^+ and NADH

115	k_{g1}	2	$nM.h^{-1}$	Rate of PGC-1α transcription
116	k_{g2}	2	$nM.h^{-1}$	Rate of PGC-1α mRNA degradation
117	k_{g3b}	3	h^{-1}	Rate of PGC-1α translation
118	k_{g3d}	3	h^{-1}	Rate of PGC-1α degradation
119	k_{g3t}	2	h^{-1}	Rate of PGC-1α nuclear import
120	k_{g4t}	2	h^{-1}	Rate of PGC-1α nuclear export
121	k_{g5}	0.1	h^{-1}	Rate of PGC-1α activation
122	k_{g7}	1	nM	Inhibition constant for binding of cortisol-receptor complex to GRE
123	k_{g8}	0.8	h^{-1}	Rate of active PGC-1α degradation
124	k_{g8d}	0.5	h^{-1}	Rate of deactivation of PGC-1α
125	k_{g9}	3	h^{-1}	Rate of FOXO1 activation
126	k_{g10}	5	h^{-1}	Rate of FOXO1 deactivation
127	k_{g11}	70	h^{-1}	Transcription rate of gluconeogenic genes
128	k_{g12}	3	h^{-1}	Degradation rate of gluconeogenic genes mRNA
129	k_{g13}	0.1	h^{-1}	Rate of Bmal1 transcription activation by active PGC-1α
130	s	8		Hill coefficient for inhibition of cortisol-receptor complex and GRE binding

Table A3

#	Parameter	Value	Units	Description/Reference
1	k	0.01	min^{-1}	Rate constant of formation of proinsulin-containing granules[136]
2	α_I	0.3	min^{-1}	Rate constant of degradation of proinsulin agreegates[136]
3	α_V	0.6	min^{-1}	Rate constant of degradation of granule membrane material[136]
4	σ	30	min^{-1}	Rate constant of insulin release from granules fused with cell membrane[136]
5	k_{Ib}	0.262		Constant describing the period of b_V[136]
6	k_{Ic}	10		Constant describing the period and horizontal shift of b_V[136]
7	k_{I1}	10	$nM^{-1}min^{-1}$	Activation rate for b_V
8	k_{I2}	9		Deactivation rate for b_V
9	k_{I3}	2.3	$(L/mmol)^3$	Parameter for b_I
10	k_{I4}	4	$(L/mmol)^3$	Parameter for b_I
11	k_{I5}	60	min^{-1}	Parameter for b_I
12	k_{In}	3		Hill coefficient for b_I
13	γ	1e-4	min^{-1}	Rate constant of granule extermalization and priming related to ATP/ADP[136]
14	k_1^+	5.788e-5	min^{-1}	Rate constant of association for the binding between granule and Ca^{2+} channel[136]
15	k_1^-	0.255	min^{-1}	Rate constant of dissociaton for the binding between granule and Ca^{2+} channel[136]

16	C_T	300		Constant pool of total Ca^{2+} channels[136]
17	τ_V	5	min	Time delay of recycling of granule membrane material[136]
18	η	4	min^{-1}	Rate constant for γ[136]
19	γ_b	1e-4	min^{-1}	Basal value of γ[136]
20	τ_G	1	hr^{-1}	Time delay for increase in glucose[136]
21	G*	4.58	mmol/L	Glucose concentration threshold for the activaton of γ[136]
22	$\hat{G}$	10	mmol/L	Glucose concentration over which h_γ remains constant and equal to $\hat{h}$[136]
23	$\hat{h}$	3.93e-3	min^{-1}	Maximal value of h_γ[136]
24	ζ	4	min^{-1}	Rate constant for ρ[136]
25	ρ_b	0.02	min^{-1}	Basal value of ρ[136]
26	k_ρ	350		Sensitivity of ρ on the activation of γ[136]
27	I_0	1.6	amol	Insulin amount contained in a granule[136]
28	N	2.76e6		Total number of β-cells in the pancreas[136]
29	f_b	0.05		Basal value of the fraction f[136]
30	K_f	3.43	mmol/L	Parameter for f(G)[136]